Non-axisymmetric and Steerable Acoustic Field for Enhanced Stone Comminution in Shock Wave Lithotripsy

by

Jaclyn Mary Lautz

Department of Mechanical Engineering and Materials Science
Duke University

Date:_____

Approved:

_____
Pei Zhong, Supervisor

_____
Glenn M. Preminger

_____
Edward J. Shaughnessy

_____
W. Neal Simmons

_____
Sorin Mitran

Dissertation submitted in partial fulfillment of
the requirements for the degree of Doctor
of Philosophy in the Department of
Mechanical Engineering and
Materials Science in the
Graduate School of
Duke University

2014

ABSTRACT

Non-axisymmetric and Steerable Acoustic Field for Enhanced Stone Comminution in Shock Wave Lithotripsy

by

Jaclyn Mary Lautz

Department of Mechanical Engineering and Materials Science
Duke University

Date:_____
Approved:

_____
Pei Zhong, Supervisor

_____
Glenn M. Preminger

_____
Edward J. Shaughnessy

_____
W. Neal Simmons

_____
Sorin Mitran

An abstract of a dissertation submitted in partial fulfillment
of the requirements for the degree of Doctor
of Philosophy in the Department of
Mechanical Engineering and
Materials Science in the
Graduate School of
Duke University

2014

Abstract

The primary goal of this dissertation was to assess the feasibility of transforming an electromagnetic (EM) shock wave lithotripter with an acoustic lens as its focusing device from the original axisymmetric pressure distribution to a non-axisymmetric steerable acoustic field. This work was motivated by the desire to better match the distribution of effective acoustic pressure and pulse energy with the trajectory and anatomical features around renal and ureteral calculi during clinical shock wave lithotripsy (SWL). The acoustic field transformation was accomplished by the design of a fan-shaped acoustic barrier (mask) placed on top of the lithotripter acoustic lens to selectively reduce the source aperture along the direction of the barrier axis, therefore effectively broadening the beam width (*BW*) of the lithotripter field in this preferred direction. Moreover, the geometry of the original lens (L_1) was modified so that the acoustic focus of the new lens (L_2) at high output voltages (necessitated by the incorporation of the mask) is closely aligned with the lithotripter focus. The mask was further driven by a motor-controlled gear system to rotate around the lithotripter axis, generating a steerable and non-axisymmetric acoustic field. In this dissertation project, a linear acoustic model was first used for parametric studies to assess the effects of mask geometry (opening angle and thickness) on beam elongation and peak pressure reduction. Based on this analysis, two mask geometries (L_2+M_{8025} and L_2+M_{9030}) were selected for modest and maximum beam elongation within the acceptable output range of the shock wave source. The acoustic and cavitation fields of the new lens with masks, as well as

the corresponding field produced by the original lens, were characterized using fiber optical probe hydrophone measurements and stereoscopic high-speed imaging. Different output voltage settings were used for each lens configuration (i.e., 14 kV for L_1, 15.8 kV for L_2+M_{8025}, and 17 kV L_2+M_{9030}) to produce equivalent acoustic pulse energy of 45 mJ in all setups, measured in the lithotripter focal plane. Under this condition, L_2+M_{8025} and L_2+M_{9030} generate lower peak pressure (38.2 and 36.8 MPa) with a significantly broadened BW_y (11.4 and 14.3 mm) along the *y*-axis (head-to-toe direction of the patient), which is aligned with the mask axis, compared to the high peak pressure (44.1 MPa) and moderate *BW* (7.5 mm) of L_1. It is worth noting that L_2+M_{8025} and L_2+M_{9030} produce a BW_x (7.6 and 7.5 mm) in the orthogonal direction to the mask axis, which is also comparable to L_1. Similarly, the beam width of the cavitation field was broadened from 8.1 to 12.2 mm for L_2+M_{8025}, and from 10.9 to 17.9 mm for L_2+M_{9030}, compared to the range of 8.8 to 9.4 mm measured from L_1. In comparison, L_2+M_{8025} produces a denser and narrower bubble cloud along the *y*-axis than L_2+M_{9030}. *In vitro* stone comminution (*SC*) tests in a tube holder (⦸ = 14 mm) have demonstrated that L_2+M_{8025} and L_2+M_{9030} are more effective at off-axis positions and during simulated respiratory motion along the elongated beam direction. The results of *SC* also confirmed the correlation between *SC* and the average peak pressure, $p_{+(avg)}$, and effective acoustic pulse energy, $E_{eff,}$ delivered to the stone, as shown in previous studies. Furthermore, a ureter model was developed and used to assess the performance of L_2+M_{9030}, which has the maximally elongated *BW* under various static and simulated respiratory motion conditions. The results suggest that

L_2+M_{9030} can produce significantly better *SC* than L_1 when the elongated beam is effectively aligned with the stone/fragments in the ureter or with their motion trajectory during the course of SWL treatment. Altogether, the results of this dissertation work have demonstrated *in vitro* that a non-axisymmetric and steerable acoustic field can significantly enhance stone comminution under clinically relevant SWL conditions. Future work is warranted to optimize the mask design and steering protocol to maximize the benefit of such an adaptable and versatile design to improve the performance and safety of clinical EM lithotripters.

To my parents, Bob and Sue Lautz,
who taught me the value of hard work and whose love, support and sacrifice
have provided me the opportunity to pursue every one of my dreams.

Table of Contents

List of Tables

List of Figures

Acknowledgements

I am fortunate to have been surrounded by incredible mentors, talented colleagues, and supportive family and friends throughout my years as a Ph.D. student. I would like to first thank my advisor Dr. Pei Zhong for inspiring me to dig deep into scientific phenomena, to be rigorous in my research while maintaining sight on the big picture and to always strive to better myself professionally. His support throughout my graduate studies has helped me design novel experiments, make effective presentations, produce quality publications and receive the National Science Foundation Graduate Research Fellowship and Engineering Innovation Research Fellowship. I would also like to thank the rest of my doctoral committee, Dr. Edward J. Shaughnessy, Dr. Glenn M. Preminger, Dr. W. Neal Simmons and Dr. Sorin Mitran for their insights and support that have been critical to my numerous projects and for my development as an engineer.

I would like to extend a sincere appreciation for Dr. Georgy Sankin who has been an amazing mentor teaching me to pursue innovative research, to be persistent in generating creative experimental designs and to be both an excellent scientist and practical engineer. There were many days during this difficult journey that he provided me the encouragement that I needed to sustain motivation for completing my Ph.D. Additionally, Dr. Sankin helped design the stereoscopic imaging setup and ureter model in this dissertation work. I would also like to thank Joseph Kleinheinz for his contributions to the automated acoustic field measurement program and post-processing of data; his ability to design and implement user-based code is remarkable.

I am grateful for my other colleagues in the Therapeutics Research Lab including Nate Smith, Fang Yuan, Chen Yang and Ying Zhang for providing me with a professionally and culturally stimulating environment. I would specifically like to thank Nate Smith for his insight on critical acoustic field parameter quantification and for his respiratory motion model used in this dissertation work. Furthermore, I wish to thank Dr. Glenn Preminger, Dr. Andreas Neisius, Dr. Nicholas Kuntz and Dr. Richard Shin, our collaborators in the Urology Department at Duke University Medical Center, who have provided a valuable clinical prospective to this fundamental engineering design work helping to align *in vitro* experiments to address clinical challenges. I wish to also thank Pat McGuire, Nikhil Bumb and John Goodfellow for providing technical expertise and feedback throughout the evolution of my experimental design.

I want to thank my loving family and friends for preserving my smile and laughter throughout this challenging and long Ph.D. journey. I am forever thankful for my parents, Bob and Sue Lautz, for teaching me insistent determination, for supporting every goal I set and for showing me how to have fun in life. I am also grateful for my brother, Randy Lautz, for not only being an incredible person but also someone whose ideals I admire so much. Finally, I want to thank my amazing fiancé, Alex Clausen, for inspiring me to succeed every day. Even during five years of long distance, he provides me with more encouragement, motivation and love than anyone could hope to have in life. This research was supported in part by the National Science Foundation Research Fellowship (DGE-0646085) and by the National Institutes of Health (5R37DK052985-17).

Nomenclature

A_{thres}	Area for effective stone comminution
a_x	Misalignment along the *x*-axis
a_y	Misalignment along the *y*-axis
β	Mask fanning angle
BW	-6 dB beam width in focal plane for acoustic field
BW_x	-6 dB beam width along the *x*-axis in the focal plane
BW_y	-6 dB beam width along the *y*-axis in the focal plane
$BW_{cav\text{-}x}$	Bubble cluster full width half maximum as visualized from *x*-*z* plane
$BW_{cav\text{-}y}$	Bubble cluster full width half maximum as visualized from *y*-*z* plane
c_w	Sound speed in water
c_p	Sound speed in polyurethane rubber
c_S	Sound speed in hard BegoStone
ρ_w	Density of water
ρ_p	Density of polyurethane rubber
ρ_S	Density of hard BegoStone
D	Diameter of source (electromagnetic coil)
D_{exc}	Respiratory motion excursion distance
D_f	Diameter of stone fragments
D_h	Diameter of holder
$dose_{eff}$	Effective dose of specified acoustic field parameters ($p_{+(avg)}$ or E_{eff})
E_{eff}	Effective pulse acoustic energy
EM	Electromagnetic
F	Lithotripter focus
f_L	Lithotripter focal length
LSW	Lithotripter shock wave
L_1	Original acoustic focusing lens (R = 220 mm)

L_2	New acoustic focusing lens (R = 350 mm)
λ	Wavelength of sound wave
M_{8025}	Acoustic barrier with geometry $\beta = 80°$ and $\Delta R = 25$ mm
M_{9030}	Acoustic barrier with geometry $\beta = 90°$ and $\Delta R = 30$ mm
p_+	Peak pressure of shock wave
p_-	Minimum of shock wave (tensile phase)
$p_{+(avg)}$	Average peak pressure
$p_{+(avg),\ thres}$	Threshold pressure for stone fragmentation
$\lvert p_{-(avg)} \rvert$	Absolute average peak negative pressure
PII	Pulse intensity integral (energy flux density)
PRF	Pulsed repetition frequency
Φ	Angle between ureter phantom and respiration axis
ΔR	Mask covering radius
R_{IEC}	Radius of 6 mm defined by IEC standard
R_h	Radius of stone holder
$r_{x,thres}$	Radius (along *x*-axis) corresponding effective fragmentation threshold
$r_{y,thres}$	Radius (along *y*-axis) corresponding effective fragmentation threshold
$Shocks_{eff}$	Effective administered shock wave dose
SC	Stone comminution
$SC_{0.5}$	50% of maximum stone comminution
SWL	Shock wave lithotripsy
t	Time
ν	Frequency of pressure waveform
Z_w	Impedance of water

1. Introduction and motivation

1.1 Kidney and ureteral stone disease

Kidney and ureteral stones (or renal calculi) affect about 10% of males and 7% of females in the United States [1], and its incidence worldwide continues to rise [2-4]. Stone formation is a complex process, initiated by mineral metabolic disorders and modulated by environmental conditions such as high temperature, intense exercise or diets of high protein, high sodium or low calcium [5]. Most renal calculi are brittle materials that contain crystalline (calcium, phosphates, uric acid, urate, crystine and xanthine) and noncrystalline (protein, cellular debris and other organic materials) components [6-8]. Renal calculi, containing only 1-2 crystalline materials, are often constructed either in a concentric layer formation or a conglomerate of crystalline and matrix materials without any organized features [2]. Kidney and ureteral stones, if they are small in size (< 4 mm), may pass naturally without any medical interventions; however, when they are big and obstruct the urinary tract, immediate clinical treatment is required [2, 9].

1.2 Evolution of shock wave lithotripsy

Shock wave lithotripsy (SWL) was first introduced commercially in the early 1980's as a non-invasive treatment of renal stone disease [10]. In SWL a few thousand (2,000 – 3,000) focused shock waves are delivered at about 1 Hz pulse repetition frequency (PRF) to break the target stones into fine fragments that can pass

spontaneously through the ureter. In the United States, about 50% of renal stones are treated by SWL which is considered most effective for treating non-lower pole kidney stones < 2 cm and upper (or proximal) ureteric stones < 1 cm (excluding cystine stones in both cases) [11-14]. Competing treatment modalities to SWL include more technically demanding minimally invasive stone removal techniques (percutaneous nephrolithotomy and ureterorenoscopy), which have advanced significantly producing stone-free rates of 90 – 100% and low retreatment rates [4, 15, 16]. However, SWL remains to be treatment the first option for treating most renal stones.

Despite technical developments in the past 30 years, the performance of modern lithotripters has not completely matched the gold-standard established by the 1st-generation HM3. Lithotripters have improved greatly in areas of imaging and acoustic coupling techniques that simplified the positioning of patients from treating in a large water bath to using "dry" coupling, a silicone-encased water cushion in contact with the patient's skin. In addition, contemporary lithotripters commonly utilize electromagnetism for highly reproducible, long-lasting and stable shock wave generation as compared to the short lifespan of electrodes used for shock wave generation in the HM3 [17]. Moreover, modern lithotripters were designed with larger source apertures to reduce pain from shock wave treatment by spreading the acoustic field over a broad area of the patient's skin. Reduction in pain allowed for clinicians to utilize sedation instead of general anesthesia thus reducing treatment duration and cost. Wider apertures, however, generated narrow focal widths in the vicinity of the target stone. This technical

evolution of the lithotripter acoustic field from low peak pressure and broad beam width to high peak pressure narrow beam width has consequently led to higher incidence of tissue injury, increased stone reoccurrence and decreased stone-free rates [18, 19]. This dissertation work aims to address this primary drawback in contemporary lithotripters by transforming their acoustic field from an axisymmetric to non-axisymmetric pressure distribution to better match with the anatomical features around the stone in the renal collecting system and to more effectively cover the translating trajectory of stone/fragments during clinical SWL.

1.3 Electromagnetic shock wave technology

Although electrohydraulic, electromagnetic (EM) and piezoelectric technologies have been used in SWL, the majority of contemporary lithotripters utilize EM technology because of its high reproducibility in shock wave generation and long-lasting stability of more than a million shocks (less than 10% variation between subsequent shocks) [20]. In EM lithotripters, the acoustic source consists of an electric coil placed in close proximity to a thin metal membrane [Figure 1.1]. When an electric current impulse is rapidly discharged through the coil, a repulsive electromagnetic force is induced on the thin metal membrane, launching an acoustic wave into the surrounding medium [20]. Two methods commonly used for shock wave focusing in EM lithotripters are by an acoustic lens (used in this work) and a parabolic reflector (used for cylindrical shock wave source). The acoustic wave generated by the source is transformed into a shock wave through nonlinear propagation in the medium toward the lithotripter focus [20, 21]. The

acoustic pressure distribution generated by an EM lithotripter is cigar-shaped along the lithotripter or *z*-axis and axisymmetric in the plane perpendicular to the shockwave propagation path. Beam width (or focal width) is calculated as the full width at half maximum pressure in the focal zone, and most commonly in the focal plane of the lithotripter.

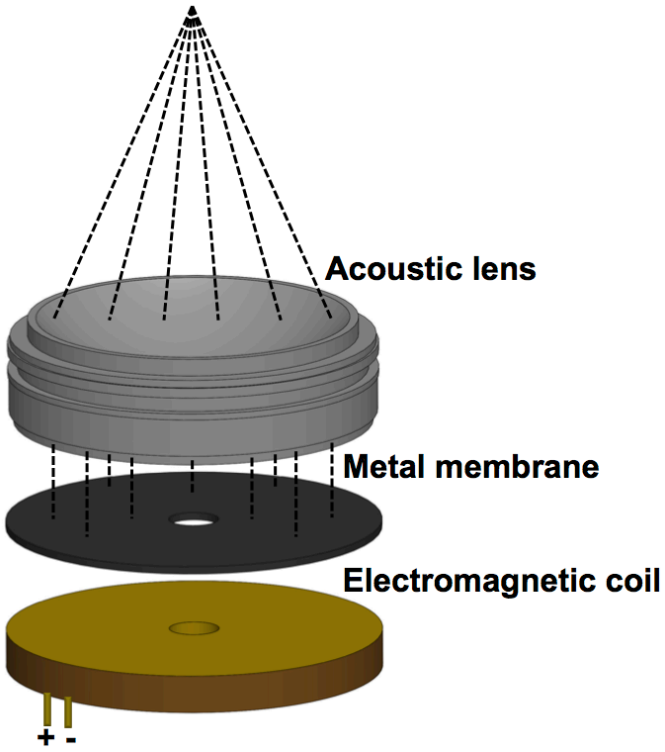

Figure 1.1: Schematic of the electromagnetic shock wave generation technology used in this work. Components include an electromagnetic coil that is excited by a short electric current pulse causing a repulsive force on the metal membrane generating a high amplitude planar acoustic wave that is subsequently focused by an acoustic lens.

1.4 Mechanisms of stone comminution

The ultimate goal of SWL is to pulverize the targeted stone into small enough fragments such that they can pass naturally through the ureter. As brittle materials, renal

calculi most likely break into fine pieces during SWL through the nucleation of microcracks and the subsequent crack growth under repetitive loadings, commonly referred to as dynamic fatigue [22]. Calculi are naturally heterogeneous materials with preexisting flaws that can be considered sites for microcrack initiation [23]. Damage mechanisms have traditionally been divided into two broad mechanisms: 1) direct stress waves produced inside the stone upon lithotripter shock wave (LSW) impact and 2) cavitation, formation of gas and vapor pockets, in the fluid medium surrounding the stone generated by the tensile phase of the LSW [Figure 1.2] [24, 25].

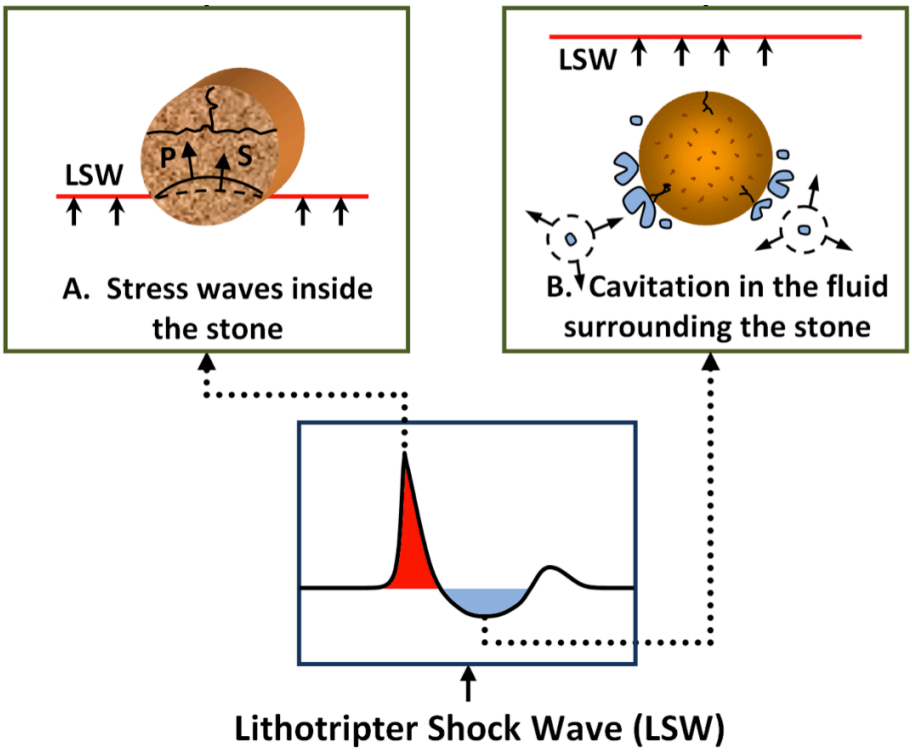

Figure 1.2: Schematic representation of the mechanisms contributing to stone comminution. Stress waves, generated inside the stone from the shock wave impact and reflection from impedance differences at stone-fluid interfaces, and cavitation, in the surrounding fluid medium generated from the negative pressure phase of the lithotripter shock wave, work synergistically to fragment stones. Image from reference [26].

Upon LSW impact, the incident shock wave is converted into both compression waves (P-wave) and shear waves (S-wave) while the surrounding tissue and fluid support only compression (pressure) waves [27]. Several mechanisms have been proposed to contribute to stone fragmentation in the early stage of SWL such as spallation, superfocusing, squeezing, shear, compression-induced tensile failure, and dynamic fatigue [16, 18, 20, 28-31].

Cavitation bubbles in the fluid (urine) surrounding the stone and along the LSW propagation path continue to expand long after the shock wave has passed. Bubbles grow several orders of magnitude in size until the static pressure in the fluid forces the bubbles to violently collapse [25, 32]. When a bubble collapses symmetrically in a fluid, a secondary shock wave will be generated. If the bubble collapse occurs near a solid boundary, a microjet of fluid will be formed (with a jet speed on the order of 100 m/s) that impact violently onto the stone surface, leading to surface erosion [33, 34]. Cavitation becomes more important as the stone comminution progresses during SWL with fragment size reduced, increased surface area and diminished role of stress waves [35-38].

Recently it has been shown that there is a strong correlation between the average peak pressure of the lithotripter field impact on a stone phantom and stone comminution efficiency both in water and in butanediol, a cavitation-suppressing medium [38]. This study also demonstrated that there is a critical pressure threshold needed to initiate stone fracture regardless of the medium surrounding the stone phantom or shock exposure,

which is in accordance with Griffith's theory for brittle material fracture [39]. This is the first study to propose the significant role average compressive peak pressure, compared to absolute peak pressure, has in effectively breaking stones thus extending the previous understanding of a linear correlation between stone comminution and acoustic pulse energy [28, 40]. The overall effectiveness of stone comminution in SWL is ensured largely by the synergistic interaction between stress waves and cavitation, especially at later stages of the treatment. Cavitation generates surface pits and flaws that serve as sites for crack initiation upon shock wave impact, which ultimately leads to complete fracture.

1.5 Motivation of an acoustic field transformation

The primary motivation of this dissertation work is to improve the treatment outcome of modern lithotripters by transforming the acoustic field surrounding the target stone. It is postulated that a transformation of the acoustic field from an axisymmetric to a non-axisymmetric pressure distribution in the plane perpendicular to the shock wave propagation axis will better match the irregular anatomical structures influencing stone spreading and to more effectively cover the trajectory of the stone during respiratory motion. By addressing these two challenges relevant to clinical SWL, stone comminution may be enhanced. There are two relevant limitations related to the modification of an acoustic field including 1) the threshold to which the beam can be broadened while still ensuring minimal pain on the skin's surface and capability to

fracture hard stones and 2) the maximum energy threshold that can be delivered along the LSW propagation path without causing tissue injury.

1.5.1 Stone translation caused by respiratory motion

The first clinical challenge addressed in this work is the effect of stone translation during respiratory motion on stone comminution efficiency. Previous clinical studies have shown that a patient's breathing may translate kidneys and ureters up to 40 mm [41-43]. Specifically, ultrasound imaging has shown that kidney stones and ureteral stones translate 10 – 40 mm and 7 – 10 mm, respectively, during respiration [44-47]. Respiration causes stones to translate in and out of the effective acoustic field thus accounting for 30 – 40% of administered shocks missing the stone [46, 48-50]. It has also been shown that the change in clinical protocol from general anesthesia to sedation reduces stone comminution because of increased patient movement, erratic breathing, inaccurate stone localization and deeper respiratory excursion displacements [51-54]. Lithotripters with a small focal zone amplify this effect. In contrast, lithotripters with a broad focal zone typically produces better stone comminution *in vivo* due to their better coverage of stone spreading within the kidney and respiratory motion leading to a higher likelihood of successful outcomes. It has been previously shown that high pressure narrow beam widths increase tissue injury [55, 56] supported by correlations of LSW energy flux density and administered energy to tissue injury [57-59]. Therefore, it is not possible to increase power output of high pressure narrow beam width lithotripters to enhance stone fragmentation area without increasing risk of tissue injury.

Two areas of recent research have aimed at addressing the challenges associated with stone spreading during treatment and stone motion during patient respiration. First, real-time tracking systems (ultrasound and predictive tracking algorithms) continuously track and aim shock waves on the stone [60-62]. Recently it has been shown that a tracking system controlling an EM lithotripter is able to track a stone *in vitro* with over 90% accuracy [63]. However, limitations in implementing these tracking systems in clinic include the degradation of image quality as fragments become smaller making accurate targeting difficult and the requirement to re-localize the stone occasionally using fluoroscopy, which consequently may increase treatment time and X-ray dose [45].

Second, it has been shown that lithotripters with low peak pressure broad beam width produce better stone comminution *in vitro* with stone spreading and during simulated respiratory motion, and *in vivo* in animal models, compared to their high peak pressure narrow beam width counterparts under equivalent focal area acoustic pulse energy [48, 64, 65]. Generally, these previous studies focused on broadening the pressure distribution while maintaining the symmetry of the acoustic field and the pulse energy in the focal region. There is a constraint of the maximum acoustic pulse energy that can be delivered to the kidney without causing hematoma. Therefore, it may be advantageous to selectively increase the pressure field distribution along the axis of stone movement during respiration while concomitantly decreasing or maintaining the pressure distribution along the axis perpendicular to respiration. A non-axisymmetric elongated field has been previously reported for the HM3 [66], which has a non-axisymmetric

pressure field distribution with an elongated beam width of 12 – 14 mm (at 20 kV) in the direction of respiratory motion (Head – Foot) compared to a narrow beam width of 8 – 9 mm in the transverse (Left-Right) direction [67, 68].

1.5.2 Kidney and ureter structure

The second clinical challenge that motivates a non-axisymmetric acoustic field is that stones commonly treated with SWL are generally located in irregular elongated anatomical structures consequently creating a directional bias for fragment spreading during treatment. Kidneys are bean-shaped structures that have a substantial role in maintaining various physiological functions for the human body including filtering and excreting metabolic waste products (urea and ammonium), regulating electrolytes, stimulating red blood cell production, controlling reabsorption of water, glucose and amino acids, and regulating blood pressure. A network of tubules and ducts, referred to as the collecting system, filter through the kidney to the ureter. The renal pelvis funnels urine from the kidney to the ureter and measures ~10 - 15 mm in diameter [69]. Stones are commonly found at the top part of the collecting system (upper pole), the renal pelvis, the ureter or the bottom part of the collecting system (lower pole and are especially difficult cases) [Figure 1.3]. The ureter is usually around between 3 – 4 mm in diameter and may dilate at the proximal end up to 6 – 10 mm in diameter when obstructed by stones [69, 70]. As stones fragment during SWL treatment, directional spreading occurs in these tubular structures. Furthermore, the axis of respiration is generally in line with these elongated structures, particularly the ureter and renal pelvis.

Currently, the acoustic field administered upon the stone does not account for anatomical structures or have a feature to control acoustic field distribution based on stone location. An axisymmetric pressure distribution upon a target stone with a ~8 mm beam width is utilized for ureteral stones even though more than half of the acoustic pulse energy may be delivered solely to surrounding tissues or may be partially ineffective in fragmentation since the stone can only spread along the length of the ureter. Therefore, a non-axisymmetric pressure distribution that maximizes the administered energy to the area of stone spreading may be more efficacious for stone comminution while concurrently minimizing the risk of tissue injury. Previous research has investigated the dependence of stone location and size on stone comminution efficiency and stone free rates [11, 71] but there has been minimal work in addressing the need to customize the acoustic field dependent on stone location.

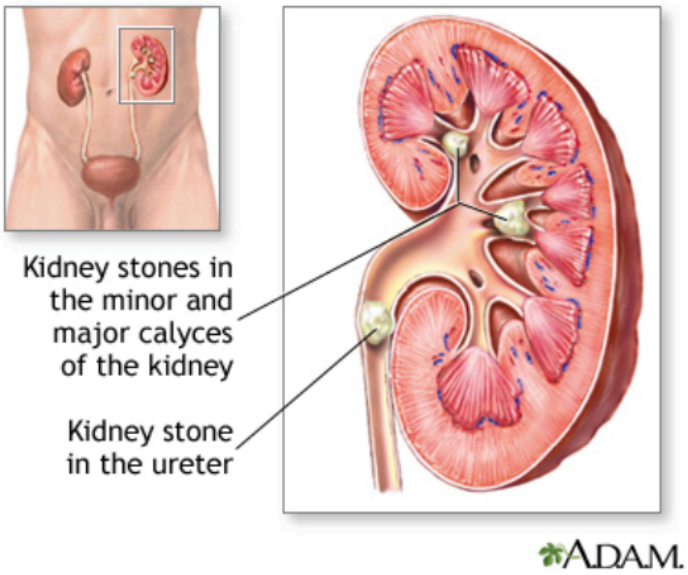

Figure 1.3: Locations of stones commonly treated with SWL. Image from reference [72].

1.6 Significance and aims of the current study

The overall objective of this dissertation is to design, implement and evaluate an acoustic field transformation to a clinically relevant EM shock wave lithotripter to enhance stone comminution efficiency. In Chapter 2, an attachable acoustic barrier (mask) is designed and engineered, guided by linear acoustic approximations for choosing geometric parameters, to transform an axisymmetric to a non-axisymmetric acoustic field in the focal plane. Non-axisymmetric acoustic fields generated by two masks were acoustically characterized and compared to a clinically relevant axisymmetric acoustic field in Chapter 3. Characterization includes pressure waveform measurements in the lithotripter focal zone to calculate critical acoustic field parameters. In addition, a method for simultaneous high-speed imaging of two perpendicular planes is used for cavitation activity evaluation and comparison of different lens configurations. Chapter 4 describes *in vitro* stone comminution evaluation of the new non-axisymmetric elongated acoustic fields compared to the original axisymmetric acoustic field. Stone comminution evaluation includes treating stones at the focus and off-axis positions and treating translating stones during simulated respiratory motion, with and without clinically relevant initial stone misalignment. In Chapter 5, a design for controllable acoustic field steering of a non-axisymmetric pressure distribution is introduced and evaluated in a ureter model, mimicking similar anatomical structures observed *in vivo*. Finally, the transformation of the axisymmetric acoustic field to a non-axisymmetric

steerable acoustic field is summarized in Chapter 6 and areas of future work are outlined in Chapter 7.

2. Experimental design for acoustic field transformation

A primary goal in this dissertation is to construct a simple yet flexible device that can be attached to an existing shock wave source to transform its axisymmetric pressure field in the focal plane to a non-axisymmetric and elongated pressure field to better match with the trajectory of stone/fragments during SWL. Engineering an attachable device instead of executing a re-design of the shock wave source allows us to evaluate a variety of design features with minimal cost and time.

To assess the feasibility of such a design, we first utilized a linear wave propagation model to simulate beam elongation created by using acoustic barriers (or masks) to cover strategically a portion of the source. The model was then used to assess the effects of key design parameters on beam width elongation and peak pressure reduction in the focal plane. Based on the results of these pilot tests, two mask designs were selected for engineering construction (Chapter 2), modified acoustic field characterization (Chapter 3), and performance evaluation (Chapter 4 and 5) against the original shock wave source under comparable effective acoustic pulse energy.

2.1 Design concept

The EM shock wave sources used in this work are capable of operating in a large dynamic range from minimal pressure output of 10 MPa to peak pressures of ~80 MPa by adjusting the source charging voltages to its upward limit of ~19 kV. For clinical treatment of stones in the kidney using the original lens, the shock wave source is usually

operated in the range of 12 – 17 kV. Therefore, maintaining the acoustic pulse energy when covering a portion of the source by a mask as compared to an uncovered source is feasible by adjusting the source charging voltage. This operational upper limit of the experimental setup is a critical parameter that limits mask geometry selection for maintaining equivalent acoustic pulse energy in the focal zone. Furthermore, at higher output voltages there is a pre-focal shift of the position (z < 0 mm) of the LSW peak positive pressure (p_+) and peak negative pressure (p_-) from the lithotripter focus (z = 0 mm), where a kidney stone is positioned during SWL. It has been shown recently that by a simple change in the curvature of the acoustic lens, this misalignment of the LSW p_+ with the lithotripter focus can be corrected [65].

In this study, the transformation of the lithotripter acoustic field in the focal plane was first analyzed based on a linear wave propagation model of a piston source. Figure 2.1(a) shows a representative pressure pulse measured near the surface of an EM coil operated at 14 kV [73]. A Fourier transform of the pressure pulse reveals its frequency spectrum shown in Figure 2.2(b). The fundamental frequency (v_0) was measured to be 0.13 MHz with an upper -6 dB bandwidth of 0.18 MHz. The near to far field (diverging) transition distance from the EM coil (L) can be determined by [74]:

$$L = \frac{D^2}{\lambda} \tag{2.1}$$

where D (= 134 mm) is the diameter of the EM coil, $\lambda = c_w/v_0$ = 11.5 mm – 8.3 mm is the wavelength of the sound wave (c_w = 1500 m/s) for v_0 (= 0.13 – 0.18 MHz).

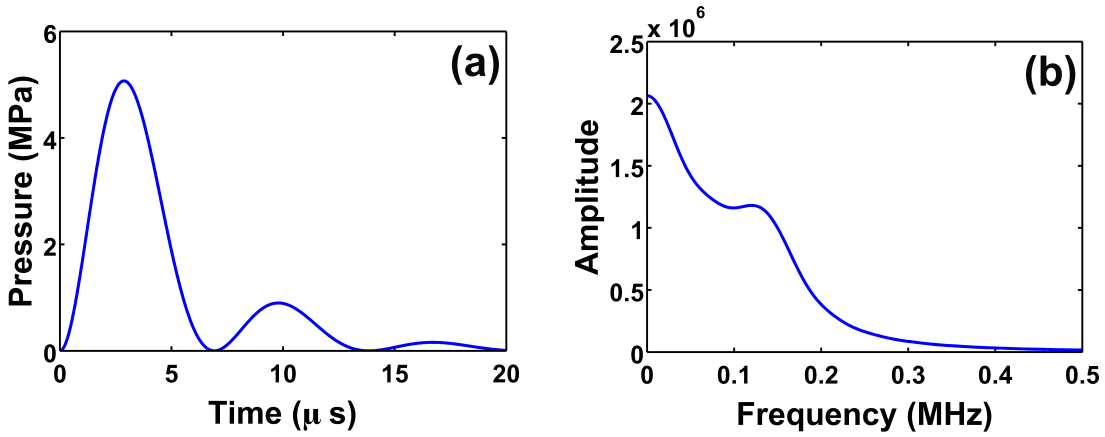

Figure 2.1: (a) Representative pressure pulse near the electromagnetic coil generated by a 14 kV charging voltage measured at a radial distance from the center of 40 mm and corresponding (b) frequency spectrum fundamental frequency at 0.13 MHz with an upper -6 dB bandwidth of 0.18 MHz.

This leads to a value of L in the range of 1560 mm to 2150 mm, confirming that the focal length (f_L) of the EM lithotripter (181.5 mm) is in the near field of the EM coil. Therefore, the beam width (BW) of the focused acoustic source can be approximated by [74-76],

$$BW = C\frac{f_L \cdot \lambda}{D} \tag{2.2}$$

where C is a constant.

Equation 2.2 suggests that the BW of a circular source of a given frequency is inversely related to the source aperture size (D). Hence, blocking or absorbing a portion of the acoustic output can effectively reduce the source aperture D and consequently increase the BW of the focused wave. If only a portion of the source is blocked, the lithotripter field will be transformed from an axisymmetric to a non-axisymmetric geometry with a BW different along the blocked direction vs. the orthogonal non-blocked

direction. In this study, the EM coil diameter along the *y*-axis (D_Y) was reduced through blocking a portion of the lithotripter output by an engineered fan-shaped mask, defined by opening angle β and radius thickness ΔR. Figure 2.2(a) illustrates the principle of wave focusing in an EM lithotripter and the positioning of the masks above the acoustic lens. There is a one to one correlation between a point on the source (*S*) and a point in the mask plane before each ray converges to the lithotripter focus (*F*). An axisymmetric source will have the same *BW* in all orientations [Figure 2.2(b)]. In comparison, it is postulated that a source with an uneven aperture (wider along the *x*-axis than the y-axis, $D_X > D_Y$) will produce an elongated beam with a broader pressure distribution along the *y*-axis ($BW_Y > BW_X$) [Figure 2.2(c)]. This particular geometry was selected to block the least surface area of the EM coil while still effectively reducing the source aperture along one preferred direction. Prior to mask geometry selection for experimental implementation, a variety of mask designs were theoretically evaluated by linear wave propagation approximations based on Huygens-Fresnel principle.

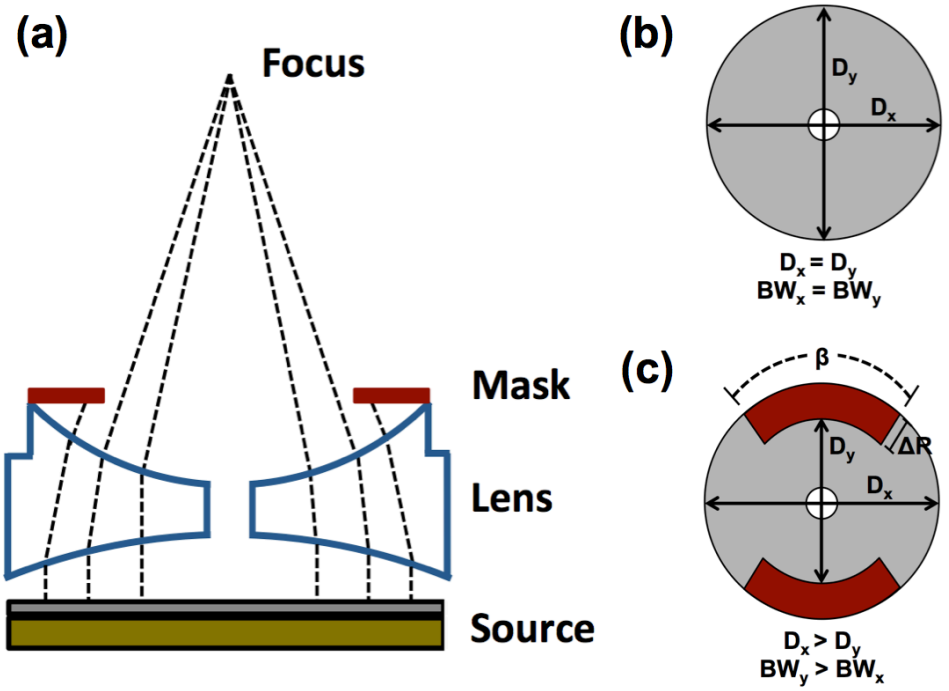

Figure 2.2: (a) Schematic side view of the electromagnetic source with an acoustic mask positioned above the lens (black dashed lines correspond to wave focusing) (b) Top view of an axisymmetric source and (c) a non-axisymmetric source showing the relationship between source diameter (*D*) and focal plane acoustic field beam width (*BW*).

2.2 Linear wave propagation model

The effect of an acoustic barrier on the lithotripter field was evaluated using the Huygens-Fresnel principle, which states that the amplitude of a wavefront at some distance from an aperture is the superposition of an array of wavelets originating from the source each generating a linear spherical wave [77]. The sinusoidal spherical waves emitted from each point on the source surface were treated equivalently by its counterpart in the mask plane by incorporating a phase delay for focusing.

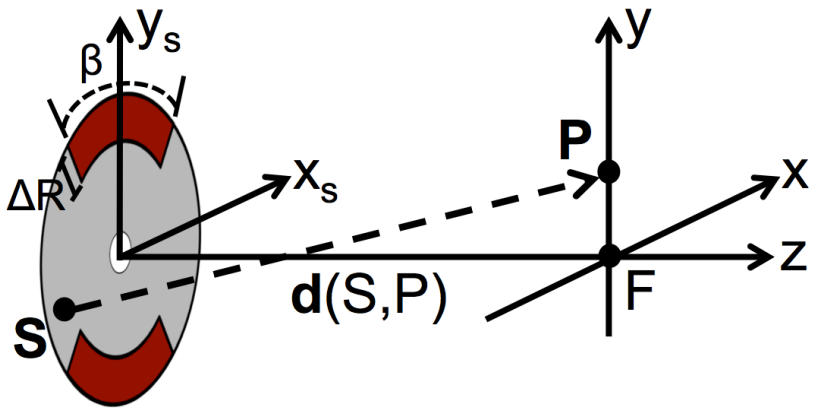

Figure 2.3: Schematic representation of the theoretical analysis based on linear acoustics showing a source grid position at *S* and a measurement point *P* in the lens focal plane where *F* corresponds to the focus.

Figure 2.3 shows the schematic representation of the resultant pressure amplitude *E* in the focal plane *P* (= (*x, y, 0*)) approximated by the superposition of all sinusoidal waves (with amplitude E_0 = 5 MPa) emanating from each individual point source located at the mask plane *S* (=(x_s, y_s, -*f*) described by

$$E(P) = \int \frac{E_0(S)}{d(S,P)} e^{i[k \cdot d(S,P) - \omega \cdot t_{shift}]} d\sigma. \quad (2.3)$$

where the wave number $k = \frac{\omega}{c}$, c = 1500 m/s in water, the angular frequency ω = 1.3 rad/s and $d\sigma$ corresponds to the area of integration defined by the uncovered EM coil surface area. Furthermore, the distance between an individual source point and its counterpart in the plane is described by

$$d(S,P) = \sqrt{(x - x_s)^2 + (y - y_s)^2 + f^2}. \quad (2.4)$$

where *f* (= 140 mm) is the distance between the lens and the focal plane.

To model a focused wave, two assumptions were further made in applying the Huygens-Fresnel principle in our analysis. First, it was assumed that each point source in the array generates an identical spherical wave of the same frequency. Second, it was assumed that there is a time delay in the wave generation at each point so that all spherical wavelets emanating from different parts of the source will arrive at the focus *F* in phase. Therefore, for each point source, a time shift was incorporated into the calculation by

$$t_{shift}c - d(S,F) = const \tag{2.5}$$

where

$$d(S,F) = \sqrt{{x_s}^2 + {y_s}^2 + f^2}. \tag{2.6}$$

Field approximations in the focal plane were investigated in (MATLAB R2012b, MathWorks Inc., Natick, MA) by defining an array of sources oriented in a circular grid of step size of dr = 1 mm and $d\theta$ = 1° [Figure 2.4]. Masks were incorporated into the simple model by assigning zero output to sources occupying those positions. Though approximate, the model provides valuable insight to the relationship between mask geometry parameters β and ΔR and the resultant acoustic field in the focal plane. Specifically, numerical approximations were evaluated for 300 conditions by varying acoustic mask β from 30° – 180° (in 5° increments) and ΔR from 0 mm – 50 mm (in 5 mm increments).

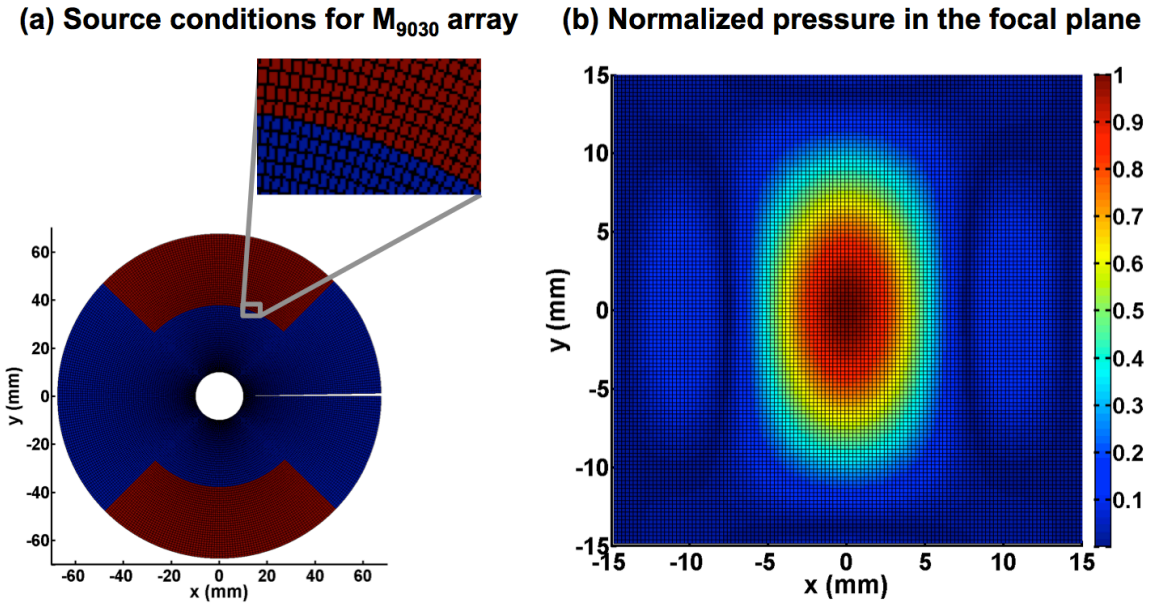

Figure 2.4: (a) Schematic representation (β = 90°, ΔR = 30 mm) of the defined array of sources oriented in a grid for numerical linear approximations and (b) normalized pressure output at the focal plane.

2.3 Assessment of beam width elongation and pressure reduction in the focal plane

Two parameters were extrapolated from the numerical evaluation of the 300 mask geometries including *BW* elongation ratio (BW_y/BW_x) and pressure ratio reduction (E_m/E_0). Beam width elongation is defined by the ratio of the elongated beam width (BW_y) to the narrow beam width (BW_x) determined by measuring the full width half maximum beam width along the *y*-axis compared to the beam width along the *x*-axis. Pressure reduction is evaluated by the ratio of the focal point pressure with a mask (E_m) to the focal point pressure with no mask (E_0). From numerical approximation results and acoustic field criteria necessary for this work, mask geometries were selected for experimental execution. Figure 2.5(a) and 2.5(b) show *BW* elongation ratios and peak

pressure reduction, respectively, in the focal plane for the 300 mask geometries investigated in this study.

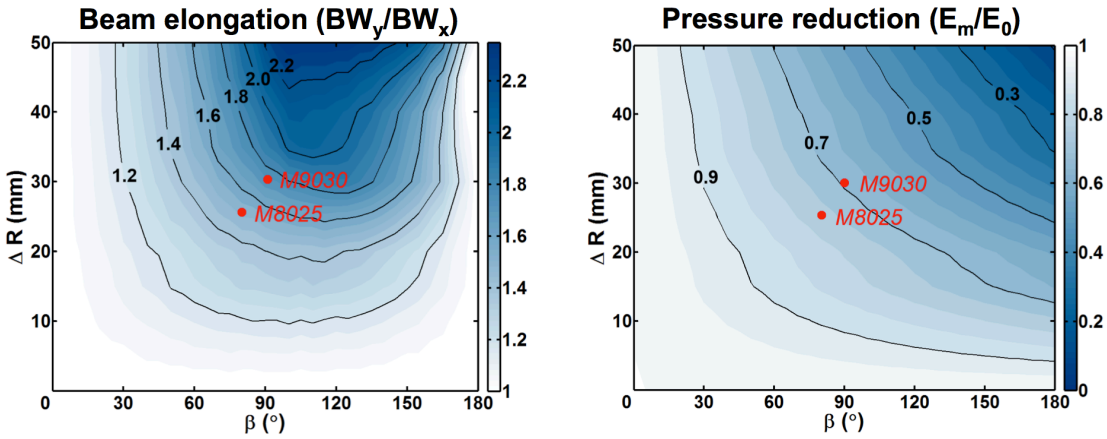

Figure 2.5: Contour plots of (b) beam elongation ratio (BW_y/BW_x) in the focal plane and (c) pressure amplitude reduction (E_m/E_0) at the focus calculated as a function of acoustic barrier geometry parameters ΔR and β.

For significant BW elongation, the mask geometry must have a fanning angle within $50° < \beta < 150°$. Furthermore, the coverage radius ΔR must be greater than 10 mm. Secondly, covering a portion of the EM coil reduces the pressure output as observed with E_m/E_0 approaching 0 as ΔR and β increase. As previously mentioned, given the operational range of the EM lithotripter's charging voltage of 17 kV, smaller β is preferable because the pressure reduction in E_m/E_0 will be less. This numerical model provides insight for choosing effective mask geometries that yield a non-axisymmetric acoustic field with minimal pressure reductions.

2.3.1 Acoustic mask geometries selected for this study

Based on the numerical calculations, two experimental mask designs were selected for further investigation in this study. The first mask has a *BW* ratio of 1.5, which is similar to the value observed in the non-axisymmetric acoustic field of the original HM3. The second mask was selected to achieve a maximum *BW* elongation ratio of 1.7 within the operable charging voltages of the EM source. For each *BW* ratio, the mask geometry that yielded the smallest pressure reduction (or largest E_m/E_0) was selected. Table 2.1 summarizes the geometries and calculated field parameters (BW_y/BW_x and E_m/E_0) of both mask designs, M_{8025} and M_{9030}. Thereafter, masks were constructed and evaluated.

Table 2.1: Summary of mask design geometries selected for experimental implementation.

	β(°)	ΔR (mm)	BW_y/BW_x	A_m/A_0
M_{8025} 	80	25	1.5	0.77
M_{9030} 	90	30	1.7	0.70

2.4 Experimental setups

To ensure side-by-side comparison under similar experimental conditions, two sets of experimental EM shock wave sources were utilized, each is equipped with an identical EM coil yet different acoustic lenses and masks for pressure field transformation. Both sets of the EM sources were mounted at the bottom of an acrylic tank (L x W x H = 40 x 40 x 30 cm) filled with 0.2 μm filtered and degassed (O_2

concentration = 2 – 4 mg/L) water maintained between 22 – 25 °C [Figure 2.6]. The same power supply and delay generator (BNC Model 555) were used alternatively between the two sources. A peristaltic pump (Cole Palmer, 77200-60) flushed water over the front surfaces of the EM coils for cooling purpose throughout the experiment. A 3D computer controlled translational stage (VXM-2 step motors with BiSlide-M02 lead screw, Velmex, Bloomfield, NY) was mounted on top of the acrylic water tank allowing for precise positioning of either a stone holder or a hydrophone fiber tip in different experiments (see Chapter 3).

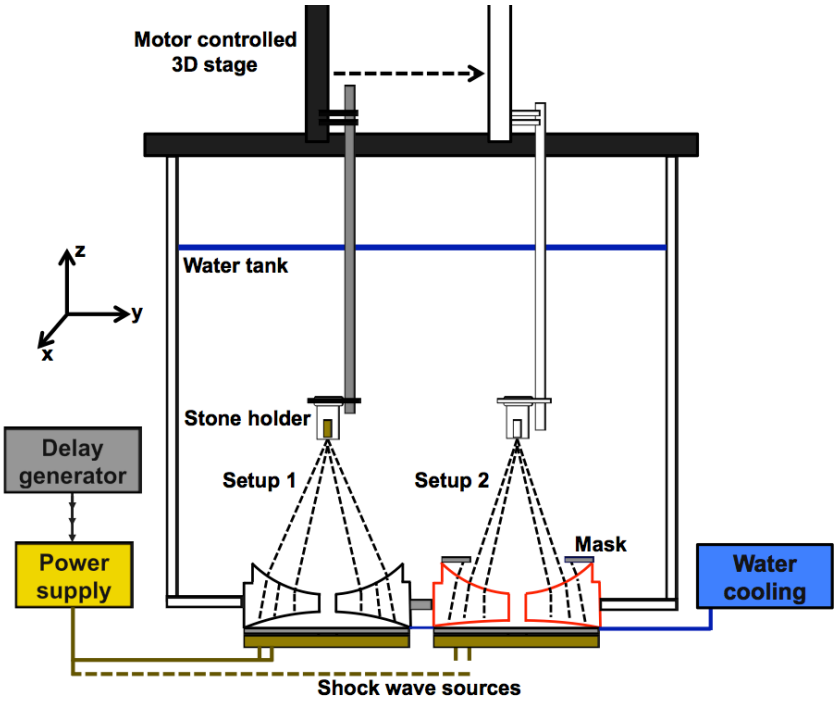

Figure 2.6: Schematic of the experimental components of two lithotripter setups. Setup 1 generates an axisymmetric pressure field distribution in the focal plane and an upgraded lithotripter, setup 2, generates a non-axisymmetric pressure field distribution in the focal plane. Setups were operated individually. The motor control stage was used for positioning of either a stone holder (with a stone phantom) or hydrophone (described in Chapter 3) and to translate between setups.

2.4.1 Mask design, construction and assembly

Masks, M_{8025} and M_{9030}, were designed in SolidWorks (Dassault Systèmes SolidWorks Corporation, Waltham, Massachusetts). Individual components were cut using a universal laser (VLS6.60, Universal Laser Systems, Scottsdale, Arizona) from acrylic sheets (Plaskolite, Inc., Columbus, OH) and EDPM (ethylene-propylene-diene monomer) closed-cell foam (McMaster-Carr, Atlanta, Georgia) [Figure 2.7(a) and (c)]. Masks was assembled from four parts: 1) the bottom and 2) top piece were cut from a 2 mm thick sheet of acrylic, 3) the middle piece from a 5.5 mm thick sheet of acrylic and 4) the two 4.8 mm thick black pieces were cut from waterproof closed-cell foam [Figure 2.7(b)]. All parts were bound together with acrylic cement (Weld-on 16, IPS Corporation, Compton, CA) creating a watertight air space inside the mask thus creating an acoustic barrier [Figure 2.7 (d)]. The mask was positioned and secured above the acoustic lens with an acrylic housing system designed in SolidWorks. Pressure measurements showed no pressure pulse could be transmitted through the mask, demonstrating effectiveness of the mask in blocking the incident LSWs.

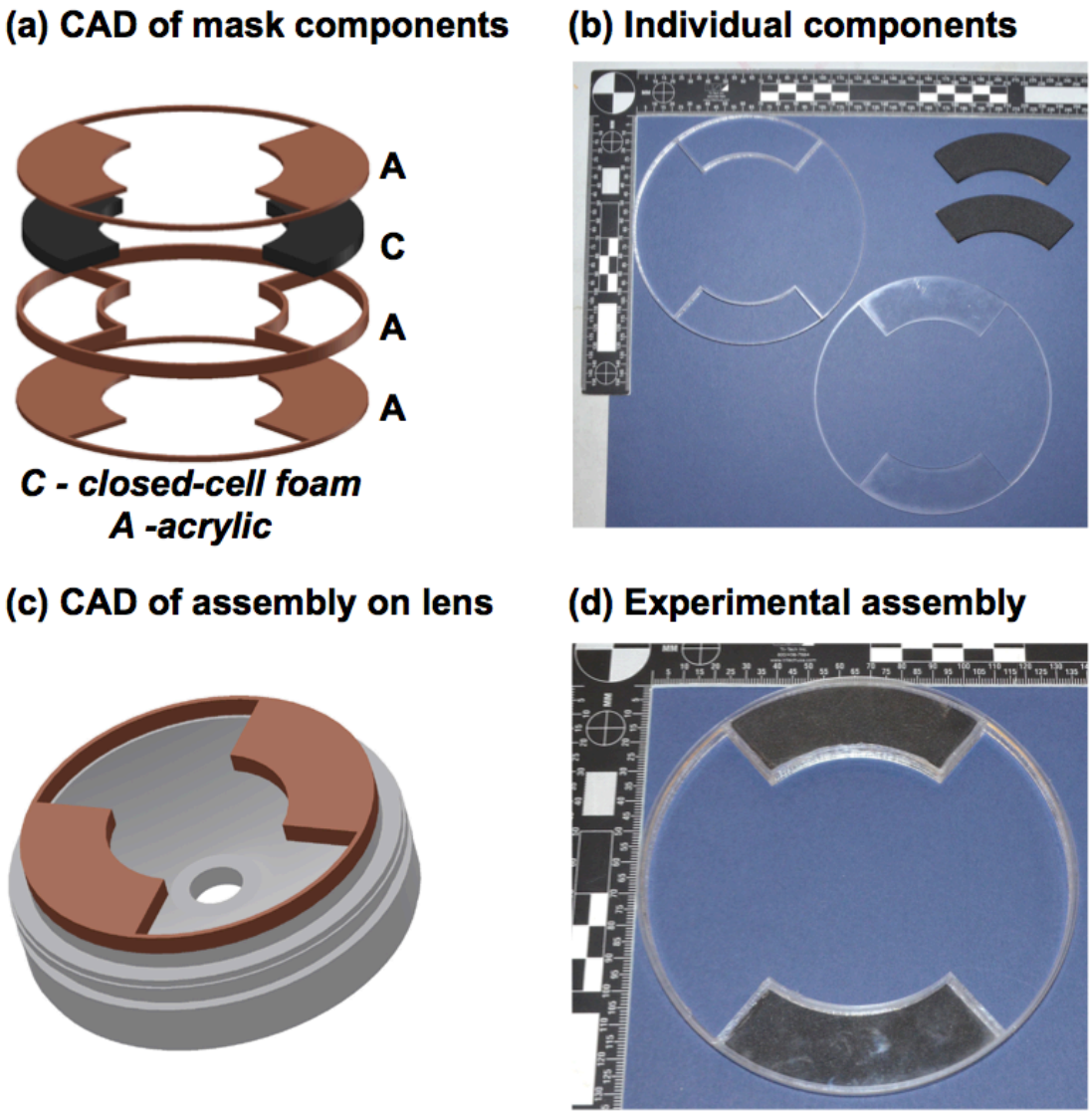

Figure 2.7: (a) Computer-aided design (CAD) and (b) experimental components of the mask design. (c) CAD of assembly on the acoustic lens. (d) Engineered assembly of the mask used in this study.

2.4.2 Acoustic lenses

Two experimental setups were used. Setup 1 [Figure 2.8(a)] includes an axisymmetric EM source and a clinically relevant focusing lens with an ellipsoidal upper

surface (semi-minor axis b_e = 95.03 mm and semi-major axis a_e = 111.52 mm) and a spherical lower surface (R = 220 mm) positioned against the EM source [L_1, Figure 2.8(b)]. Setup 2 includes an acoustic mask described by fanning angle β and covering radius ΔR [Figure 2.8(c)] secured above the acoustic lens [Figure 2.8(d)] to transform the axisymmetric acoustic field to a non-axisymmetric field in the focal plane (z = 0 mm, 181 mm from the EM coil).

Setup 2 was operated at a higher source charging voltage compared to setup 1 to maintain equivalent acoustic energy in the focal area since a mask blocks a portion of the EM lithotripter output energy. Therefore, a slightly modified acoustic lens (L_2) with a greater inner surface radius [Figure 2.8(d); R = 350 mm) compared to L_1 was used for alignment of the lithotripter focus with the position of the LSW p_+ in setup 2. A greater inner curvature of the focusing lens provides a post-focal shift of p_+ from the focus but at higher charger voltages, p_+ shifts toward z = 0 mm. L_1 and L_2 (without masks) [65]. Acoustic characterization and stone comminution efficiency were investigated with L_1 and L_2 (without masks) and performed approximately the same [Appendix A] at matched effective acoustic pulse energy E_{eff} of ~45 mJ (based on IEC 61846 lithotripter field characterization protocol) calculated in a circular area 12 mm in diameter. Setups are defined as L_1 (setup 1, control setup) and L_2+M_{8025} and L_2+M_{9030} (setup 2, two different mask implementations); therefore, three acoustic field outputs are evaluated in Chapter 3 – 5.

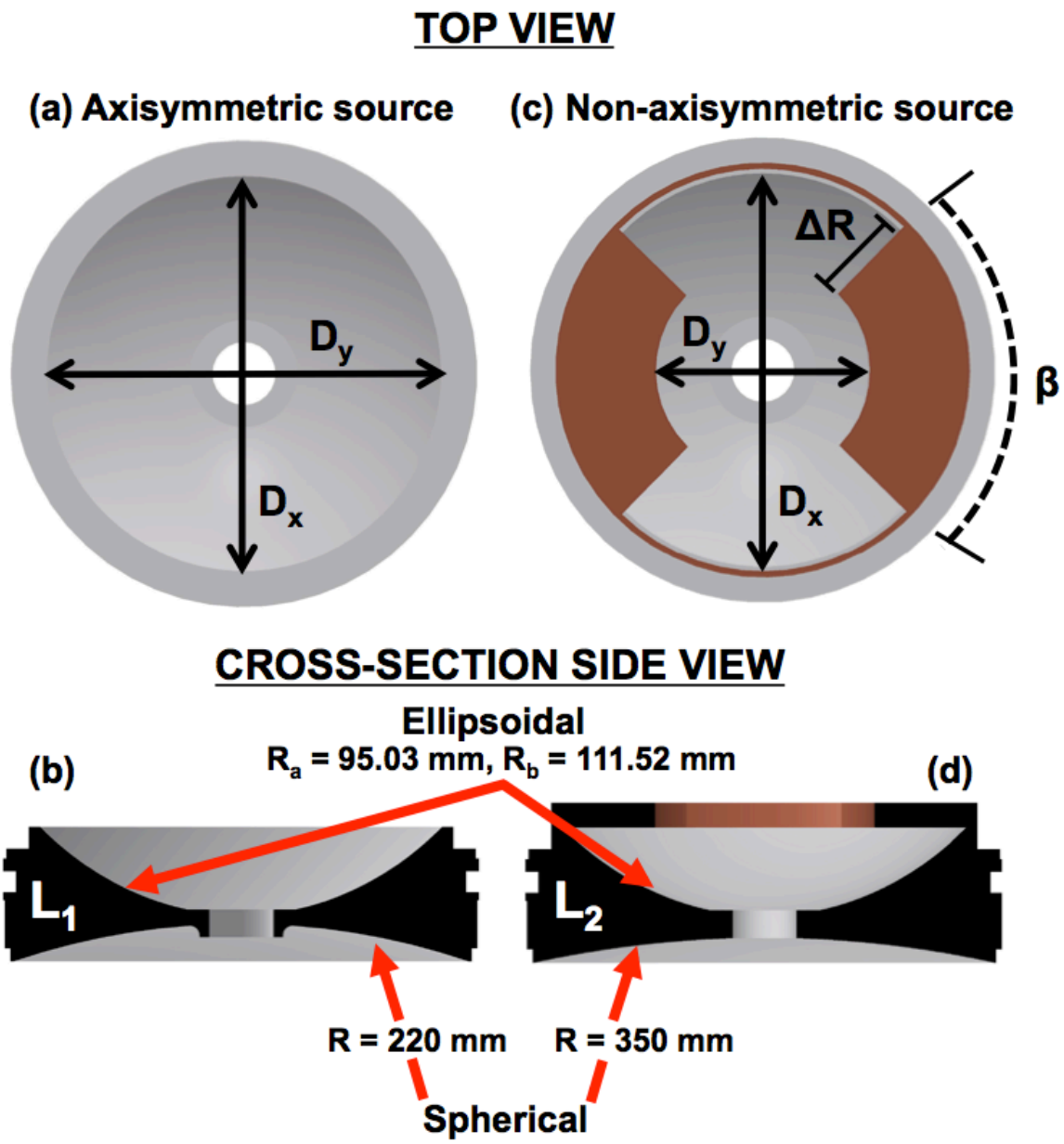

Figure 2.8: Top view of (a) an axisymmetric and (b) a non-axisymmetric source generated by blocking a portion of the electromagnetic coil with a fan-shaped acoustic masks made from acrylic and closed-cell foam and described by angle β and radius ΔR for reducing D_y while maintaining D_x. Side view showing the cross-section of (b) a standard acoustic lens with an inner spherical curvature of 220 mm (L_1) and (d) a modified acoustic lens with a larger spherical curvature of 350 mm (L_2) and a mask positioned and secured above it. L_1 and L_2 have equivalent upper ellipsoidal surfaces with semi-major axis of 111.52 mm and semi-minor axis of 95.03 mm.

3. Characterization of the acoustic and cavitation fields produced by the axisymmetric and non-axisymmetric sources

In this chapter, the axisymmetric shock wave field generated by L_1 and non-axisymmetric fields generated by L_2+M_{8025} and L_2+M_{9030} are characterized based on hydrophone measurements, from which key lithotripter field parameters are calculated. In addition, high-speed imaging captures the dynamics of cavitation bubbles produced by different shock wave sources, and the distribution of bubble density in the lithotripter field is determined.

3.1 Background – Physical characterization of the lithotripter field

Alongside parameters deduced from pressure waveforms, understanding and characterizing cavitation in the focal zone of the experimental setups is critical.

3.1.1 Acoustic field

Based on IEC 61846 standard, a lithotripter field is characterized by several key parameters, including beam width (*BW*), peak positive pressure (p_+), pulse intensity (*PII*), and effective acoustic pulse energy (E_{eff}). Among these parameters, there have been numerous studies, particularly focused in early stage fracture, that investigate the mechanisms that are responsible for stone fragmentation during SWL (described in section 1.4). However, translating the mechanisms of action from idealized experimental setups and theoretical analysis to lithotripter field parameters that correspond to effective stone comminution remains a challenge. A few studies have shown that stone

comminution efficiency linearly correlates with the incident lithotripter shock wave effective pulse acoustic energy E_{eff} [28, 40, 78]. E_{eff} is defined as the pulse acoustic energy integrated within a circular area in the focal plane centered at the lithotripter axis with a radius 6 mm (RI_{EC})

$$E_{Eff} = \frac{1}{\rho_w c_w} \int_S \left(\int_{t_1}^{t_2} p^2(t) dt \right) dS \tag{3.1}$$

where ρ_w and c_w correspond to the density and sound speed in the wave propagation medium, and t_1 and t_2 are the first and last points where the pressure exceeds 10% of p_+. More recently, the average peak pressure $p_{+(avg)}$ incident on a stone (or fragments) during SWL has been shown to correlate logarithmically with *in vitro* comminution efficiency [38].

3.1.2 Cavitation field

Cavitation is a mechanism that contributes significantly to stone comminution, predominantly as fragments reduce in size, and it also has been directly linked to tissue injury mechanisms [31, 79-82]. Previous *in vitro* studies have defined cavitation as predominantly a surface-acting mechanism specifically acting on the surface closest to LSW impact [36, 83]. Stones will not fragment as effectively without cavitation, which has been observed in reduced stone comminution in experimental studies that have used overpressure and viscous medias, instead of water, to suppress focal region cavitation activity [35-38].

Since the inception of SWL, there has been substantial effort to understand cavitation activity *in vitro* and *in vivo* using high-speed imaging, ultrasound imaging and passive cavitation detection [84-88]. Cavitation is quite volatile making it extremely challenging to develop metrics and standards that can effectively regulate a non-destructive environment for the patient's kidney and surrounding tissue. However, it is fairly well understood that an idealized acoustic field would include maximum bubble activity within the immediate vicinity of the stone surface with minimal bubble activity along the LSW propagation path (i.e. tissue in clinic).

The non-axisymmetric acoustic field generated by the upgraded lithotripter is motivated by optimizing these discussed field parameters that have been shown to be important for effective stone comminution in clinically relevant environments. In this chapter, experimental techniques focusing on pressure field characterization and cavitation visualization and quantification will be introduced to adequately investigate the upgraded lithotripter's non-axisymmetric pressure distribution. These results create the framework for stone comminution evaluation (Chapter 4 and 5).

3.2 Materials and methods

The experimental setup described in section 2.4 was used for acoustic field characterization in this chapter [Figure 3.1]. The axisymmetric field generated by the L_1 and the non-axisymmetric fields generated by the upgraded lithotripter setups L_2+M_{8025} and L_2+M_{9030} are characterized and compared. To establish a basis for comparison, L_1 was operated at a clinically relevant source charging voltage of 14 kV and upgraded

lithotripters, L_2+M_{8025} and L_2+M_{9030}, were characterized at multiple source charging voltages until conditions that yielded approximately equivalent E_{eff}, calculated within a circular area in the focal plane centered at the lithotripter axis with a 6 mm radius (Equation 3.1), to L_1 were used for direct comparison and stone comminution evaluation in Chapter 4 and 5.

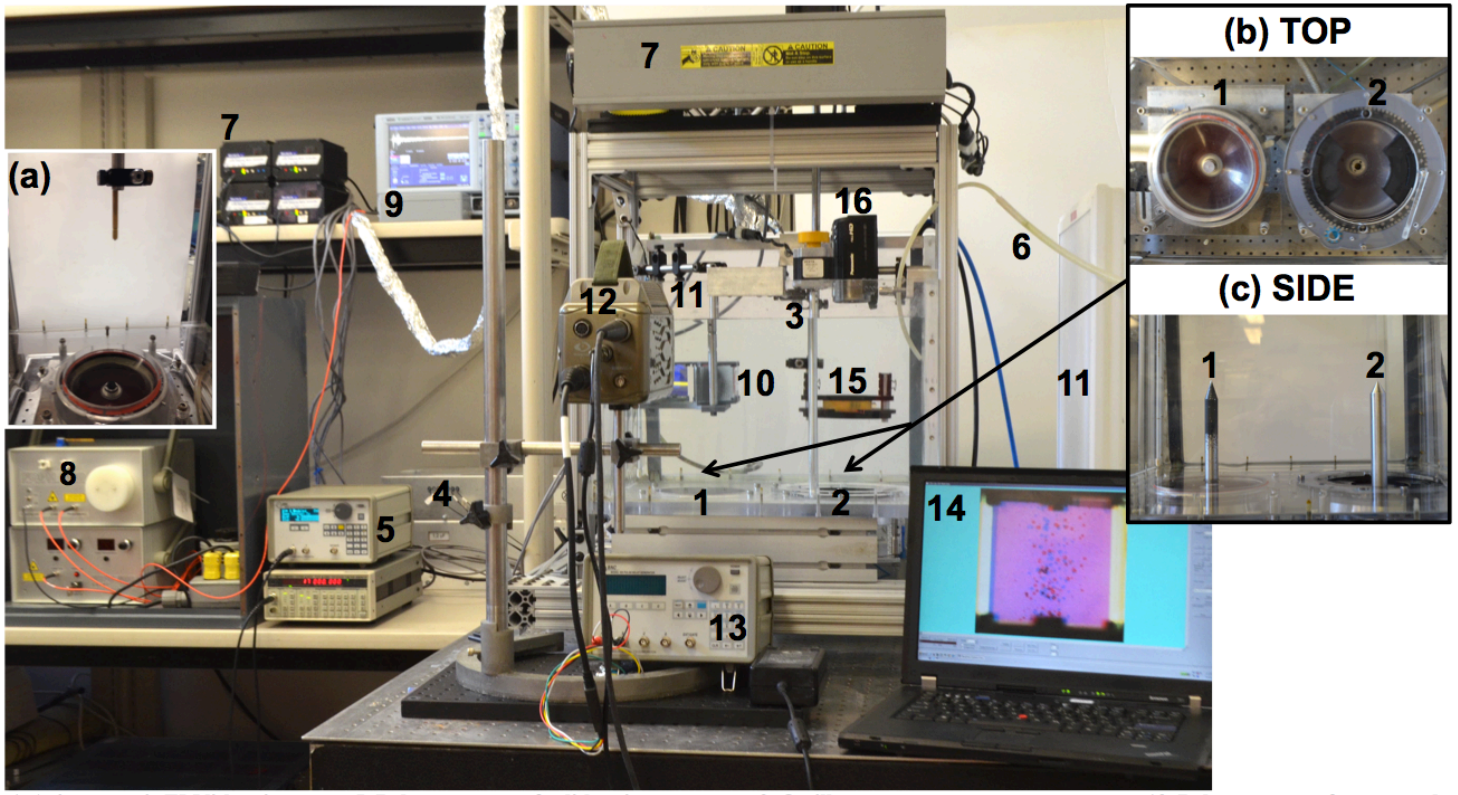

Figure 3.1: Experimental setup including representative positioning of components for acoustic field characterization and stone comminution evaluation. Insert (a) shows fiber optic hydrophone positioning in the focal plane. (b) Top view of the two EM lithotripter setups and (c) side view showing pointers denoting the lithotripter shock wave geometric focus.

3.2.1 Pressure field characterization

Administered shock waves were triggered by a pulse wave generator (BNC Model 555) at a PRF of 0.05 Hz for acoustic field characterization to ensure bubble nuclei between successive shocks have sufficient time to dissolve. Pressure waveforms were measured in free field using a fiber optic probe hydrophone (FOPH 500, RP Acoustics, Leutenbach, Germany). A 3D computer controlled translational stage (VXM-2 step motors with BiSlide-M02 lead screw, Velmex, Bloomfield, NY) was mounted on top of the acrylic water tank allowing precise positioning of the hydrophone fiber tip for field measurements and to easily translate between setups. Hydrophone laser instability introduces 5 – 10 % error in pressure and energy, respectively [89]. The temperature and gas concentration of the water in the tank was maintained between 22 – 25 °C and < 3 mg/L O_2, respectively. A computer controlled MATLAB program was used to position and view real-time unprocessed pressure waveforms throughout the measurements.

3.2.1.1 Axisymmetric acoustic field distribution

Pressure waveforms generated in an axisymmetric field were collected in the lithotripter focal plane (z = 0 mm, 140 mm from the acoustic lens to the focus) along the x-axis and y-axis using step increments of 1 mm between 0 – 12 mm and 2 mm step increments between 14 – 28 mm. Collected pressure waveforms were filtered by a 20 ns temporal window and subsequently averaged at each field position (n = 6). Post-processed pressure waveforms were utilized to calculate the LSW pulse intensity integral *PII(x,y)* by time-integration and to measure the LSW peak pressure p_+ at all field

positions. Because of field symmetry, x or y were replaced by radius r and corresponding calculations along the x-axis and y-axis were averaged. $PII(r)$ and $p_+(r)$ as functions of spatial position were curve fitted with third-order polynomials to calculate BW and integrated parameters. [48]. E_{eff} and $p_{+(avg)}$ within a circular area of radii of R_{IEC} = 6 mm and R_h = 7 mm (stone holder size that is used in Chapter 4) were calculated by

$$E_{Eff} = \int_S PII(r)\, dS \tag{3.2}$$

and

$$p_{+(avg)} = \frac{1}{\pi R^2} \int_S p_+(r)\, dS \tag{3.3}$$

where $PII(r)$ is calculated by

$$PII(r) = \int_{t_1}^{t_2} \frac{p(t,r)^2}{Z_w} dS. \tag{3.4}$$

The acoustic impedance of water $Z_w = \rho_w c_w$ and integration bounds t_1 and t_2 correspond to the point where the pressure first exceeds 10% of the peak pressure and to the zero-crossing point following the secondary compression phase, respectively. Integrated parameters E_{eff} and $p_{+(avg)}$ were numerically calculated by extrapolating a Cartesian coordinate grid space (x_i, y_j) from the curve fitted data previously described. E_{eff} and $p_{+(avg)}$ were calculated within a circular meshed area of radius R_{IEC} = 6 mm and R_h = 7 mm by

$$p_{+(avg)} \approx \frac{\sum_{i=0,j=0}^{\left(\frac{x_i}{\Delta x}\right)^2+\left(\frac{y_j}{\Delta y}\right)^2<{R_h}^2} p_+\left(\frac{x_{i+1}-x_i}{2}, \frac{y_{j+1}-y_j}{2}\right)(\Delta x \cdot \Delta y)}{\sum_{i=0,j=0}^{\left(\frac{x_i}{\Delta x}\right)^2+\left(\frac{y_j}{\Delta y}\right)^2<{R_h}^2} (x_{i+1}-x_i)\cdot(y_{j+1}-y_j)} \tag{3.5}$$

and

$$E_{Eff} \approx \sum_{i=0,j=0}^{\left(\frac{x_i}{\Delta x}\right)^2+\left(\frac{y_j}{\Delta y}\right)^2<{R_h}^2} PII\left(\frac{x_{i+1}-x_i}{2}, \frac{y_{j+1}-y_j}{2}\right)(\Delta x \cdot \Delta y). \quad (3.6)$$

A step size of 1 mm yielded a numerical area of integration ~16 – 18% smaller than the analytical area of integration; therefore, refinement of experimental data was necessary to closely match the circular area of integration. A spatial step size of $\Delta x = \Delta y = 0.1$ mm was used to closely match the analytical area calculation with a less than 2% difference. Based on an experimental hydrophone step size of 1 mm, an experimental error of ± 9 – 10% was calculated for E_{eff} and $p_{+(avg)}$ [Appendix B].

3.2.1.2 Non-axisymmetric acoustic field distribution

In the non-axisymmetric pressure field, the entire focal plane was scanned in a rectangular grid within bounds $-22 \leq x \leq 22$ mm and $-28 \leq y \leq 28$ mm using 1 mm steps if $|x| \leq 10$ mm and $|y| \leq 12$ mm and 2 mm steps for all other field positions. Collected pressure waveforms were filtered by a 20 ns temporal window and subsequently averaged at each field position (n = 5). Acoustic field parameters $p_+(x,y)$ and $PII(x,y)$ were linearly interpolated using experimental measurements [Figure 3.2(a, d)] creating a refined grid with square cell sizes of $\Delta x = \Delta y = 0.1$ mm (cell area, da = 0.01 mm^2) matching the axisymmetric acoustic field numerical spatial size. Experimental data of step size 1 mm [Figure 3.2 (b, e)] was refined to a 0.1 mm x 0.1 mm grid size [Figure 3.2(c, f)] thus approaching the circular area of integration with a less than 2% difference. E_{eff} and $p_{+(avg)}$ were calculated within a circular refined meshed area of radius R_{IEC} = 6 mm and R_h = 7 mm by Equation 3.5 and 3.6, respectively.

In addition, BW_x and BW_y were calculated as described for the axisymmetric source in section 3.2.1.1.

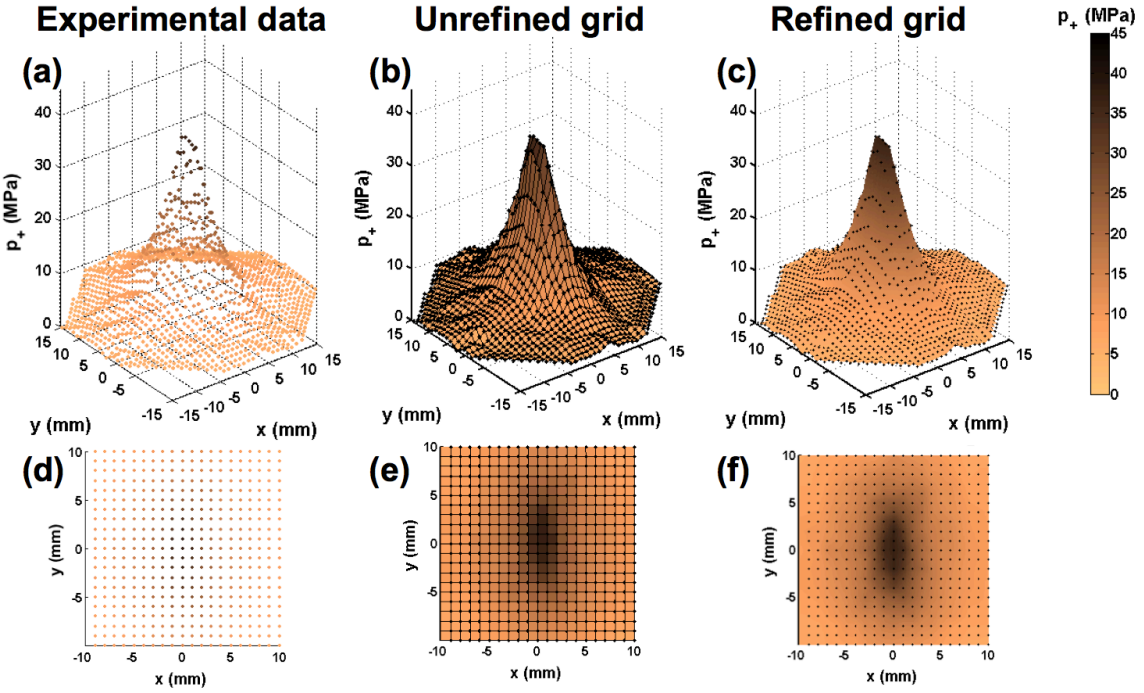

Figure 3.2: Representative focal plane scan of peak pressure for L_1+M_{8025}. (a, d) Experimental measurements recorded at 1 mm steps were converted to a (b, e) grid before linearly interpolating data into a (c, f) refined grid of 0.1 mm steps before numerical integration.

3.2.2 Stereoscopic high-speed imaging of cavitation

Axisymmetric and non-axisymmetric bubble density distributions in the focal zone, centered around the lithotripter focus, were captured by using a stereoscopic high-speed imaging technique developed recently [90].

3.2.2.1 Optical imaging setup

Optical components including mirrors, color filters and a dichroic beam-splitter were mounted using a custom 3D model printed plastic frame (Dimension 1200,

Stratasys, Eden Prairie, MN). The optical system was positioned in the water tank [Figure 3.1] to image two projections (*y*-*z* and *x*-*z*) of the 40 × 40 × 40 mm volume of interest simultaneously as seen in Figure 3.3.

Two 60 × 60 cm (width × height) LED diffuser panels (HCL-FLT8N-0600A0-F1, ATG Electronics Corp., Rancho Cucamonga, CA) of color temperatures T_Y = 2800 – 3200K and T_X = 5500 – 6500K were positioned in the *x*-*z* and *y*-*z* planes for back illumination. Furthermore, two 50 × 75 mm mirrors (M1 and M2, NT480451 Edmund Optics, Barrington, NJ) reflected *y*-*z* and *x*-*z* optical projections through a red (F1) and blue filter (F2) (additive filter set C46-140 Edmund Optics, Barrington, NJ). Color-coded projections were superimposed by a beam-splitter (BS, 50R/50T, 62-882, Edmund Optics, Barrington, NJ) and captured simultaneously by a high-speed color camera (Phantom v.7.3, Vision Research) with a 90 μs exposure time. The camera was externally triggered by a digital delay-pulse generator (565-2C-H-E, Berkeley Nucleonics Corp., San Rafael, CA) and recorded 10 frames per lithotripter shock at a frame rate of 10,000 frames per second. A 50 mm lens (f/1.4, Micro-Nikkor, Nikon Corp., Chiyoda, Tokyo) was used, providing a resolution of 0.26 mm/pixel and a depth of field greater than 20 mm. The interaction between individual bubbles was minimized by administering shocks at a slow PRF (= 0.05 Hz), which provided sufficient time for residual bubble nuclei to re-dissolve into the fluid [91].

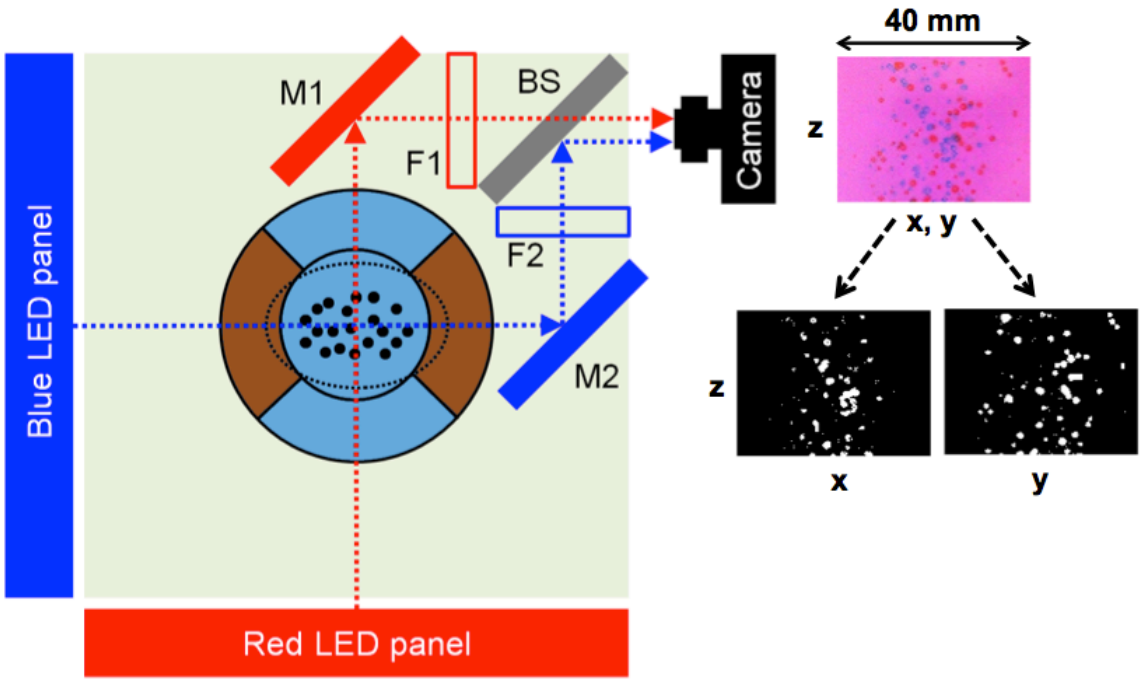

Figure 3.3: Top view schematic diagram of the optical setup for stereoscopic imaging of bubble distribution (denoted with black filled circles) produced in the focal volume of the shock wave lithotripter. LED panels of different emitting wavelengths (or colors) were used to distinguish between *y*-*z* and *x*-*z* projections. The projected bubble images in the *y*-*z* and *x*-*z* planes are reflected by mirrors (M1 and M2), respectively, and filters (F1 and F2) subsequently pass red and blue projections to the dichroic beam-splitter (BS) before being recorded simultaneously by a digital color camera. Captured images are post-processed to separate *y*-*z* and *x*-*z* projections.

3.2.2.2 Post-processing of captured images

High-speed imaging data were post-processed in MATLAB to separate color-coded projections corresponding to *y*-*z* and *x*-*z* grayscale images [Figure 3.3]. The grayscale images were further converted into binary ("black and white") images to isolate bubble boundaries following a previously described protocol [92]. The distribution of cavitation activity was calculated by measuring the density of black pixels in a square region of interest defined by $-15 < z < 15$ mm (height) and $-20 < x, y < 20$ mm (width).

The data were recorded during 150 successive lithotripter shots and were integrated over z to collect sufficient statistics of the cavitation probability. Captured frames corresponding to maximum bubble expansion (~250 μs post-trigger), maximum bubble density, were extracted from each shock's image sequence. Three-parameter Gaussian curve fitting

$$F(x) = \mathrm{P1}\ \mathrm{e}^{-\left(\frac{x-P2}{P3}\right)^2} \tag{3.7}$$

$$F(y) = \mathrm{P1}\ \mathrm{e}^{-\left(\frac{y-P2}{P3}\right)^2} \tag{3.8}$$

was used to estimate the width of the bubble cluster (*P2-x*, *P3-y*) in the focal volume. By adjusting the parameter *P1*, the areas under each Gaussian curve were normalized. The beam width of cavitation BW_{cav}, defined by the width from the maximum cavitation activity to the half maximum value, was calculated for all setups along the *x-z* and *y-z* planes.

3.3 Acoustic field results

Acoustic field characterization results for non-axisymmetric pressure distributions generated by L_2+M_{8025} and L_2+M_{9030} is are compared with the axisymmetric field produced by L_1. Though multiple source charging voltages were investigated for the upgraded non-axisymmetric setup [Appendix C], conditions that yielded equivalent focal region acoustic energy within a circular area of R_{IEC} = 6 mm are presented in detail in this chapter. It was found that to produce clinically relevant and equivalent acoustic pulse

energies in the geometric focal plane in all setups, L_1 was operated at 14 kV and L_2+M_{8025} and L_2+M_{9030} were operated at 15.8 kV and 17 kV, respectively

3.3.1 Axisymmetric and non-axisymmetric pressure field distributions

Figure 3.4(a–c) shows average pressure waveforms generated by L_1 (a), L_2+M_{8025} (b) and L_2+M_{9030} (c). Representative field positions include the focal point (offset by 50 MPa) and off-axis positions of 4 mm (off set by 20 MPa) and 8 mm (no offset) along the *x*-axis (dashed) and *y*-axis (smooth line). Off-axis pressure waveforms were measured at (+) and (-) 4 mm and (+) and (-) 8 mm and were averaged. At the focus, L_1 delivers a p_+ = 44.1 MPa which is >15% higher than that of L_2+M_{8025} (38.2 MPa) and L_2+M_{9030} (36.8 MPa). Similar trends are observed for the shock wave's tensile phase measured at the focus; p_- = -10.6 MPa for L_1 with a slightly reduced strength of -10.4 (L_2+M_{8025}) and -10.1 MPa (L_2+M_{9030}) observed with masks.

L_1 produced an axisymmetric pressure distribution as observed in identical pulse profiles measured along the *x*-axis and *y*-axis. In contrast, L_2+M_{8025} and L_2+M_{9030} produced non-axisymmetric pressure distributions shown in the reduction of p_+ along the *x*-axis compared to the *y*-axis. Though L_1 produces greater p_+ at the focus, L_2+M_{8025} and L_2+M_{9030} deliver greater p_+ at off-axis positions along the *y*-axis. At y = 4 mm (x = 0 mm), p_+ for L_2+M_{8025} is ~18% higher (23.9 MPa) than that of L_1 (20.3 MPa); furthermore, p_+ for L_2+M_{9030} is ~40% higher (28.9 MPa) than L_1. Further off-axis at y = 8 mm (x = 0 mm), p_+ for L_2+M_{8025} and L_2+M_{9030} are >35% and 65% higher than L_1 (9.8 MPa). At off-axis positions along the *x*-axis (from 1 – 6 mm), p_+ of L_2+M_{8025} and

L_2+M_{9030} are ~10% lower than L_1. However, at field positions greater than 6 mm off-axis, p_+ of L_2+M_{8025} and L_2+M_{9030} are ~10% greater than L_1. Measurements of p_- suggest that the tensile component of L_2+M_{8025} is stronger than L_1 and L_2+M_{9030} at all off-axis positions (> 2 mm) along both the *x*-axis and *y*-axis.

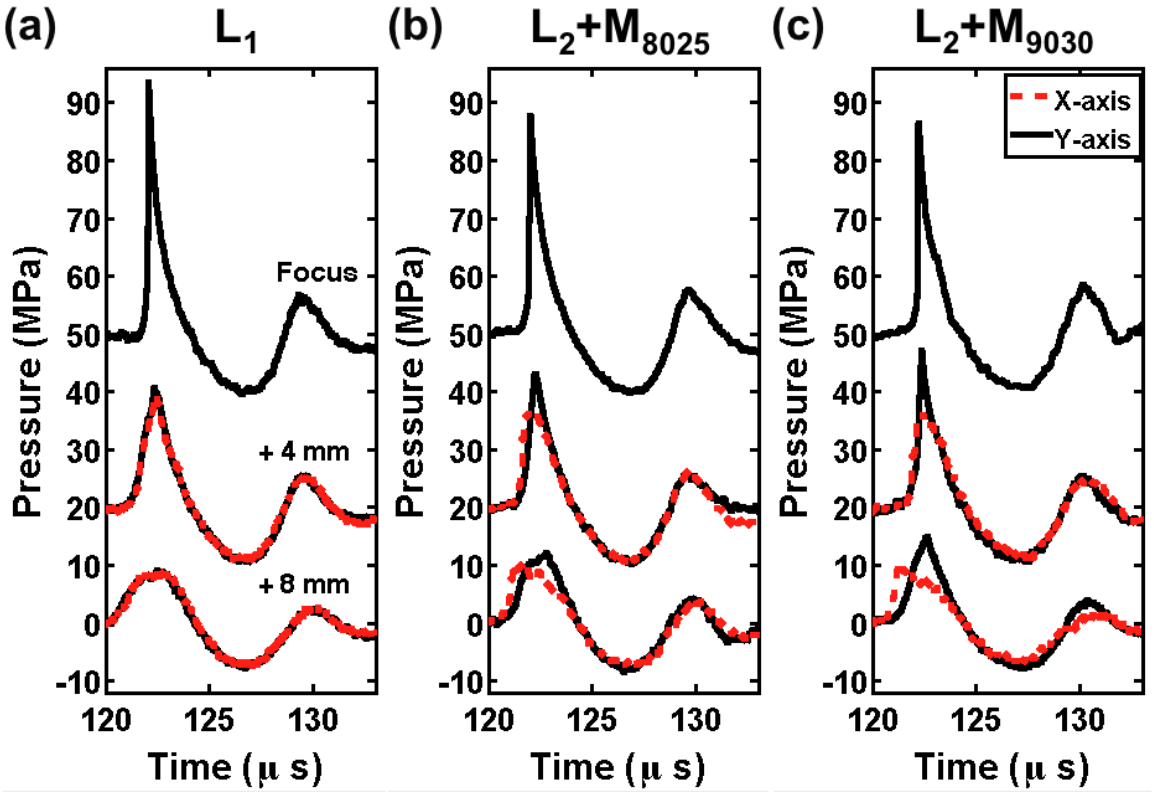

Figure 3.4: Focal plane averaged (n = 6) pressure waveforms of (a) L_1 and mask setups (b) L_2 + M_{8025} and (c) L_2 + M_{9030} measured at the focus (offset by 50 MPa) and at four off-axis positions, 4 mm (offset by 20 MPa) and 8 mm along the x-axis (dashed red line) and y-axis (solid black line).

Two-dimensional averaged p_+ (n = 6) as a function of field position (*x*-axis, open markers and *y*-axis, filled markers) for L_1, L_2+M_{8025} and L_2+M_{9030} is plotted in Figure 3.5(a–c). The implementation of both masks shows a pressure distribution elongated along the *y*-axis. Compared to the axisymmetric p_+ distribution of L_1 [Figure 3.5(a)],

L_2+M_{8025} [Figure 3.5(b)] and L_2+M_{9030} [Figure 3.5(c] have greater p_+ along the *y*-axis and lower p_+ along *x*-axis. To quantify pressure field elongation, the *BW* was measured for all setups along the *x*-axis (BW_x) and *y*-axis (BW_y). The *BW* of L_1 is 7.5 mm, calculated by averaging BWx and BW_y because of symmetry. Similarly, BW_x for L_2+M_{8025} and L_2+M_{9030} are 7.6 and 7.5 mm, respectively. However, BW_y is drastically enhanced along the *y*-axis by implementing an acoustic mask. The BW_y of L_2+M_{8025} (11.4 mm) is ~50% greater than the *BW* of L_1 while the BW_y of L_2+M_{9030} (14.3 mm) is more than 90% greater than the *BW* of L_1.

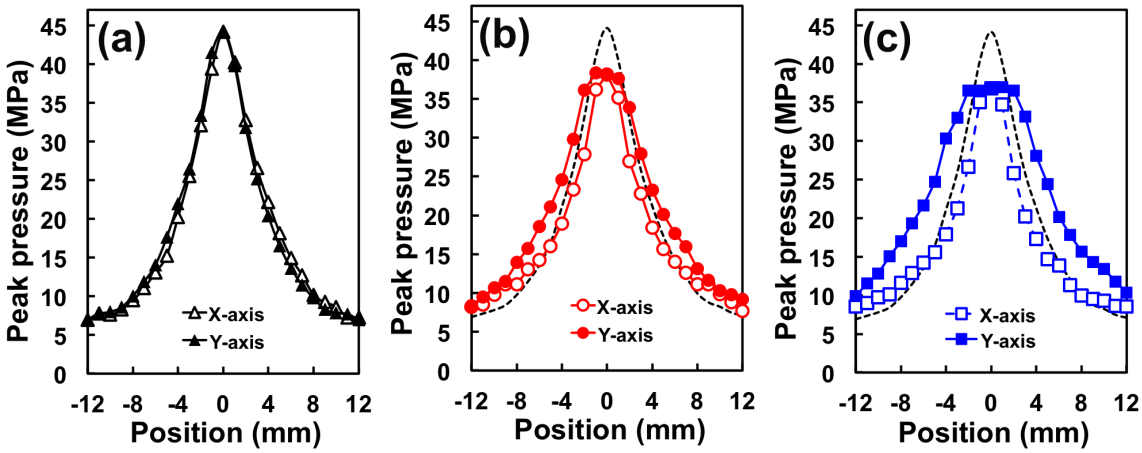

Figure 3.5: Averaged peak pressure p_+ (n = 6) of (a) L_1, (b) L_2 + M_{8025} and (c) L_2 + M_{9030} as a function of field position along the *x*-axis (open markers) and *y*-axis (filled markers). The black dashed line on (b) L_2 + M_{8025} and (c) L_2 + M_{9030} corresponds to the p_+ curve (average of *x*-axis and *y*-axis measurements) of L_1. Experimental measurement yielded standard deviation of < 3 MPa.

Contour plots (0 MPa, white – 45 MPa, black) of averaged p_+ (n = 4) in the focal plane (z = 0 mm) are shown in Figure 3.6 to visualize acoustic fields particularly non-axisymmetric pressure distribution. Though complete grid measurements were not collected for L_1, the contour plot was constructed by extrapolating an axisymmetric

distribution from average measurements along the *x*-axis and *y*-axis [Figure 3.6(a)]. Contour plots show an approximately ellipsoidal pressure distribution for non-axisymmetric fields [Figure 3.6(b) and (c)] and a greater eccentricity for L_2+M_{9030} than L_2+M_{8025}.

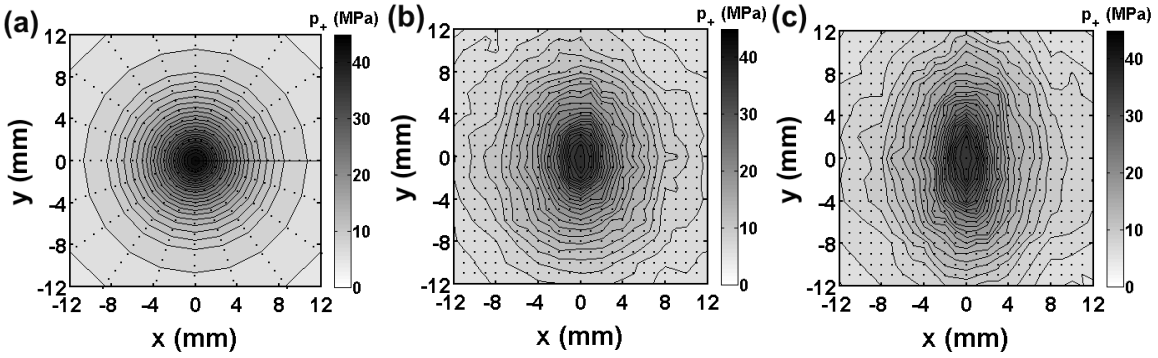

Figure 3.6: Contour plots of averaged p_+ (n = 5) in the geometric focal plane (z = 0 mm) of (a) L_1, (b) L_2 + M_{8025} and (c) L_2 + M_{9030}. Black dots in (b) and (c) correspond to experimental measurement positions.

3.3.2 Cavitation distribution in the focal zone

Figure 3.7 shows cavitation bubble distribution in the focal zone (width x height, 40 mm x 30 mm) corresponding to maximum bubble expansion (t = 250 us) in the *x*-*z* and *y*-*z* planes. The Gaussian fitting of bubble density distributions indicates that L_1 generates an approximately axisymmetric bubble cluster ($BW_{Cav\text{-}x}$ = 8.8 mm, $BW_{Cav\text{-}y}$ = 9.4 mm) [Figure 3.7(a)]. In comparison, L_2+M_{8025} produces a non-axisymmetric bubble cluster elongated to $BW_{Cav\text{-}y}$ = 12.2 mm with an elongation of 1.5 as compared to $BW_{Cav\text{-}y}$ = 8.1 mm [Figure 3.7(b)]. Lastly, L_2+M_{9030} generates a non-axisymmetric bubble cluster that is less dense but covers more focal volume ($BW_{Cav\text{-}x}$ = 10.9 mm, $BW_{Cav\text{-}y}$ = 17.9 mm) than the aforementioned fields. The bubble clusters in the upgraded lithotripters span a

significantly greater area; however, the lithotripter with L_2+M_{9030} produces a broader but less dense bubble cluster possibly implicating a possibly more effective and safer cavitation field for treatment. It is important to note that the depth of field of 20 mm may limit the results collected for L_2+M_{9030} and L_2+M_{8025} in the *x-z* plane as the cumulative bubble activity would not be visualized since it extends up to ± 20 mm from the focus. Therefore, we may expect the peak for L_2+M_{9030} along the plane to have a higher peak cavitation activity similar to L_2+M_{8025} though not captured in these results.

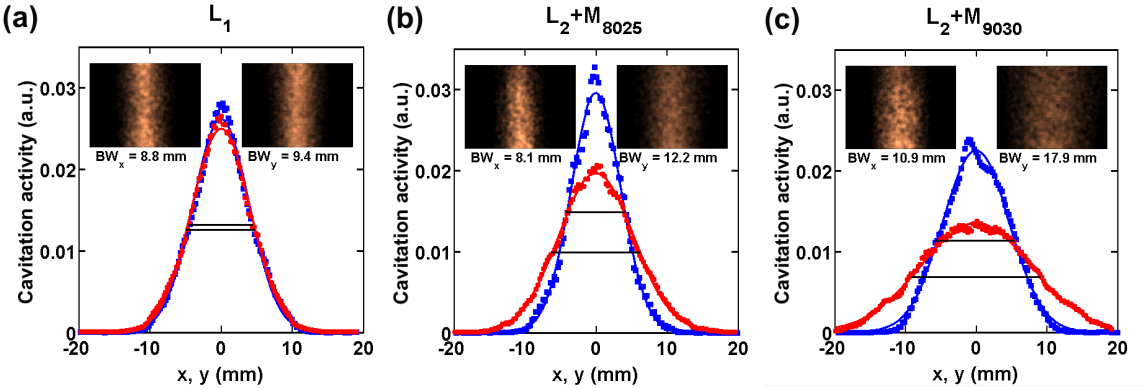

Figure 3.7: Cavitation activity in the x-z (red circles) and y-z (blue squares) planes for (a) L_1, (b) L_2 + M_{8025}, (c) L_2 + M_{9030}. The full width at half maximum of the cavitation field is measured from Gaussian curve fitting (continuous lines). Inserts show the result of the summation of cavitation activities for 150 shocks in the x-z plane (upper-left) and y-z plane (upper-right). Inserts are scaled down to 0.25X of the cavitation activity along the x-axis.

3.3.3 Investigation of peak average pressure and effective acoustic energy at different field positions in the focal plane

Figure 3.8 shows critical acoustic field parameters as a function of stone treatment position (x_h, y_h). $p_{+(avg)}$, $|p_{-(avg)}|$, and E_{eff} are quantified within the stone holder (R_h = 7 mm). As seen in Figure 3.8(a), $p_{+(avg)}$ for all setups are approximately equal at the focus (~20.5 MPa) and holder positions centered at x_h and y_h = 4 mm (~18 MPa). As the stone

holder position diverges further from the focus, $p_{+(avg)}$ is greater at $y_h > 4$ mm compared to $x_h > 4$ mm for both mask designs. $p_{+(avg)}$ for L_2+M_{9030} is minimally higher than L_2+M_{8025} at $y_h > 4$ mm while $p_{+(avg)}$ for L_2+M_{9030} is minimally lower than L_2+M_{8025} at $x_h > 4$ mm. The axisymmetric field, L_1, delivers the lowest $p_{+(avg)}$ at all treatment positions greater than 4 mm as compared to both mask setups. Finally, $p_{+(avg)}$ of both masks converge to ~7.5 MPa at treatment positions, along both axes, greater than 14 mm indicating that differences critical acoustic field differences are observed up to 12 mm from the focus. To further delve into acoustic field quantification, $|p_{-(avg)}|$ calculations are shown in Figure 3.8(b). Trends vary slightly from $p_{+(avg)}$ as observed in L_2+M_{8025} delivering the strongest $|p_{-(avg)}|$ at treatment positions $y_h < 14$ mm. This result is in accordance with the quantified cavitation activity showing that L_2+M_{8025} delivers the highest density of bubble activity within $y_h < 10$ mm.

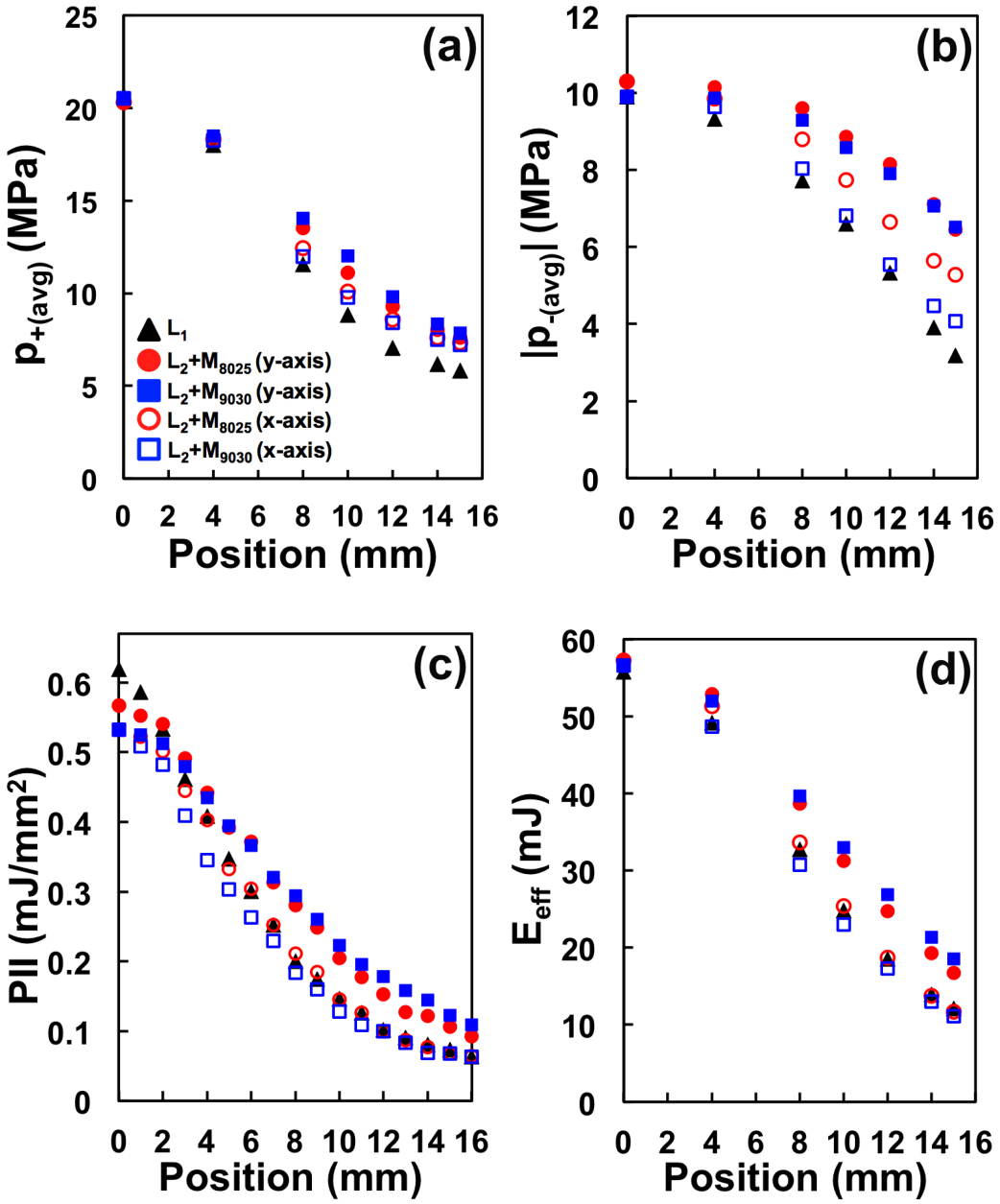

Figure 3.8: Calculated acoustic parameters (a) $p_{+(avg)}$, (b) $|p_{-(avg)}|$ (c) *PII* and (d) E_{eff} as a function of stone treatment position in the focal plane along the x-axis (open markers) and y-axis (filled markers) for L_1 (triangles), L_2 + M_{8025} (circles) and L_2 + M_{9030} (squares), respectively. The values of $p_{+(avg)}$, $p_{-(avg)}$ and E_{eff} were calculated within a circular area of R_h = 7 mm.

Figure 3.8(c) shows *PII* generated by each setup with results demonstrating similarities similar to p_+ trends previously observed in Fig. 3.5(a–c). At the focus, L_1 delivers the greatest *PII* (0.62 mJ/mm^2) as compared to 0.57 and 0.53 mJ/mm^2 delivered by L_2+M_{8025} and L_2+M_{9030}, respectively. As field positions exceeding 2 mm from the focus, *PII* of L_1 declines sharply below *PII* generated by both mask setups, particularly along the *y*-axis. *PII* results for L_2+M_{8025} and L_2+M_{9030} oscillate at positions $2 < y_h < 10$ mm possibly indicating minimal variance between setups. However, at $y_h \geq 10$ mm, *PII* of L_2+M_{9030} is greater than all other setups. For treatment positions $4 < x_h < 15$, approximately equivalent *PII* is delivered for L_1 and L_2+M_{8025} with L_2+M_{9030} being minimally lower.

As an extension of *PII* results, Figure 3.8(d) shows E_{eff} delivered to the stone holder at several treatment positions. At the focus, all setups deliver approximately equal E_{eff} (56 – 57 mJ), similar to trends observed with $p_{+(avg)}$. However, at $y_h = 4$ mm, L_2+M_{8025} and L_2+M_{9030} produce the greatest accumulated acoustic energy (52 – 53 mJ) in the stone holder as compared to other conditions (< 48 MJ). As previously observed in trends of $p_{+(avg)}$, there is a similar transition of mask design results as observed when data for L_2+M_{8025} declines below L_2+M_{9030} between $8 < y_h < 10$ mm. Trends are relatively stable at positions greater than 10 mm. E_{eff} of L_2+M_{9030} is greater ~2.0 – 2.5 mJ (10 – 17%) than L_2+M_{8025} (*y*-axis). At $x_h > 6$ mm, *PII* and E_{eff} for mask designs and L_1 are relatively similar (<5% difference). Overall, results show that the non-axisymmetric acoustic field generated by the two investigated masks yields higher $p_{+(avg)}$ and E_{eff} at $y_h >$

0 mm. Table 3.1 shows a comparison of measured and calculated critical acoustic parameters from generated by L_1 and mask setups, L_2+M_{8025} and L_2+M_{9030}.

Table 3.1: Critical acoustic field parameters measured at the focus or calculated within a circular area of R_h = 7 mm centered around the focus for L_1, L_2 + M_{8025}, L_2 + M_{9030} operated at 14 kV, 15.8 kV and 17 kV, respectively (equivalent $E_{eff\,(R\,=\,6\,mm)}$).

	E_{eff} (R=6mm) (mJ)	p_+ (MPa)	$p_{+(avg)}$ (MPa)	$\lvert p_- \rvert$ (MPa)	$p_{-(avg)}$ (MPa)	BW_x (mm)	BW_y (mm)	$BW_{Cav\text{-}x}$ (mm)	$BW_{Cav\text{-}y}$ (mm)	PII (mJ/mm^2)	E_{eff} (R=7mm) (mJ)
L_1 14 kV	44.4	44.1	20.6	10.6	9.8	7.5	7.5	8.8	9.4	0.62	55.7
L_2+M_{8025} 15.8 kV	44.9	38.2	20.3	10.4	10.2	7.6	11.4	8.1	12.2	0.57	57.2
L_2+M_{9030} 17 kV	44.5	36.8	20.5	10.1	9.9	7.5	14.3	10.9	17.9	0.53	56.5

3.4 Discussion

Acoustic field characterization results show that the implementation of a mask (aligned on the *y*-axis) above a lithotripter acoustic lens generates a stable and effective method to transform from an axisymmetric to a non-axisymmetric pressure field distribution verifying linear wave approximations (Chapter 2). Moreover, since the maximum deliverable pulse acoustic energy is limited by the risk of tissue injury, this upgraded lithotripter design demonstrates the capability of distributing effective acoustic energy in a non-axisymmetric field to conceivably better match anatomical structures and stone translation during respiratory motion. The upgraded non-axisymmetric acoustic field distribution generated by two masks were compared to that of a clinically relevant axisymmetric pressure distribution at equivalent delivered acoustic energy. In order to deliver equivalent acoustic energy as L_1, mask designs, L_2+M_{8025} and L_2+M_{9030} redistribute energy from the immediate focal area (within 4 mm) to the *y*-axis.

Compared to the high pressure narrow *BW* produced by L_1, mask designs L_2+M_{8025} and L_2+M_{9030} both generate lower pressure fields broadened along the *y*-axis and narrow along the orthogonal *x*-axis. The acoustic field generated by L_2+M_{9030} distributes energy further off-axis producing a broader lower pressure field as compared to L_2+M_{8025}. In addition, by treating stones along the broad pressure distribution of L_2+M_{8025} and L_2+M_{9030}, higher $p_{+(avg)}$ and E_{eff} are delivered to the circular area of a stone holder (R_h = 7 mm) as compared to the corresponding narrow axis of each mask. It is important to note that though masks distribute energy broadly along the *y*-axis, the

acoustic field along the corresponding orthogonal *x*-axis, is approximately equivalent to L_1. The simultaneous visualization of the cavitation cluster in two projections, *y*-*z* and *x*-*z*, reveals that bubble distribution for each setup are generally in line with the pressure distribution observed. The current study and subsequent results are limited in terms of cavitation visualization as the depth of field visualized is less than 20 mm with bubble activity extending up to ± 20 mm away from the focus along the *y*-*z* plane. Therefore, cavitation analysis is specifically limited along the *x*-*z* plane. Further design improvements will enable better cavitation analysis in future studies, which will enhance the risk of tissue injury discussion.

There are several key features of the non-axisymmetric pressure distributions that are believed to enhance stone comminution while concomitantly reducing or at least not increasing tissue injury as compared to the axisymmetric high pressure narrow *BW* of modern lithotripters. First, the enhancement of *BWy* as compared to *BWx* may be more effective for treatment of stones that have directional spreading and translation as a consequence of irregular elongated anatomical structures (ureter and calyces) and respiratory motion. As previous studies have shown a correlation of $p_{+(avg)}$ and E_{eff} to stone comminution [38, 40], it is hypothesized that L_2+M_{8025} will fragment stones more effectively at field positions along the *y*-axis between 2 – 8 mm and L_2+M_{9030} will be more beneficial at positions greater than 8 mm.

Risk of tissue injury is discussed in terms of pulse acoustic energy and cavitation. Within 2 mm from the focus, L_1 delivers high LSW pulse energy as compared to mask

designs possibly implicating higher tissue injury. Masks deliver stronger LSW pulse energy at off-axis positions along the *y*-axis compared to L_1; however, it is believed that these values may be below the threshold for tissue injury. Similarly, bubble activities generated by the masks are redistributed from a highly dense narrow focal zone to a less dense broad zone extending along the y-axis similarly to the pressure distribution. Cavitation is critical for breaking stones into fine fragments [35, 38, 82] but it may also increase the risk of tissue injury [33, 80]. Though the bubble activity generated by L_2+M_{9030} covers a greater volume than L_1 and L_2+M_{8025}, quantification shows that its sparse suggesting that tissue injury risk may be reduced. In contrast, L_2+M_{8025} generates a bubble cloud that is narrower than L_2+M_{9030} with the highest bubble density observed from the *y*-*z* plane as compared to other setups thus it is recommended that this particular setup be further investigated in terms of tissue injury risk. To evaluate stone comminution produced by the non-axisymmetric pressure distribution compared to the axisymmetric field, stones are treated at the focus and at off-axis positions and during simulated respiratory motion (Chapter 4).

4. *In Vitro* stone comminution for performance evaluation of a non-axisymmetric acoustic field

4.1 Background – Respiratory motion

To assess the effects of non-axisymmetric elongated acoustic fields generated by mask design L_2+M_{8025} and L_2+M_{9030} (described in Chapter 2 and 3) on stone comminution, experiments were performed both under static conditions at various lithotripter field positions and during simulated respiratory motion.

First, stones were treated either at the lithotripter focus or off-axis to evaluate the correlation between parameters $p_{+(avg)}$ and E_{eff} (from Chapter 3) and stone comminution. Second, pressure threshold values were determined and subsequently utilized to calculate the effective area of stone comminution for each configuration. This study provides the foundation for more intricate and clinically relevant stone comminution evaluations including simulated respiratory motion with and without clinically relevant stone misalignment.

Accurate and precise positioning of a kidney stone inside a patient is critical for effective stone comminution during clinical SWL. However, several factors such as stone translation due to respiration and fragment spreading during treatment may all contribute to imprecise alignment that may compromise treatment efficacy. In this chapter, the effect of stone translation was investigated using simulated respiratory motion to better bridge *in vitro* experiments to clinically relevant *in vivo* treatment during SWL. Organ motion in the upper abdomen (in particular the kidneys) is caused by

diaphragm contraction downward on the retroperiteneum to create space for lung expansion (inspiration phase) and relaxation, retracting upward as a person exhales (expiration phase) [Figure 4.1]. Although kidney motion may translate in the superior-inferior (SI), anterior-posterior (AP) and lateral directions simultaneously, the predominant displacement is in the SI direction with an excursion distance up to 30 mm for normal breathing and nearly 90 mm for forced breathing [41, 42, 93, 94]. Motion of kidneys during SWL is directly related to patient comfort, type of anesthesia administered and whether ventilation is used to control breathing [95]. It has been shown that general anesthesia helps to yield higher stone comminution compared to sedation, which has been attributed to decreased patient movement from discomfort and respiration [54, 95].

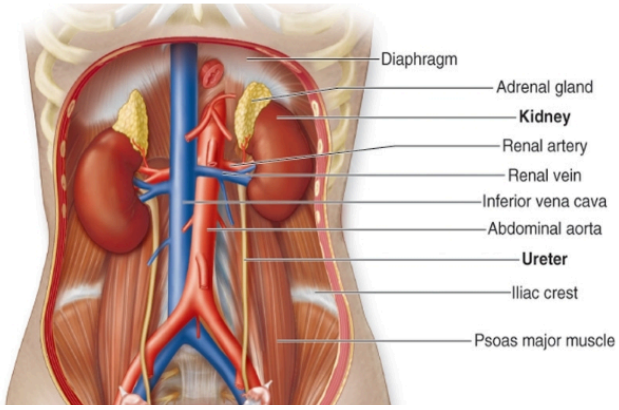

Figure 4.1: Illustration of upper abdomen showing the diaphragm and the kidney and ureter anatomical structure and position [72].

As previously described, ~40% of administered shocks from contemporary lithotripters may miss the target stone due to respiratory motion [46, 50]. In contrast, the original HM3 and some broad beam width / low peak pressure lithotripters have

produced better treatment outcome with higher stone clearance and lower retreatment rates. It is postulated that a broad focal zone may cover the stone trajectory more effectively and consequently increase the percentage of administered shocks to impact on the target stone despite respiratory motion. We hypothesize that the non-axisymmetric pressure field generated by the masks will fragment stones more effectively as it covers the trajectory of stone motion more effectively than its axisymmetric counterpart.

4.2 Materials and methods

Cylindrical stone phantoms, (7 x 7 mm, ⦸ x H) made of BegoStone material with a 5:1 power to water mixing ratio (wave speed c_S = 3148 m/s and ρ_S = 1563 kg/m^3) were soaked in filtered water for ~ 2 hours before SWL treatment [96]. Stone phantoms were placed inside a flat-base Teflon tube holder (R_h = 7 mm) and were precisely aligned or translated with the 3D positioning system (VXM-2 step motor with BiSlide-M02 lead screw, Velmex, Bloomfield, NY). At least six stones were used for each experimental condition. The shockwave source was operated at an output voltage of 14 kV (L_1), 15.8 kV (L_2+M_{8025}) and 17 kV (L_2+M_{9030}), respectively, to deliver equivalent acoustic pulse energy inside the holder in the focal plane for the three different experimental configurations. Masks were aligned with the acoustic barrier positioned along the *y*-axis in all the experiments. After treatment, fragments were collected and dried for more than 24 hours. Fragments < 2 mm (considered passable by patients) were separated using a 2.0 mm grid sieve (No. 10, W.S. Tyler, Mentor, OH) and used to quantify stone comminution efficiency (percent of fragments < 2 mm of the original stone mass).

Results are presented in mean ± standard deviation; statistical analysis was evaluated using either one-way ANOVA to compare more than two groups of data or student's t-test to directly compare two groups of data. Statistical significance was characterized by $p < 0.05$ corresponding to a 95% confidence interval.

4.2.1 Static stone comminution at the lithotripter focus and at off-axis positions

In the first set of experiments individual stones were exposed to 500 shocks delivered at 1 Hz PRF positioned either at the focus (z = 0 mm) or at various off-axis positions in the focal plane along the x- and y-axis (4, 8, 10, 12 and 14 mm) [Figure 4.2].

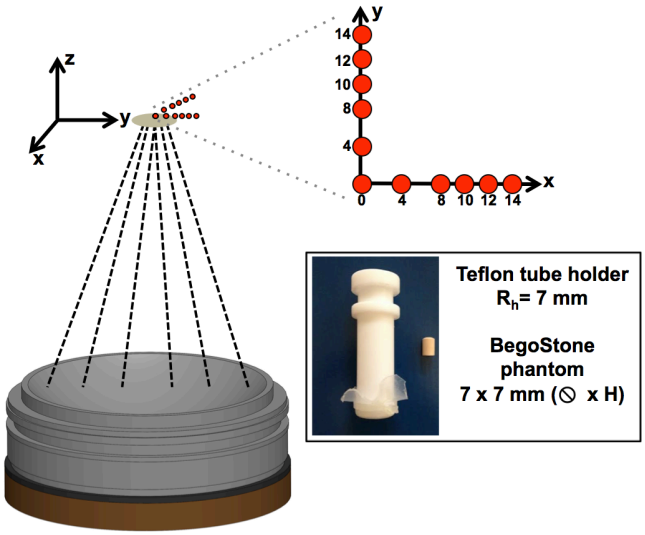

Figure 4.2: Schematic of the treatment positions (red circles) used during static stone comminution tests. A tube holder (R_h = 7 mm radius) and hard BegoStone phantoms (7 x 7, ⦸ x H) were used.

Among the six samples, half were treated in the positive and the other half in the negative quadrant along the x- and y-axis to reduce potential bias in sample alignment. Correlation between stone comminution and $p_{+(avg)}$ (described in section 3.3.3) was

evaluated to determine the pressure thresholds under each setup. The corresponding radii along the x-axis ($r_{x,thres}$) and y-axis ($r_{y,thres}$) for $p_{+(avg)}$ threshold were determined from which the area (A_{thres}), approximated as an ellipse, for effective stone comminution was calculated by

$$A_{thres} = \pi \cdot r_{x,thres} \cdot r_{y,thres}. \tag{4.1}$$

4.2.2 Respiratory motion model

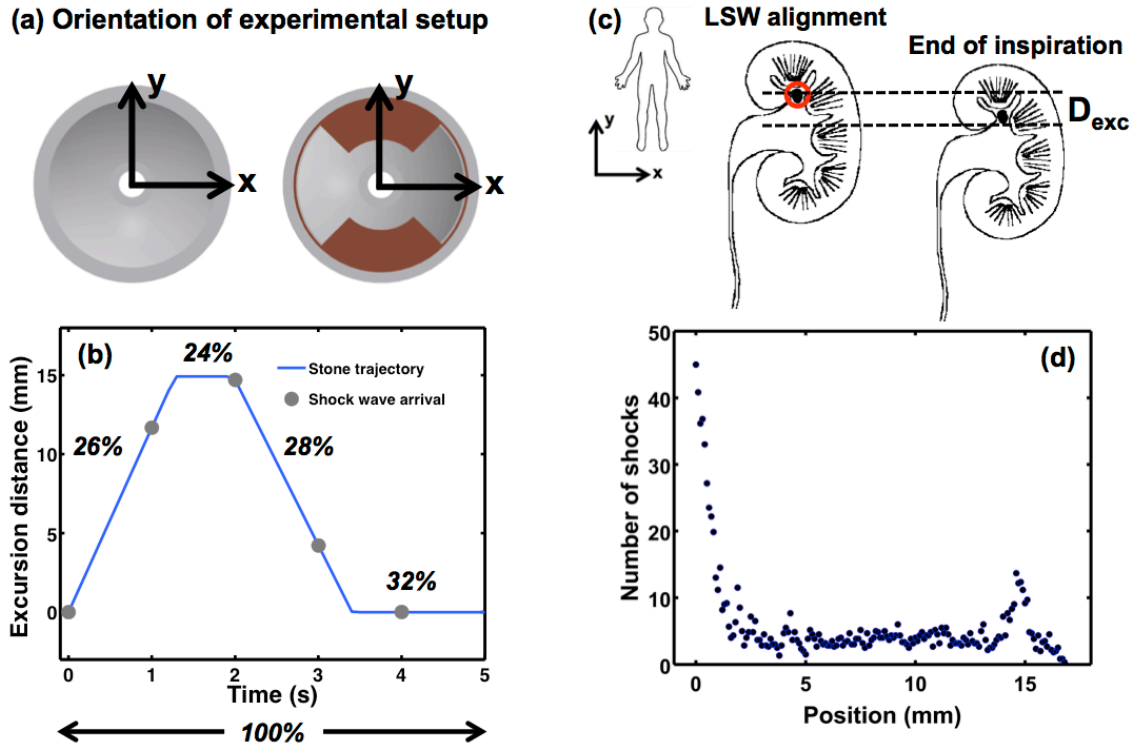

Figure 4.3: (a) Experimental orientation of the axisymmetric and non-axisymmetric setups. (b) An example of absolute displacement of the stone trajectory during simulated respiratory motion. Experimental evaluation includes translating individual stones with an excursion distance of 15 mm either along the x-axis or (c) the y-axis. The lithotripter shock wave propagation z-axis is oriented out of the page. The stone holder is denoted with the red circle, which indicates the alignment of the lithotripter focus at the beginning of the treatment. (d) Representative histogram showing the number of shocks administered at each field position during the treatment.

The second set of experiments were carried out to evaluate stone comminution produced by the axisymmetric and non-axisymmetric fields during simulated respiratory motion [Figure 4.3]. Stones were aligned to the lithotripter focus at the end of patient's expiration phase of breathing to mimic ideal alignment before the treatment and simulated translation began. Stones were moved either along the *x*- or *y*-axis [Figure 4.3(c)] to evaluate the effect of the elongated pressure distribution on comminution. The axisymmetric pressure field produced by the original lens was included. During the experiment, each stone was translated away from the focus (inspiration) and back toward the focus (expiration) using a computer controlled program [Figure 4.3(b)] [48]. A total of 1000 shocks were delivered to the stone at 1 Hz PRF using an excursion distance (D_{exc}) of 15 mm and a breathing rate of 12 breaths per min (BPM), mimicking a normal slow breathing pattern [93, 94, 97]. Furthermore, breath duration was randomly varied within 5% and a low drift of less than 1 mm/breath cycle was employed to introduce a modest variation in the stone translation pattern. During the treatment, a histogram of the number of shocks delivered as a function of stone position was recorded and utilized to quantify dynamic field parameters for the cumulative exposure during the entire treatment [Figure 4.3(d)].

4.2.3 Stone alignment sensitivity test

As a continuation of section 4.2.2, the third set of stone comminution tests included a stone alignment sensitivity test to evaluate the influence of clinically relevant stone misalignment on treatment outcome. Because the stone in a patient is constantly

moving due to respiratory motion, ideal alignment with the lithotripter focus in clinic is difficult. Previous *in vitro* studies utilize almost exclusively ideal alignment scenarios and the impact of potential misalignment has not been investigated.

To this end, an initial stone misalignment was introduced into the same respiratory model described in 4.2.2. Stones were misaligned either along the *x*- or *y*-axis with an off set displacement of 2, 4, 6 or 8 mm in the positive or negative quadrants [Figure 4.4, only positive quadrants are shown].

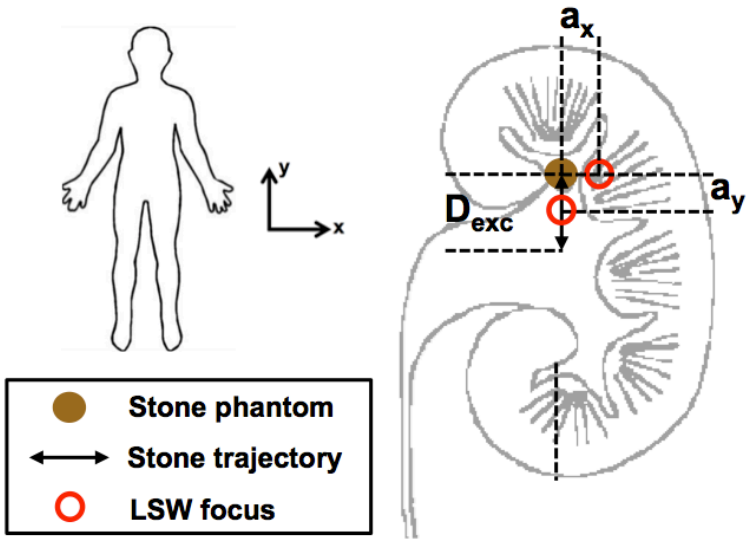

Figure 4.4: Schematic of the alignment sensitivity stone comminution experiment. The lithotripter focus was intentionally misaligned at either a_x or a_x representing misalignment along the *x*- or *y*-axis, respectively. During treatment, stones were always translated at an excursion distance D_{exc} = 15 mm along the *y*-axis.

4.2.4 Correlating dynamic field parameters and translating stones

It has been previously shown that $p_{+(avg)}$ and E_{eff} correlate with stone comminution [38, 40, 98]. This relationship was extended to understand the dynamic treatment process during stone translation. The acoustic field, including bubble activity and stress waves,

administered on the target stone is continuously variant; therefore, the total effective dose of $p_{+(avg)}$ and E_{eff}, were calculated for the duration of the treatment by

$$dose_{eff,p_{+(avg)}} = \sum_{y=a_y}^{y_{thres}} p_{+(avg)}(a_x, y) \cdot dose(a_x, y) \tag{4.2}$$

and

$$dose_{eff,E_{eff}} = \sum_{y=a_y}^{y_{thres}} E_{eff}(a_x, y) \cdot dose(a_x, y) \tag{4.3}$$

where a_x and a_y correspond to the initial misalignment along the *x*- and *y*-axis, respectively. $dose(a_x, y)$ is defined by the number of shocks administered along the respiration axis (*y*-axis) from a_y to y_{max} (= a_y + *drift* + D_{exc}). For each experimental condition, the average of each stone sample's $dose(a_x, y)$ was used for correlating *SC* against effective dose of $p_{+(avg)}$ or E_{eff}. Lastly, y_{thres} corresponds to the field position matching the threshold pressure for stone fragmentation as follows

$$p_{+(avg)}(a_x, y_{thres}) = p_{+(avg)}threshold. \tag{4.5}$$

with the calculated threshold of $p_{+(avg)}$ ~10 MPa.

4.3 Results

4.3.1 Static stone comminution

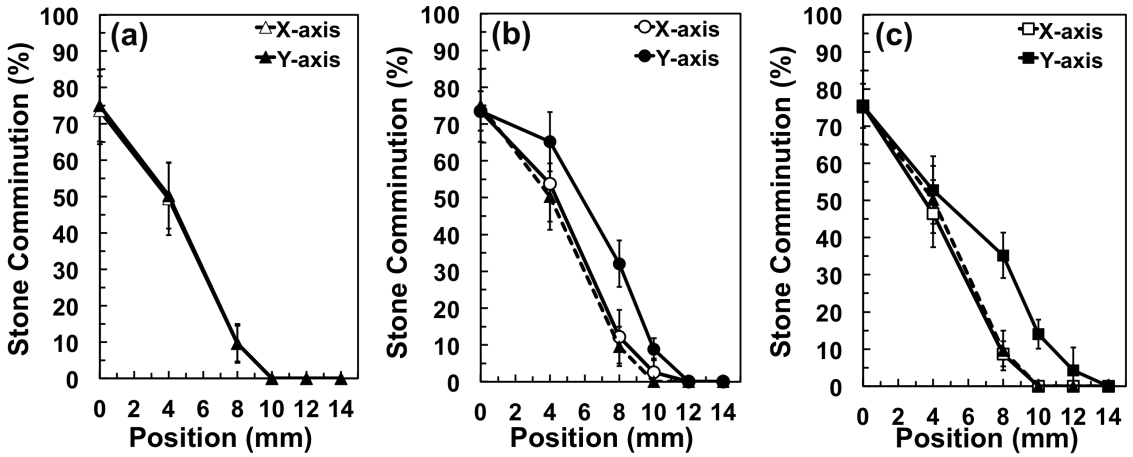

Figure 4.5: Averaged (n = 6) static stone comminution produced by (a) L_1 (triangles), (b) L_2 + M_{8025} (circles), and (c) L_2 + M_{9030} (squares) after 500 shocks delivered to a stone phantom (⦸ x *H*, 7 x 7 mm) in a tube holder (R_h = 7 mm) positioned at the focus and several off-axis positions, 4, 8, 10, 12, and 14 mm (*x*-axis, open markers; *y*-axis, filled markers). The black dashed line in (b) and (c) corresponds to the stone comminution produced by L_1 for comparison.

Figure 4.5 shows stone comminution (*SC*) as a function of the holder's center position, produced by L_1 (a), L_2+M_{8025} (b) and L_2+M_{9030} (c) after 500 shocks. All three lens configurations produce approximately equal *SC* (~73%) at the focus and *SC* in general decreases progressively as the holder moves off-axis. Because of symmetry, *SC* produced by L_1 along the *x*- and *y*-axis are statistically the same ($p > 0.1$) and no *SC* was produced at off-axis positions > 8 mm [Figure 4.5(a)].

In comparison, there is a drastic difference between *SC* produced off-axis along the *x*- and *y*-axis, with both masks significantly enhancing stone comminution along the elongated beam direction [Figure 4.5(b) and (c)]. For example, *SC* produced by using L_2+M_{8025} along the *y*-axis results at off-axis positions of 4 and 8 mm are ~12% and 33%

higher than their counterpart on the *x*-axis, respectively [Figure 4.5(b)]. However, at positions exceeding 8 mm off-axis, the difference in *SC* between the two axes diminishes; no fragmentation was observed at > 12 mm off-axis positions. In comparison, *SC* produced by L_2+M_{9030} is statistically similar at off-axis positions of 4 mm along both axes ($p = 0.29$) [Figure 4.5(c)]. However, *SC* is significantly greater ($p < 0.001$) at 8 mm on the *y*-axis (32.1 ± 6.6%) than on the *x*-axis (8.7 ± 4.3%). In addition, no *SC* occurs at positions of off-axis 8 mm on the *x*-axis but *SC* of 14.0 ± 4.3% and 4.2 ± 6.1% mm were produced at 10 and 12 mm, respectively, on the *y*-axis. The maximally elongated acoustic field of L_2+M_{9030} is capable of fragmenting stones at positions up to 12 mm on the *y*-axis signifying the drastic difference in *SC* effectiveness in the non-axisymmetric field. In addition, there is no statistical difference in *SC* ($p > 0.1$) when treating stone phantoms along the *x*-axis of either L_2+M_{8025} or L_2+M_{9030} as compared to the control setup, L_1.

Along the *y*-axis, both L_2+M_{8025} and L_2+M_{9030} fragment stones more effectively at off-axis positions than L_1. Between the two mask designs, L_2+M_{8025} performs better than L_2+M_{9030} ($p = 0.024$) at 4 mm off-axis positions on the *y*-axis. Although not statistically significant, *SC* produced by L_2+M_{8025} is slightly higher than that produced by L_2+M_{9030} at an off-axis position of 8 mm. At further off-axis positions, y_h = 10 and 12 mm, L_2+M_{9030} fragments stones ~5% greater than L_2+M_{8025}. It is important to note that *SC* is relatively low (< 15%) at an off-axis position of 10 mm on the *y*-axis even with L_2+M_{9030}.

4.3.2 Pressure thresholds of stone comminution and effective stone fragmentation area

Figure 4.6 shows static stone comminution results plotted against $p_{+(avg)}$ calculated within the stone holder in a linear-log scale, with $SC = m \ln(p_{+(avg)}) + b$ [99]. For all three setups, *SC* results were grouped for each condition at different positions along the *x*-axis and *y*-axis, excluding the ones where no fragmentation was produced. Best-fit parameters are summarized in Table 4.1. The $p_{+(avg)}$ thresholds were found in the range of 10.0 to 10.5 MPa from different experimental setups. A one-way analysis of covariance of fitted curves shows that differences in $p_{+(avg)}$ thresholds are not statistically different ($p > 0.1$).

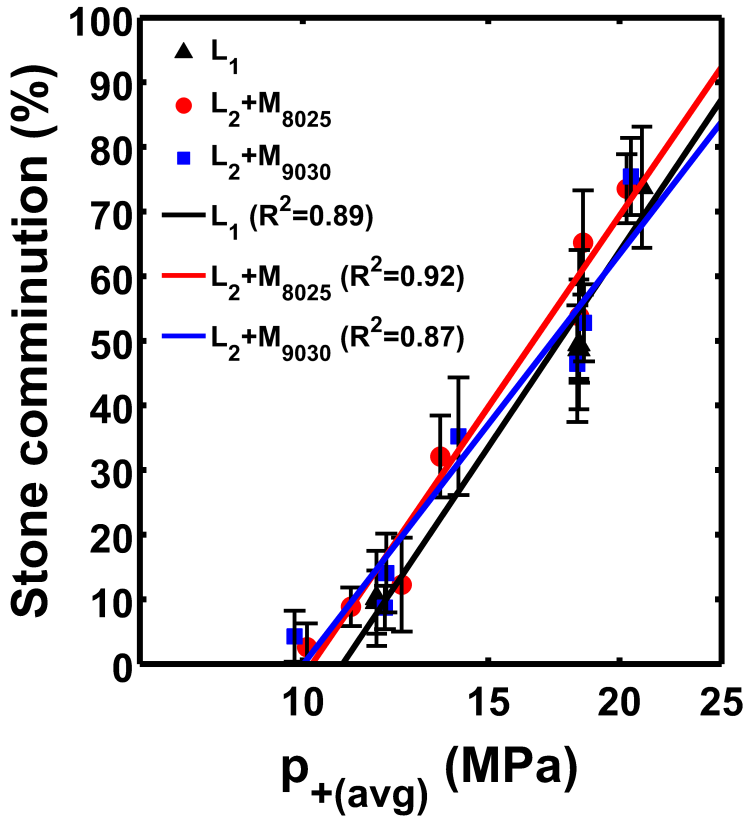

Figure 4.6: Stone comminution (from static focal and off-axis positions) versus average peak pressure ($p_{+(avg)}$) for L_1 (black triangles), L_2+M_{8025} (red circles), and L_2+M_{9030} (blue squares). Logarithmic fits are presented as smooth lines with corresponding R^2 and coefficient values shown in Table 4.1.

The axisymmetric field generated by L_1 is capable of breaking up stones at off-axis positions of $r_{x,thres} = r_{y,thres} = 8.6$ mm from the focus. In comparison, L_2+M_{8025} and L_2+M_{9030} have higher $r_{x,thres}$ of 9.9 and 9.6 mm, and more notably, $r_{y,thres}$ of 11.1 mm and 11.6 mm, respectively. The enlargement of $r_{y,thres}$ with both masks enables stone fragmentation to be produced at off-axis positions up to 30% further from the focus than the original lens. Consequently, the area of fragmentation zone A_{thres} is enlarged from

230 mm^2 for L_1 to 345 mm^2 and 350 mm^2 for L_2+M_{8025} and L_2+M_{9030}, respectively. This significant increase in A_{thres} by more than 40% using the masks may be advantageous when treating stones that can spread or move substantially under the influence of respiration. A_{thres} of L_2+M_{8025} is marginally lower than L_2+M_{9030} but results are within an experimental error of at least 10%.

Table 4.1: Logarithmic curve fitting of stone comminution as a function of peak average pressure in the stone holder (R_h = 7 mm) for L_1, L_2 + M_{8025}, and L_2 + M_{9030}. Confidence bounds of 95% are included for calculated coefficients *m* and *b*. Predicted average peak pressure thresholds for initiating stone comminution are approximately equal for all three setups (p > 0.1).

	SC = m lnx +b		$p_{+(avg)}$ **threshold (MPa)**	R^2	$r_{x,thres}$ **(mm)**	$r_{y,thres}$ **(mm)**	A_{thres} **(mm^2)**
	m	***b***					
L_1 14 kV	105 ± 13	-247± 33	10.5 ± 1.8	0.89	8.6	8.6	230
L_2+M_{8025} 15.8 kV	103 ± 9	-240 ± 25	10.2 ± 1.7	0.92	9.9	11.1	345
L_2+M_{9030} 17 kV	92 ± 12	-211 ± 30	10.0 ± 2.3	0.87	9.6	11.6	350

4.3.3 Stone comminution during respiratory motion

Stones were translated either along the *x*-axis (solid) or *y*-axis (checkered) during simulated respiratory motion experiments to compare the non-axisymmetric pressure field generated by each mask with L_2 with the axisymmetric pressure field of L_1. Stones were treated with 1000 shocks delivered at 1 Hz PRF (n = 6) [Figure 4.7]. Simulated stone motion was operated at an excursion distance of D_{exc} = 15 mm, which is greater than r_{thres} for all setups. In addition, stone translation exceeded the range of cavitation activities for all experimental conditions [in section 3.2.1] except along the *y*-axis of

L_2+M_{8025} and L_2+M_{9030}. In general, results produced under simulated respiratory motion show similar trends with the characterization (p_+, *BW*, and cavitation activity) of the acoustic field. There is no statistical difference between *SC* results produced by L_1 (when translating stones either along the *x* or *y*-axis) and L_2 with masks (translating along the *x*-axis) ($p = 0.32$). However, when stones are translated along the elongated beam direction, *SC* is significantly enhanced. For L_2+M_{8025}, *SC* increases from 60.8 ± 8.6% (*x*-axis) to 73.4 ± 5.4% (*y*-axis) with a statistically significant difference ($p = 0.01$). Similarly, L_2+M_{9030} also produces statistically better *SC* ($p = 0.004$) when stones are translated along the *y*-axis (69.3 ± 6.4%) than along the *x*-axis (57.9 ± 3.2%). There are no statistical differences between *SC* produced by using $L_{2\ with}$ masks when stones are translating along the same axis ($p > 0.1$). Overall, the results demonstrate that by aligning the direction of stone translating with the broad acoustic beam axis, stone fragmentation can be significantly enhanced. Also important to note, the non-axisymmetric pressure distribution produced by L_2 with masks does not compromise *SC* even when stones are translated along the *x*-axis compared to L_1.

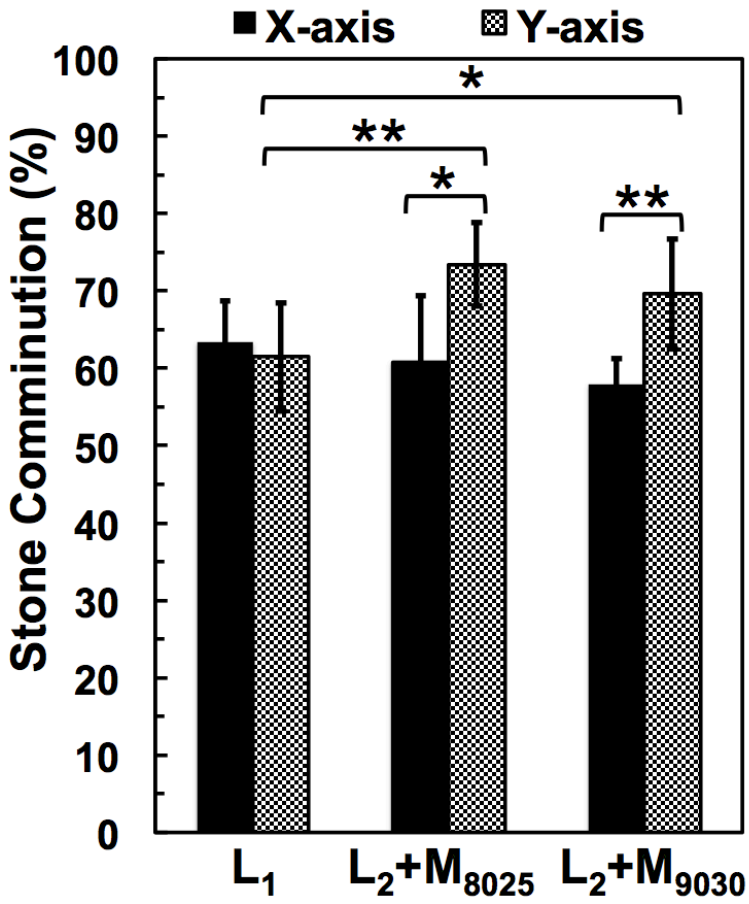

Figure 4.7: Stone comminution (n = 6) after 1000 shocks during simulated respiratory motion with L_1, L_2 + M_{8025} and L_2 + M_{9030}. Stones were treated in a tube holder (R_h = 7 mm) and positioned at the focus and translated either along the *x*-axis (solid fill) or along the *y*-axis (checkered fill) at an excursion distance of 15 mm and 12 BPM. Indicated p-values for comparison are noted as ** < 0.01 and * < 0.05.

Table 4.2 summarizes the effective doses of $p_{+(avg)}$ and E_{eff} [Equation 4.2 and 4.3, respectively] delivered to the stone during simulated respiratory motion under each experimental condition. Effective doses were normalized by the total number of delivered shocks (1000 shocks). It can be seen that L_2+M_{8025} and L_2+M_{9030} deliver a higher effective dose along the *y*-axis for ($p_{+(avg)}$ of 13.0 ~ 13.3.4 MPa and E_{eff} of 36.8 ~

37.4 mJ) than along the x-axis ($p_{+(avg)}$ of 12.2 ~ 12.5 MPa and E_{eff} of 33.2 ~ 34.6 mJ). In addition, the percent of administered shocks delivered within the stone comminution threshold area ($\%shocks_{eff}$) are higher along the y-axis (74 ~ 75%) than along the x-axis (66 ~ 67%). These trends are consistent with the results of *SC* in Figure 4.7.

Table 4.2: *SC* results with corresponding effective doses of $p_{+(avg)}$ and E_{eff} [Equation 4.2 and 4.3] for the entire treatment of 1000 shocks calculated for each experimental condition.

	SC (%)	**dose$_{eff}$, p$_{+(avg)}$ (MPa)**	**%shocks$_{eff}$**	**dose$_{eff}$, E$_{eff}$ (mJ)**
L1, *x*-axis	63.5	11.9	61	32.0
L$_1$, *y*-axis	61.5	11.8	60	32.1
L$_2$+M$_{8025}$, *x*-axis	60.8	12.5	67	34.6
L$_2$+M$_{8025}$, *y*-axis	73.4	13.0	74	36.8
L$_2$+M$_{9030}$, *x*-axis	57.9	12.2	66	33.2
L$_2$+M$_{9030}$, *y*-axis	69.6	13.3	75	37.4

4.3.4 Effects of misalignment on stone comparison

Sensitivity of stone alignment was investigated using L_1 and L_2+M_{8025}. Prior to the SWL, stones were misaligned off the lithotripter focus along the *x*-axis by a_x [Figure 4.8(a)] or *y*-axis by a_y [Figure 4.8(b)] with simulated respiration aligned along the *y*-axis in the experiments. Misalignment data in the positive and negative quadrant for the *x*-axis were averaged at respective positions but were not averaged for the *y*-axis. Since stones were translating along the *y*-axis, the positive and negative quadrant misalignment

positions delivered different acoustic fields thus were not averaged. In general, as the distance of misalignment increases along the *x*-axis, *SC* decreases for both evaluated setups. In comparison, the effect of misalignment on *SC* along the *y*-axis is dependent on the trajectory of stone motion. As misalignment increases by $a_y > 0$ mm, *SC* decreases for both setups; however, misalignment of $a_y < 0$ generates an increase in *SC*. This demonstrates the importance of accurate stone alignment and potential improvement of *SC* by initially aligning stones opposite the direction of respiratory motion to account for stone trajectory during SWL. *SC* shows a substantial reduction 61 ~ 73% (idealized alignment) to < 10% for misalignment at distances of 8 mm. It is also interesting to note that the same degree of misalignment along the *y*-axis [Figure 4.8(a)] (same direction as stone trajectory) reduces stone comminution faster than along the *x*-axis, which is perpendicular to respiration motion [Figure 4.8(b)]. Furthermore, *SC* is greatest for both setups at misalignment positions between -4 mm and -8 mm along the *y*-axis (opposite respiration direction). However, at most individual misalignment positions either along the *x*- or *y*-axis, L_2+M_{8025} produces better SC than L_1.

To investigate the sensitivity of each setup to misalignment, *SC* was normalized by the results with highest *SC* [Figure 4.8, secondary vertical axis). Normalized stone comminution was curve fitted with a polynomial to approximate the misalignment position corresponding to a 50% reduction ($SC_{0.5}$) in comminution. $SC_{0.5}$ of L_2+M_{8025}, along the *x*-axis, is at ± 6.7 mm compared to ± 6.3 mm for L_1. $SC_{0.5}$ along the *y*-axis reduces to positions +5.5 and +4.9 mm for L_2+M_{8025} and L_1, respectively, in the direction

of respiration. However, $SC_{0.5}$ is enhanced to -15 and 13 mm along the *y*-axis. The fitted curves demonstrate the shift of *SC* efficiency if stones are positioned opposite the direction of induced trajectory. To summarize, both acoustic fields are sensitive to initial misalignment of the stone and in particular, in the direction perpendicular to the respiration axis but there is a slight enhancement of *SC* (not statistically significant) if positioned strategically accounting for stone trajectory. Lastly, the non-axisymmetric pressure field of L_2+M_{8025} is more effective in fragmenting stones at all misalignment positions and appears to be less sensitive at all misalignment distances > 2 mm than L_1.

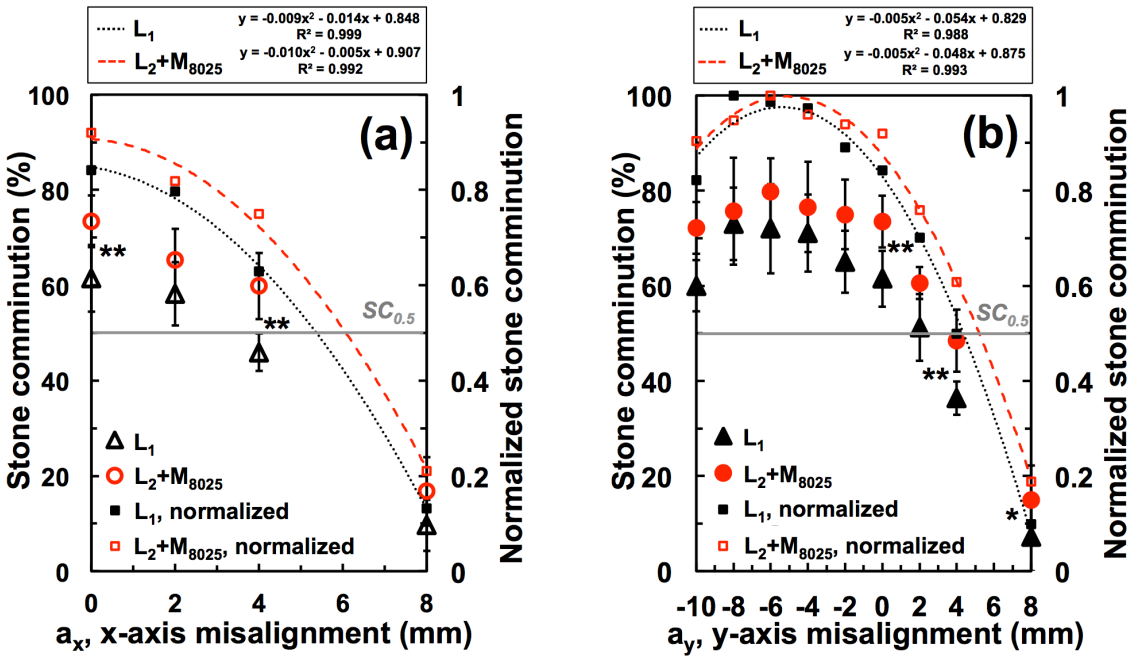

Figure 4.8: Averaged (n = 6) stone comminution after 1000 shocks treated during simulated respiratory motion with L_1 (black triangles) and L_2 + M_{8025} (red, circles). Stones were positioned at the focus and at misalignment positions along the (a) *x*-axis at a_x and (b) *y*-axis at a_y and translated the y-axis at an excursion distance of 15 mm and 12 BPM. Stone comminution results normalized to stone comminution with no misalignment are shown as the open red (, L_2 + M_{8025}) and filled black (L_1) squares. Curve fitting of normalized stone comminution is shown with red

dashed and black dotted lines. Indicated p-values for comparison are noted as ** < 0.01 and * < 0.05.

4.3.5 Correlation of delivered field parameters and stone comminution

Section 4.3.4 demonstrates a clear effect of initial stone misalignment on *SC*. A quantification of the effective dose ($dose_{eff}$) for the critical field parameter $p_{+(avg)}$ may provide additional insight. Figure 4.9 show the $dose_{eff}$ of $p_{+(avg)}$ delivered by L_1 (black triangles) and L_2+M_{8025} (red circles) to the stone holder throughout the treatment. At misalignment positions of a_x [Figure 4.9(a)] and a_y [Figure 4.9(b)], L_2+M_{8025} delivers higher effective doses of $p_{+(avg)}$ to the stone holder during treatment than L_1. Furthermore, the highest doses of $p_{+(avg)}$ when the stone is positioned at $a_y < 0$ thus agreeing with *SC* in Figure 4.8.

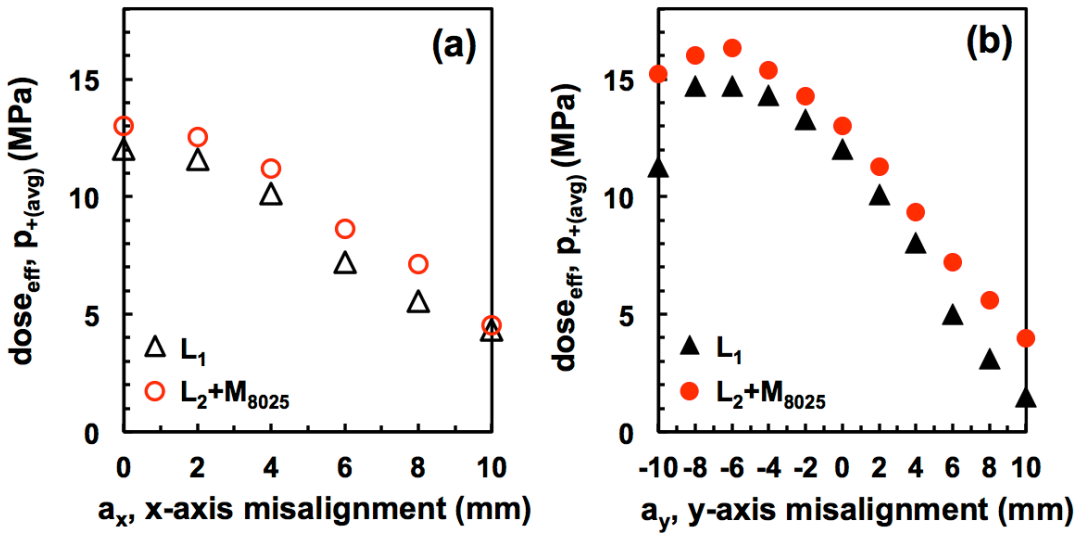

Figure 4.9: Effective dose of $p_{+(avg)}$ delivered during the entire treatment process, plotted against initial misalignment positions along the *x*-axis at a_x (a) or the *y*-axis at a_y (b). for L_1 (black, triangles) and L_2+M_{8025} (red, circles). Stones were translated during respiratory motion along the *y*-axis and the acoustic barrier of the mask was aligned along the *y*-axis.

Figure 4.10 shows the correlation between *SC* and the effective dose of $p_{+(avg)}$ delivered to the stone holder throughout the treatment. Overall, the correlation of *SC* and the effective dose of $p_{+(avg)}$ agrees with the previously shown correlation under static test conditions, demonstrating a pressure threshold for stone fragmentation.

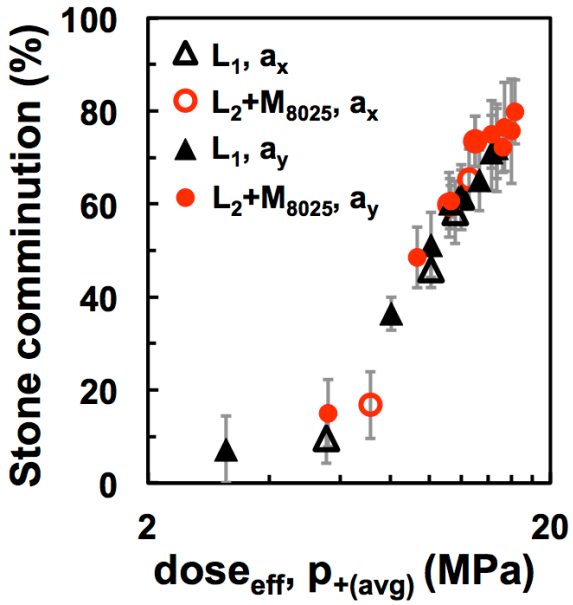

Figure 4.10: Stone comminution (n = 6) results plotted against the effective dose of $p_{+(avg)}$ delivered to the stone holder during the entire treatment of 1000 shocks.

4.4 Discussion

This chapter evaluates the performance of the non-axisymmetric pressure field produced by L_2+M_{8025} and L_2+M_{9030} compared to the axisymmetric field of L_1. First, static stone comminution reveals that both masks produce higher comminution efficiency at treatment positions along the broad pressure distribution (*y*-axis) as compared to L_1. In addition, the moderately elongated pressure field produced by L_2+M_{8025} generates better *SC* within $0 < y < 8$ mm than the maximized elongated pressure field produced by

L_2+M_{9030} (y = 4 mm, $p < 0.05$). At further off axis positions, however, L_2+M_{9030} fragments stones slightly better (~5% better) than L_2+M_{8025}. These results suggest that L_2+M_{8025} performs better nearer to the focus (< 8 mm) and L_2+M_{9030} operates better at further off-axis positions (> 8 mm) suggesting that each mask has a specific range of optimal performance. This optimal range of performance suggests that depending on kidney stone location and factors such as respiratory motion or anatomical structure, acoustic field selection may enable better treatment outcome. For example, if there is minimal respiratory motion or spreading potential, L_2+M_{8025} may be selected for treatment. In addition, there were no statistically significant differences in treating stones at field positions along the narrow pressure distribution of the masks (x-axis) as compared to L_1 thus suggesting that treatment outcome will not be compromised by the elongated acoustic fields. Correlations of static stone comminution against average peak pressure delivered to the stone holder for each setup show a pressure threshold range for fragmentation of ~10.1 – 10.5 MPa ($p > 0.1$). As observed in previous studies, the pressure threshold is a fundamental property of the stone phantom's mechanical properties; therefore, the convergence of data from different acoustic fields is appropriate [38]. From the calculated peak average pressure threshold, the area for effective stone comminution is enhanced by more than ~40% using the masks as compared to L_1.

Subsequent to the aforementioned mechanistic study, the respiratory motion model shows a clinically relevant investigation to the performance of non-axisymmetric acoustic fields. L_2+M_{8025} and L_2+M_{9030} both produce statistically greater stone

comminution, compared to L_1, when stones were translated along the broad pressure distribution axis. By effectively positioning the acoustic field to more closely cover the stone trajectory, stone comminution is enhanced. This correlation is observed in the *SC* plotted against effective dose of acoustic field parameters.

In addition, the alignment sensitivity experiment reveals that though *SC* is either reduced or enhanced when stones are intentionally misaligned before treatment. If misaligned along the *x*-axis or along the *y*-axis in the same direction as the respiratory motion trajectory, stone comminution is reduced for both setups. In comparison, by misaligning the stone opposite the direction of respiratory motion ($a_y < 0$ mm), stone comminution is slightly enhanced for both setups. Stones are generally aligned to the lithotripter focus at the end of patient expiration; however, the target stone is continuously moving thus making ideal alignment challenging. Therefore, misalignment along the respiration axis would be particularly prominent during SWL. This result suggests that by pre-positioning the stone to account for stone trajectory, an optimal treatment strategy may exist. Though this study did not outline an exact protocol for optimal stone alignment, these results strongly demonstrate the importance of initial stone alignment and in particular at an offset away from the focus opposite the direction of stone translation during respiratory motion. L_2+M_{8025} generally maintains greater *SC* for all tested field positions with less sensitivity at misalignment positions off from the focus greater than 2 mm. The reduction in misalignment sensitivity of the mask suggests that it will have more practical advantages in clinic than L_1. Furthermore, it is postulated that

the enhancement of the effective stone comminution area may also counteract the reduction of *SC* observed from other factors, beyond respiratory motion, including stone spreading during the fragmentation process.

5. Steerable non-axisymmetric acoustic field

5.1 Background – Anatomical features of the ureter

This chapter investigates the influence of anatomical features in a ureter model on stone spreading and comminution. Most kidney stones pass down from the renal calyces to the ureter (25 – 30 cm in length), which are segmented into the proximal, mid and distal locations [100]. Because the ureter is normally 3 ~ 4 mm in diameter, stones of sufficient size may obstruct the flow of urine out of the kidney and consequently induce pain. Small stones (< 5 mm) have higher change of passing spontaneously without treatment [101-103]. Approximately ~70% of stones (< 7 mm diameter) in the distal end of the ureter (near the bladder) and ~25% of stones in the proximal end (near the renal pelvis junction) pass without treatment [104, 105].

Treatment outcome of ureteral stones by SWL depends on both the size and location of the stone. After SWL, stone free rates in the range of 68 ~ 90% and 74 ~ 86 % have been reported for stones in the proximal and distal end of the ureter, respectively [106]. Ureteroscopy, a main competing technology to SWL, is considered the treatment of choice for ureteral stones, producing stone free rates of 90 ~ 100% for distal stones and about 74% for proximal stones [107, 108]. Despite this, the non-invasive nature of SWL still renders it as the first-line therapy, which may also be more cost-effective compared to the more invasive ureteroscopic procedures [109, 110]. In this chapter, we will focus on the anatomical structure of the proximal and mid ureter, and evaluate factors that may influence SWL outcome at those locations.

The anatomical structure of the ureter and kidneys naturally varies among patients. Figure 5.1(a) shows a representative radiograph of the upper abdomen (highlighted by contrast agents) showing the collecting system and mid-to-proximal ureter. Although extensive clinical studies have been carried out to investigate SWL treatment on lower pole stones, very little research has been done to correlate ureter anatomy to stone comminution efficiency. One common anatomic feature often investigated is the infundibulopelvic angle (α) [Figure 5.1(b)], measured between a line connecting the central point of the ureter opposite the lower kidney pole to the central point of the renal pelvis and the central axis of the lower pole infundibulum. The value of α measured in healthy adults varies in a large range from 30° to 90° with no statistical differences between kidneys with and without stones [111-114]. Therefore, there is no consensus regarding the angle between the ureter and the respiration axis. We hypothesize that stone comminution in a ureter can be influenced by the spreading characteristics of residual fragments in the surrounding anatomical structure and the continuous transition of the ureter that carries those fragments during respiratory motion. We introduce an angle ϕ (Figure 5.1(c)), which is in the range of 0° to 40° that measures the orientation of the upper ureter with respect to the respiration axis, and evaluate the combined effects of ureter anatomy at a slanted angle ϕ and respiration on stone comminution.

A ureter model was developed and incorporated in a series of experiments to compare stone comminution produced by an axisymmetric vs. a non-axisymmetric

acoustic field. Furthermore, a beam steering protocol that incorporates anatomical and respiratory factors to enhance stone comminution produced by the non-axisymmetric field was developed and compared with that produced by an axisymmetric field.

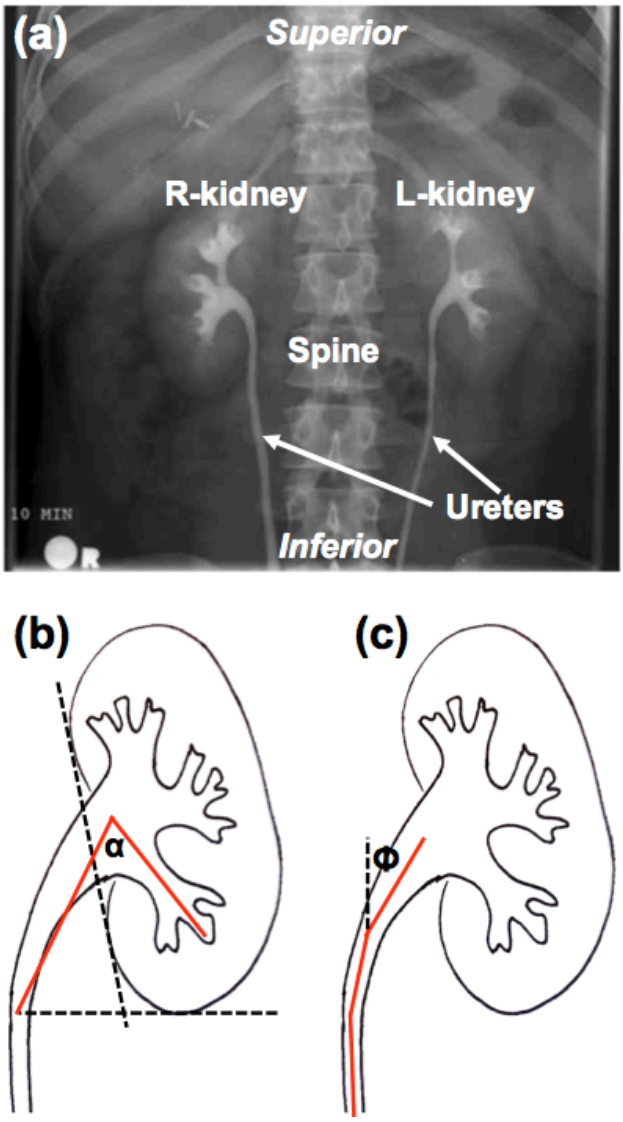

Figure 5.1: (a) Radiograph, with injected contrast agent, of the upper abdomen showing the urinary tract [115]. (b) Representative infundibulopelvic angle α previously investigated. (c) A proposed angle of interest ϕ for this study investigating the angle between the ureter axis and vertical axis of respiration varies along the location of the ureter.

5.2 Methods and materials

This section contains three parts. First, the apparatus to control the steering of the non-axisymmetric acoustic field was expanded from the static mask design described in section 2.4.2. Second, a ureter model was designed to mimic *in vivo* anatomical structure. Third, stone comminution experiments were carried out to compare treatment efficiency produced by the axisymmetric vs. the steerable, non-axisymmetric acoustic field.

5.2.1 Steerable mask design assembly

A gear system was designed to steer (i.e., rotate) the non-axisymmetric acoustic field on-command via a motor control system, which was incorporated with the static mask design. Figure 5.2 shows both the computer aided design of different components of the gear system (a – d) and the images of the experimental assembly (e – h). The design was carried out in SolidWorks and the components were cut from acrylic sheets by a universal laser, including 1) the mask (described in 2.4.2), 2) a large 90-tooth gear, 3) a small 10-tooth gear, 4) an adapter for holding the gears in place, and 5) a top piece to secure the mask design in position. Screws were used to secure the adapter and top housing parts to the acrylic water tank in order to maintain gear alignment. The small and large gears were cut from 2 mm thick acrylic sheets. An aluminum rod, connected to a rotation system (VXM-2 step motor with BiSlide-M02 lead screw, Velmex, Bloomfield, NY [Figure 5.2(e)], was used to rotate the small gear [Figure 5.2(f)]. The rotation of the small gear drove the rotation of the large gear that is secured to the mask.

In addition, a ball-locking system was designed to precisely lock the mask in specific positions [Figure 5.2(g)]. This was system was designed to be able to freely rotate the mask by rotation of the gears; however, the ball-locking system provided 32 secure positions (every 10°), which is beneficial if treating at static mask positions. Finally, a MATLAB program was written to control the rotation of the mask.

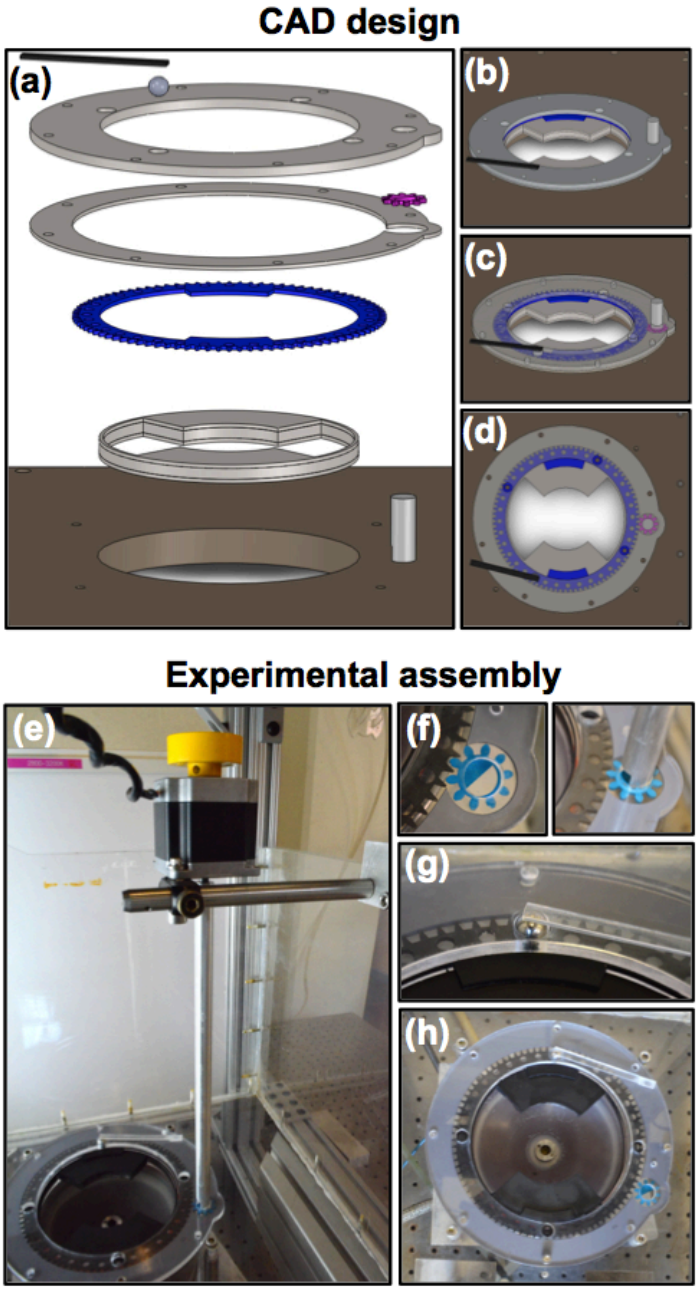

Figure 5.2: (a) Computer-aided design schematic of the components of the gear assembly to steer the acoustic field visualized with an (b) isoview, (c) transparent isoview and (d) top view. (e) Experimental setup of the steerable beam design rotated by (f) a gear system and locked in discrete positions by (g) a ball-lock feature. (h) Top view of the gear assembly to rotate the mask.

5.2.2 Ureter model

Figure 5.3 shows the ureter model specifically designed for this study. Two materials for the ureter model were evaluated: silicon rubber and polyurethane rubber. Though both materials have similar properties, polyurethane rubber was ultimately selected based on design criteria including comparable acoustic properties to soft tissue, ability to withstand thousands of shocks without degradation, and nearly complete transparency for imaging of stone fragmentation during treatment. The ureter model was made of polyurethane rubber (Parts A - pre-polymer, B - polyol, and C - softener, Polytek Development Corp., Easton, PA, USA) at a 1:1:1 mixing ratio resulting in similar acoustic properties (sound speed c_p = 1410 m/s, density ρ_p = 1090 kg/m^3) to those of soft biological tissues.

A plastic 3D printed mold and a precisely positioned 6 mm steel rod were used to imprint a 6 x 70 mm (⦸ x length) tube before the polyurethane rubber was cured overnight [Figure 5.3(a – b)]. Though normal ureter diameters typically range from 3 ~ 4 mm in diameter, 6 mm ureter model was selected for this study to mimic the stone-induced ureter dilation (caused by inflammation and ureteral mucosal edema with an average diameter of 5.3 and 6.1 mm for the distal and proximal ends, respectively), observed in previous studies [70]. Using X-ray computer tomography, ureteral stones measured 5.0 ~ 5.3 mm in the axial plane and 8.3 ~ 9.9 mm in the coronal plane for distal and proximal locations, respectively, have been reported [ref]. Using the 6-mm ureter model, the same cylindrical stone phantoms, (7 x 7 mm, D x H) described in section 4.2,

which fall into the size range between non-passable (> 5 mm) and upper limit of urinary stones treated by SWL (> 10 mm), could be used. The polyurethane ureter model was secured in a 3D printed supportive housing unit [Figure 5.3(c – d)] that is connected to the translational stage described in section 4.2. Individual stones were centered in the ureter model and aligned to the lithotripter focus before SWL [Figure 5.4(d)].

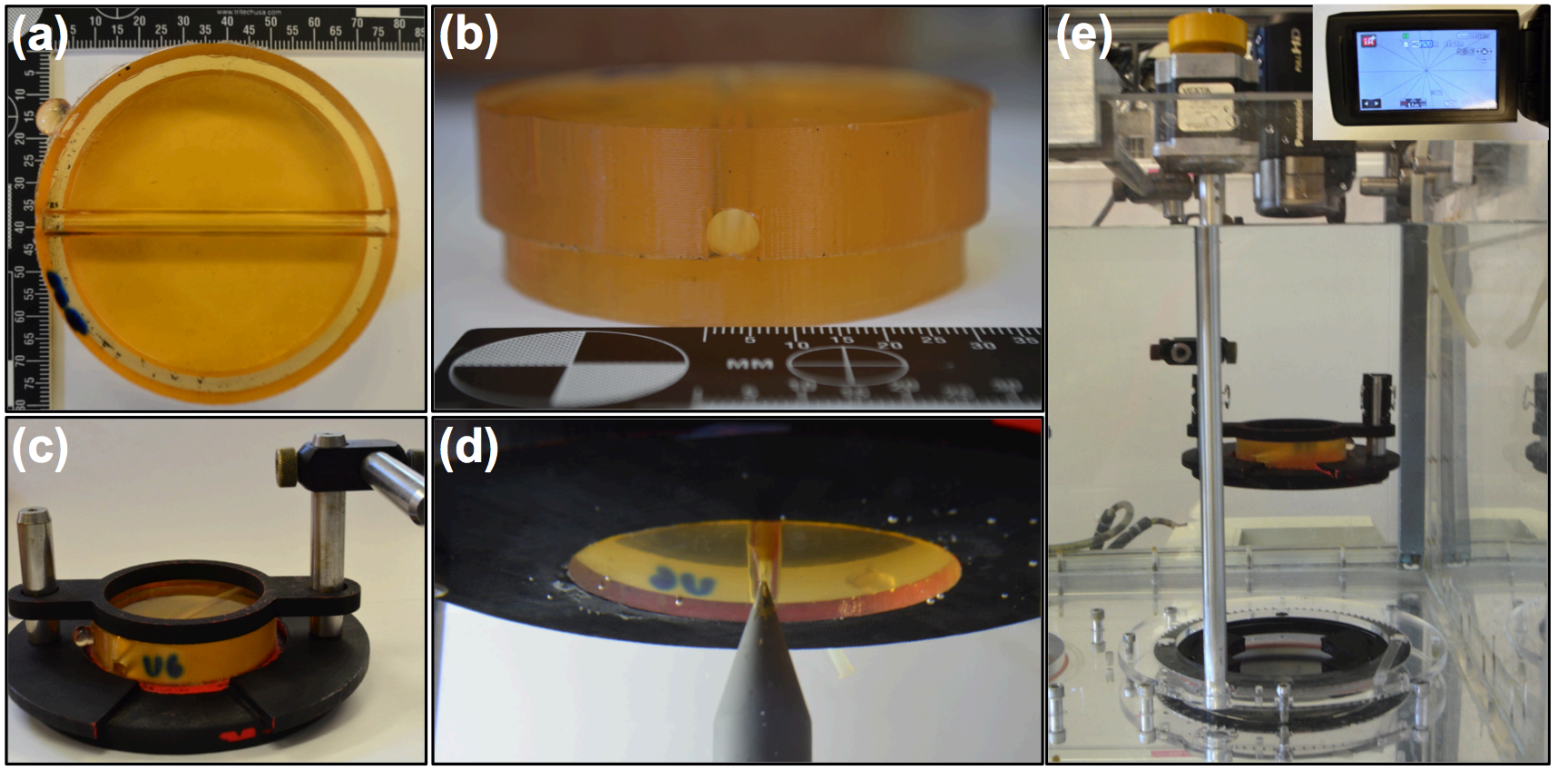

Figure 5.3: (a) Top and (b) side view of the ureter model (6 x 70 mm, ⦸ x length) made of polyurethane rubber. (c) A plastic housing unit connected to a 3D motor controlled stage to position the ureter at the lithotripter focus aided with (d) a mechanical pointer. (e) Digital camcorder positioned above the ureter model to record the stone fragmentation process.

5.2.3 Stone comminution evaluation

5.2.3.1 Static stone comminution in a ureter model

Stone comminution in the ureter model was evaluated with the axisymmetric acoustic field generated by L_1 and non-axisymmetric acoustic fields produced by L_2+M_{8025} and L_2+M_{9030}, at lithotripter charging voltages of 14 kV, 15.8 kV, and 17 kV, respectively. Masks were aligned along the *y*-axis, as described for all previous stone comminution experiments in Chapter 4. The length of the ureter phantom was aligned to either the *x*-axis, perpendicular to the mask alignment ($ureter_x$) or the *y*-axis ($ureter_y$). Stones were treated with 1000 shocks administered at 1 shock per second. Visualization of the stone fragmentation process was captured using a digital camcorder (Panasonic HC-V720 HD, Osaka, Japan) positioned ~16 cm above the ureter and secured to the water tank wall [Figure 5.3(e)].

After treatment, fragments were dried and then segmented by sieves (No. 5, 7 and 10, W.S. Tyler, Mentor, OH) to determine the size of fragment (D_f) in the range of $D_f <$ 2.0 mm (considered passable by patients), 2.0 < D_f < 2.8 mm, 2.8 < D_f < 4 mm and $D_f >$ 4 mm. To quantify stone comminution, the percent of fragments in each size range normalized by the original stone mass were quantified. Statistical analysis was performed as described in section 4.2.

5.2.3.2 Stone comminution in the ureter model at a slanted angle under simulated respiratory motion

The second set of stone comminution experiments examined the effects of ureter anatomy combined with the influence of respiratory motion. This particular experiment focused on evaluating the performance of the non-axisymmetric steerable acoustic field. To more closely match the anatomical variation observed *in vivo,* the ureter phantom was positioned at an angle (Φ), measured between the length of the ureter section where the stone resides and the respiration axis (*y*-axis). Two particular angles of interest were selected for investigation: 1) $\Phi_1 = 40°$ to mimic the funnel-like shape of the ureter angled from the renal pelvis (ureteropelvic junction) and 2) $\Phi_2 = 10°$ to represent the mid-ureter section that aligns fairly close with the respiration axis [Figure 5.4].

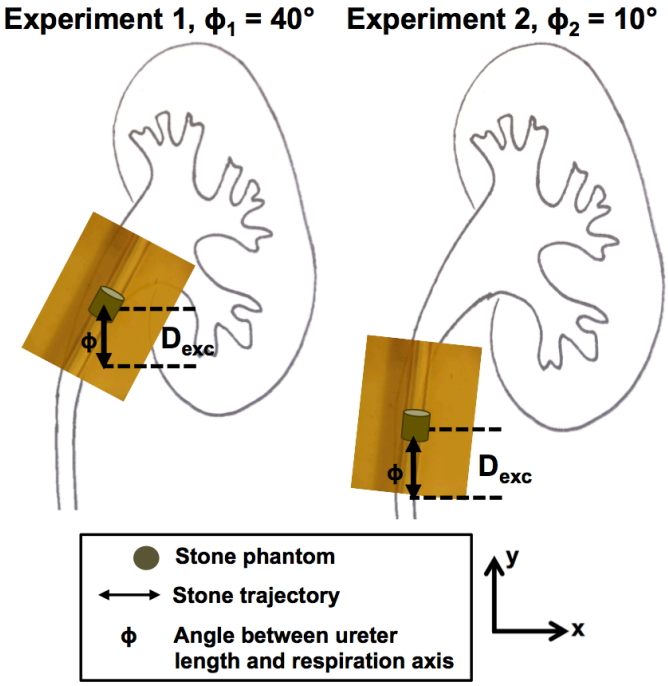

Figure 5.4: Schematic representation of the angled ureter model with simulated respiratory motion. Ureters were oriented at an angle of Φ, measured between the ureter axis and the respiration axis. Two representative angles were investigated: $\Phi_1 = 40°$ and $\Phi_2 = 10°$, and the respiration was set at an excursion distance of 10 mm with 12 breaths per minute.

The respiratory model described in section 4.2.2 was used to translate the ureter phantom. A reduced excursion distance of D_{exc} = 10 mm was selected because previous studies have shown that ureteral stones are less affected by patient's respiration [47]. The ureters at the lower end are generally fixed but stones located in the ureteropelvic junction to the level of the inferior pole have displacement patterns similar to that in the kidneys [116, 117]. Cheng et al showed that under endotracheal general anesthesia proximal ureteral stones translate ~6.5 mm and under intravenous fentanyl anesthesia stones translate ~10 mm; hence, we selected an excursion distance of 10 mm [47]. It is important to note that respiratory movements of the kidneys may produce ureteric kinks

or angulations at the proximal end; however, exploring such factors is beyond the scope of this study [116]. The distal end of the ureter has minimal observed movement since it is located in the pelvic region unaffected by respiration so we consider that the static ureter stone comminution described in 5.2.3.1 would be appropriate for such conditions [118].

After individual stone phantoms were positioned at the center of the ureter and aligned to the lithotripter focus, the non-axisymmetric acoustic field was rotated by Φ to align the elongated beam with the ureter axis. Stones were treated with 1000 shocks administered at 1 Hz PRF using either the axisymmetric or non-axisymmetric fields without rotation. Subsequent data quantification and statistical analysis were performed as described in section 5.2.3.1.

5.2.4 Acoustic field steering to enhance the total dose of administered average peak pressure during stone treatment

The final experimental evaluation in this chapter included comparing stone comminution in the ureter model during respiratory motion. Specifically, a protocol to steer the non-axisymmetric acoustic field during treatment was designed by enhancing the total dose of the average peak pressure administered to the stone and residual fragments in the translating ureter model. The parameters that were incorporated into the design of the treatment protocol include pressure distribution in the acoustic field (Chapter 3), ureter positions throughout the respiration cycle (described in Chapter 4),

and the spreading characteristics of stone fragments during treatment in the ureter model (section 5.2.2).

5.3 Results

5.3.1 Static stone comminution in a ureter model

To investigate stone comminution in an anatomical structure that has directional bias on spreading, stones were first treated in the ureter model without translation from respiratory motion. In general, stones were observed to be fragmented either into small pieces deemed passable (< 2 mm) near the lithotripter focus or pushed away significantly off-axis and remained large size (> 4 mm) throughout the entire treatment [Figure 5.5]. This was especially true for stones treated with L_1 [Figure 5.5(a)] and when the ureter model was aligned to the *x*-axis of L_2+M_{8025} and L_2+M_{9030} (images not shown). *SC* is statistically the same for these three groups ($p > 0.1$), supported by similar values in the $p_{+(avg)}$ (18.7, 18.5 and 17.8 MPa for L_1, L_2+M_{8025} and L_2+M_{9030}, respectively) within a 6 x 20 mm (width x length) area centered around the lithotripter focus. Under these treatment conditions, large sized fragments were displaced by 22.5 ± 5.8 mm threshold from the focus after the initial 100 shocks, and thereafter minimal movement of the residual large fragments were observed up to 1000 shocks, based on analysis of the captured movies in ImageJ (National Institute of Health, Bethesda, Maryland). In contrast, when the ureter model was aligned with the *y*-axis of L_2+M_{8025} and L_2+M_{9030}, the stone was fragmented gradually in the first 100 shocks with minimal off-axis displacement of the large fragments as shown in Figure 5.5(b) and 5.5(c), respectively.

Under these conditions with better alignment with the elongated beam direction, higher $p_{+(avg)}$ of 20.2 and 21.8 MPa for L_2+M_{8025} and L_2+M_{9030}, respectively, were delivered to the ureter model, leading to better SC after 1,000 shocks.

Quantitatively, the lowest SC in the range of 24.0 ~ 27.3% was produced by L_1 or L_2+M_{8025} and L_2+M_{9030} when the ureter axis was aligned perpendicular to the elongated beam direction (Figure 5.6). In contrast, when the ureter was aligned to the elongated beam (*y*-axis) of the L_2+M_{8025} and L_2+M_{9030} SC was more than doubled (51.2 and 57.0% for L_2+M_{8025} (red) and L_2+M_{9030} (blue), respectively). The difference is statistically significant with L_2+M_{9030} producing higher *SC* than L_2+M_{8025}, both of which are also higher than their counterparts in the x-axis and those produced by L_1.

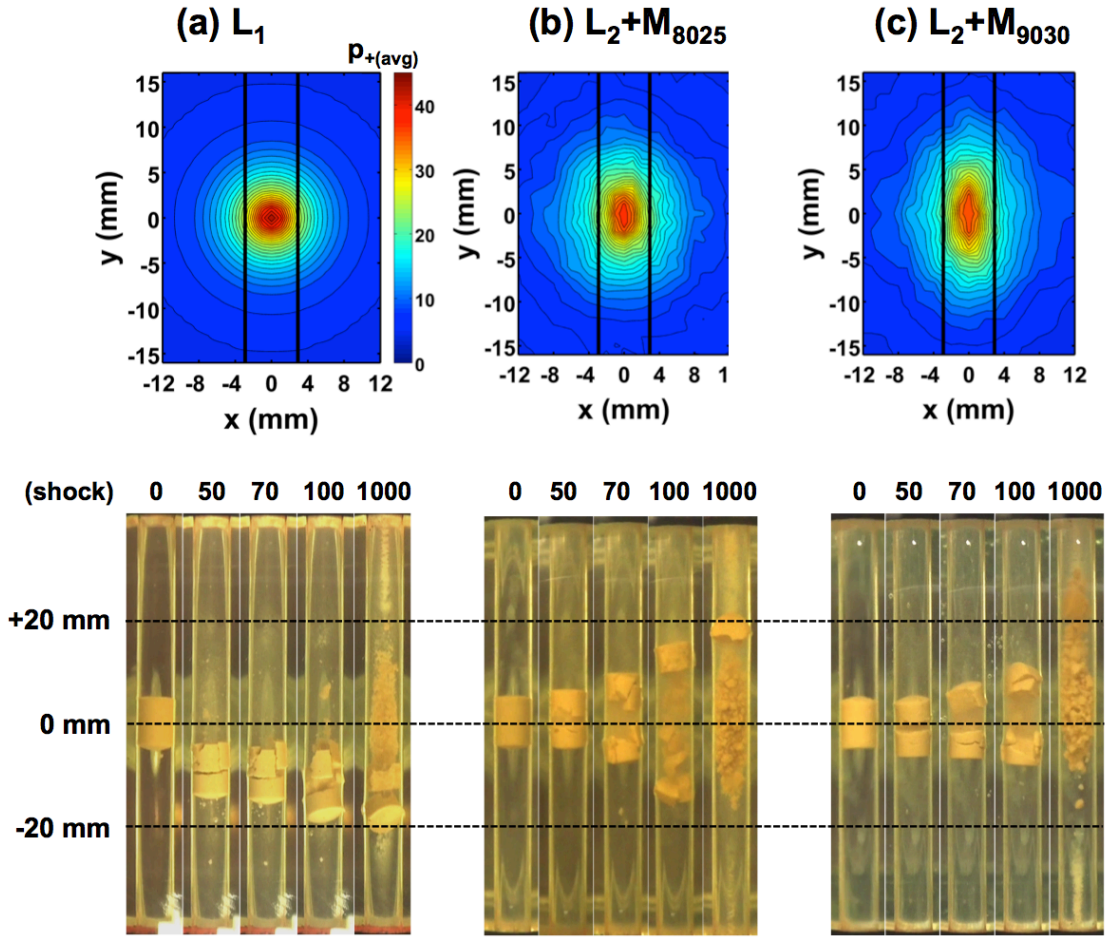

Figure 5.5: Contour plots of peak pressure in the focal plane with ureter geometry outlined in black and representative video camcorder images of stone comminution processes in the ureter model aligned to the *y*-axis with (a) L_1, (b) L_2+M_{8025} and (c) L_2+M_{9030}. Captured images are shown for 0, 50, 70, 100 and 1000 shocks. The ureter channel is 6 x 70 mm (⦸ x length) and the cylindrical stone phantoms are 7 x 7 mm (⦸ x H).

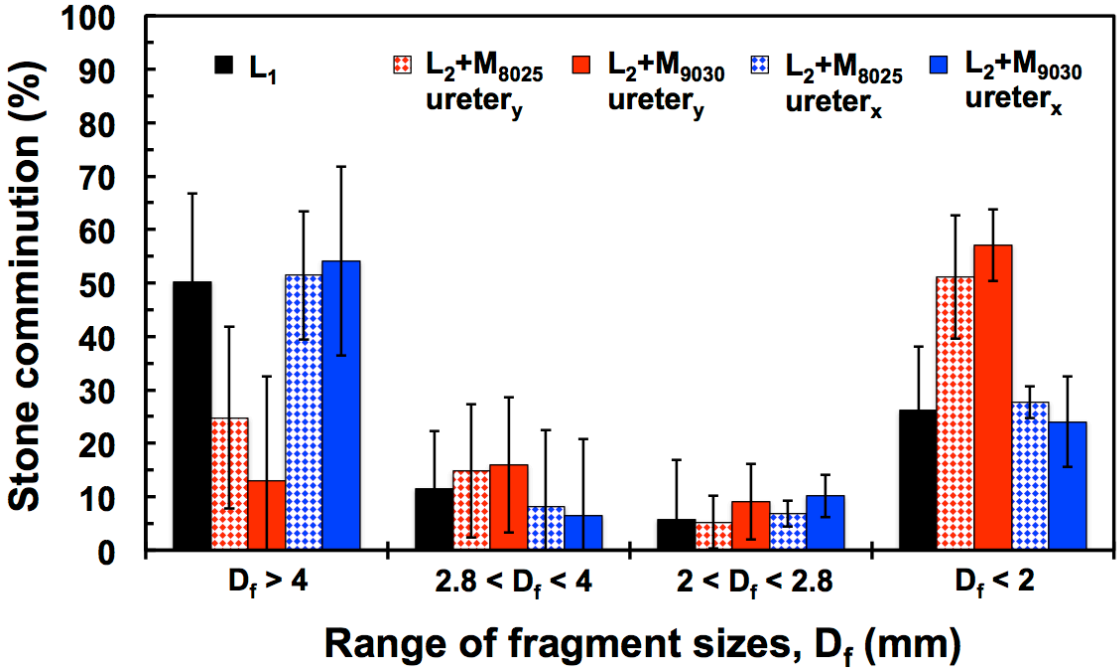

Figure 5.6: Percent of stone comminution (n = 10) in the ureter model in different range of fragment sizes produced under static treatment condition by 1000 shocks delivered at 1 Hz PRF. The ureter model was aligned to either the *x*-axis ($ureter_x$, checkered) or *y*-axis ($ureter_y$, solid) of L_1 (black), L_2+M_{8025} (red), and L_2+M_{9030} (blue).

5.3.2 Stone comminution in an angled ureter model during simulated respiration motion

Since L_2+M_{9030} produced better *SC* than L_2+M_{8025} when the ureter is aligned to the elongated beam direction, its performance was further examined in a setup that combined anatomical geometry and respiratory motion. Figure 5.7 shows *SC* produced after 1000 shocks in the ureter model aligned at Φ of 10° (a) and 40° (b) while translated during simulated respiratory motion for L_1 (black) and L_2+M_{9030} (blue), also aligned to Φ throughout treatment. Though not statistically significant, comminution efficiency (*SC* < 2 mm) produced by both lenses is lower when the ureter is oriented at 40° as compared to

10° angle from the respiration direction. This result suggests that the geometric relation between the ureter and the respiration axis may affect the treatment efficacy. In comparison, L_2+M_{9030} produces a better comminution than L_1 at 10° (39.4% vs. 28.0%) and 40° (33.3% vs. 18.2%, respectively ($p = 0.03$),

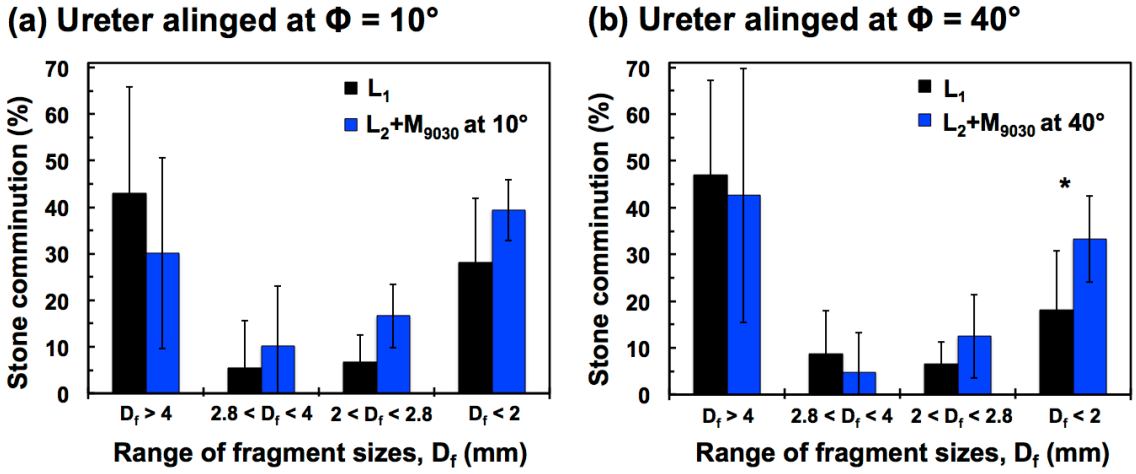

Figure 5.7: Stone comminution (n = 6) in the ureter model, which was translated during simulated respiratory motion (along the *y*-axis, 0°) with an excursion distance D_{exc} = 10 mm and at 12 breaths per minute. The ureter was oriented at Φ of (a) 10° and (b) 40°. Results are shown for L_1 (black) and L_2+M_{9030} (blue) that was aligned at Φ with the ureter axis. Stones were treated with 1000 shocks at 1 Hz PRF.

5.3.3 Treatment strategy based on stone comminution, field parameters and stone spreading results

Treatment strategy based on stone comminution, field parameters and stone spreading results

To develop the steering protocol, several factors were considered. The trajectory of the stone and fragments throughout respiration cycle [Figure 5.8(a)] was analyzed to enhance the total dose of $p_{+(avg)}$ delivered to the ureter model. L_1 produces an axisymmetric field, thus has no capability to steer (or rotate). In contrast, because of its

non-axisymmetric field L_2+M_{9030} is capable of steering to better match with the stone trajectory. Figure 5.8 shows calculated $p_{+(avg)}$ for L_1 (c), L_2+M_{9030} (d) and L_2+M_{9030} with steering incorporated (e). The steering protocol includes rotating the mask with the ureter motion path from Φ (aligned to the ureter) to 0° (aligned to *y*-axis) at the same speed of the respiratory motion to maximize $p_{+(avg)}$ delivered. By steering the mask instead of maintaining alignment with the ureter, $p_{+(avg)}$ increases from 14.0 to 14.4 MPa (Φ = 10°) and from 9.6 to 11.5 MPa (Φ = 40°) at D_{exc} of 10 mm. Compared to L_1, the steering protocol of L_2+M_{9030} increases $p_{+(avg)}$ from 18.7 to 21.8 MPa at the focus and from 11.2 to 14.4 MPa (Φ = 10°) and 9.9 and 11.5 MPa (Φ = 40°).

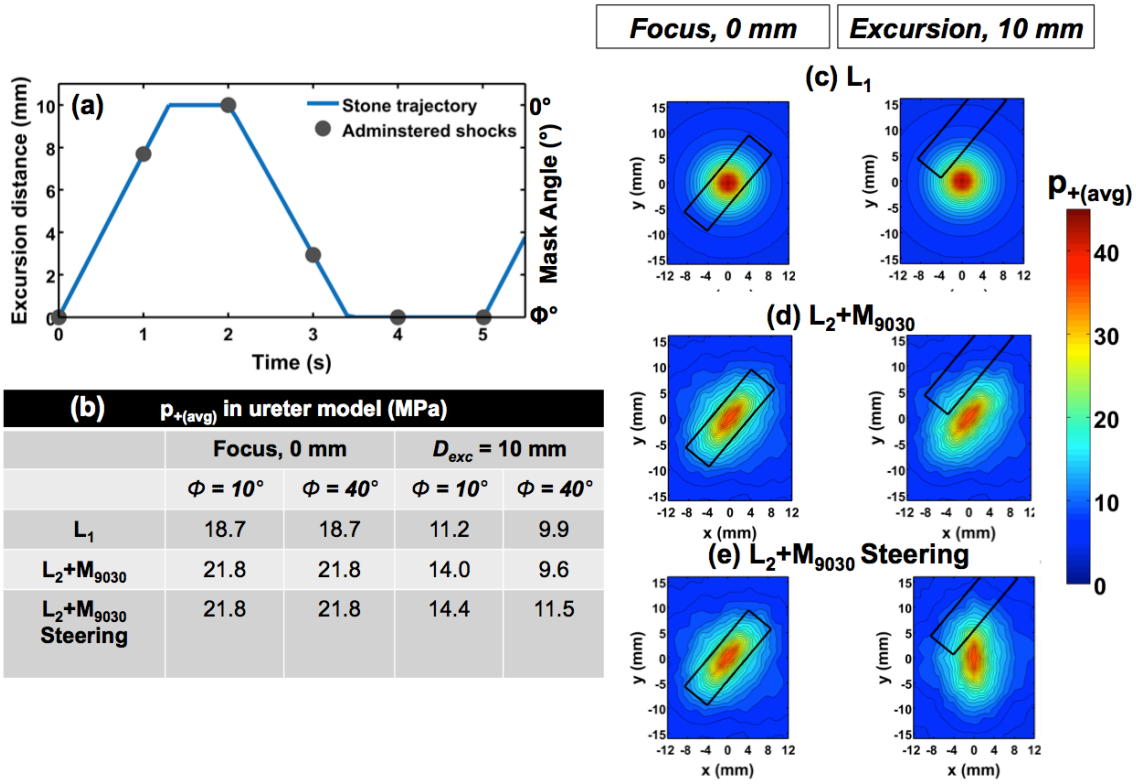

(b) $p_{+(avg)}$ **in ureter model (MPa)**

	Focus, 0 mm		D_{exc} = 10 mm	
	Φ = 10°	Φ = 40°	Φ = 10°	Φ = 40°
L_1	18.7	18.7	11.2	9.9
L_2+M_{9030}	21.8	21.8	14.0	9.6
L_2+M_{9030} Steering	21.8	21.8	14.4	11.5

Figure 5.8: (a) Respiration cycle showing the stone trajectory and rotation of L_2+M_{9030} for steering. (b) Calculated $p_{+(avg)}$ generated by L_1, L_2+M_{9030} and L_2+M_{9030} with steering. (c – e) Peak pressure in the focal plane showing the orientation of each acoustic field generated by (c) L_1, (d) L_2+M_{9030} and (e) L_2+M_{9030} with steering at both the focus and at maximum excursion distance (D_{exc}) of 10 mm.

5.3.4 Stone comminution with idealized treatment strategy

Stone comminution with an improved treatment strategy

Figure 5.9 shows the enhancement of *SC* produced by steering of L_2+M_{9030} in addition to simply aligning the elongated beam axis to the ureter. Though the increment has not achieved statistical significance, the upward trend is clear at both angles investigated. Compared to L_1 (18.2%), comminution efficiency is statistically enhanced by steering L_2+M_{9030} (38.0%) at $\Phi = 40°$ ($p = 0.009$).

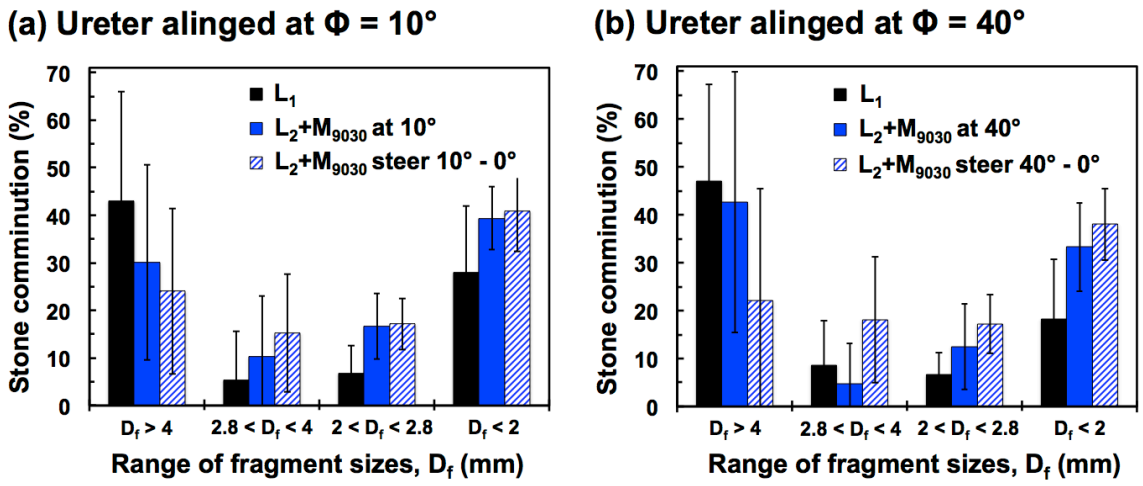

Figure 5.9: Averaged (n = 6) stone comminution in the ureter model translated during simulated respiratory motion (along *y* –axis, 0°) with an excursion distance of D_{exc} = 10 mm and 12 breaths per minute. The ureter was angled at Φ of (a) 10° and (b) 40°. Results are shown for L_1 (black) and L_2+M_{9030} (blue) angled at Φ and while steering L_2+M_{9030} (blue, checkered) rotating between Φ and 0° thus maximizing administered average peak pressure to the fragments in the ureter. Stones were treated with 1000 shocks at 1 Hz.

5.4 Discussion

In this chapter, a ureter model was designed to evaluate stone comminution produced by an axisymmetric versus a steerable non-axisymmetric acoustic field. To effectively steer the non-axisymmetric acoustic field on command, a motor controlled gear system was incorporated into the mask designs previously described in Chapter 2. Static results demonstrate that both L_2+M_{8025} and L_2+M_{9030} can enhance stone comminution to more than 2-fold when the ureter is aligned to the elongated beam direction, as compared to L_1. With higher $p_{+(avg)}$ delivered to the ureter (aligned to the *y*-axis) L_2+M_{9030} generates better comminution efficiency than L_2+M_{8025}. Furthermore, in contrast to the commonly observed Gaussian-like distribution of fragment sizes in a tube holder, fragments produced in the ureter model split into two distinct groups: one small

and passable group (< 2 mm) and another of large fragments (> 4 mm). These results demonstrate the critical influence of anatomical structures on stone spreading and ultimately treatment efficacy. Stones treated in the static ureter model may translate well to clinical treatment of stones along the ureter with minimal respiratory motion (mid- to distal ureter). If the clinical lithotripter field could be transformed to effectively cover the irregular elongated geometry of a ureter, treatment outcome may be enhanced.

By combining anatomical structure and stone translation during respiratory motion in an *in vitro* experiment, it was shown that the steerable non-axisymmetric acoustic field statistically enhances stone comminution by following the trajectory of the stone to enhance the total dose of $p_{+(avg)}$ during the entire treatment. Specifically, this result was most prevalent at ureter alignments angled at 40° showing an increase of stone comminution from 18.2% to 38.0% demonstrating the capability of the non-axisymmetric steerable beam to adapt to ureter angle and respiratory motion effectively. Further optimization of the steering protocol is needed to deliver the highest possible average peak pressure to the stone, accounting for both anatomical structure and stone translation caused by respiratory motion during SWL. In particular, we foresee that initially aligning the stone off set from the focus opposite the direction of respiratory motion could further improve *SC* efficacy, as the generated acoustic field will cover a greater coverage area of the stone trajectory.

It is postulated that the steerable non-axisymmetric acoustic field designed in this study has two primary advantages relevant to clinical SWL. First, even without distinct

respiratory motion, the acoustic field distribution could be initially aligned to the irregular shapes of the kidney (renal pelvis or calyces) or ureter. Controllability and flexibility of the acoustic field is critical as anatomical structures vary drastically between even healthy patients so a permanent field is not beneficial. Second, designing treatment strategies for steering the non-asymmetric field may enhance treatment outcome by accounting for contributions of stone translation during respiratory motion and stone spreading influenced by the immediate surrounding anatomy.

6. Summary

The main goal of this dissertation is to design, implement and evaluate an acoustic field transformation that provides a better match of the acoustic pressure field and effective pulse energy with the target stone and resultant fragments in the irregular anatomical structure of the upper urinary system during SWL, in particular under the influence of respiratory motion. Multiple factors were considered when designing the acoustic field transformation from a conventional axisymmetric field along the lithotripter axis to an elongated and non-axisymmetric one, especially in the lithotripter focal plane. The three most critical factors are: 1) limitation in broadening the acoustic field while keeping the incident pressure at the skin surface to be low enough (e.g., < 20 MPa at 60 mm distance from the lithotripter focus) to minimize patient discomfort, 2) maintaining the capability to fragment hard stones with reduced peak pressures [38], and 3) minimizing the risk of tissue injury, commonly related to the peak energy flux density of the LSW and cumulative energy delivered to the focal region [16, 57, 58].

Chapter 2 describes the design concept and criteria of an external acoustic barrier (mask) to transform the acoustic field. A linear wave propagation model was used to guide the selection of the mask geometry in terms of two main parameters: 1) the fanning angle β and 2) the radius change ΔR. By blocking a portion of the incident wave originated from the EM coil along the y-axis, the beam width of the lithotripter field along this particular direction can be a broadened. Based on the model calculation of the ratios of beam width elongation and peak pressure reduction two mask geometries were

selected for implementation and performance evaluation. Because the mask covers a portion of the incident wave energy, the charging voltage of the EM shockwave source has to be increased in order to deliver comparable effective acoustic pulse energy to the lithotripter focal zone. However, higher charging voltage causes a pre-focal shift of the LSW peak pressure. To correct this, a modified lens (L_2) with a larger radius of curvature than the original lens (L_1) was used to better align the LSW peak pressure with the lithotripter focus. Altogether, two modified lenses with masks (L_2+M_{8025} with moderate beam elongation and L_2+M_{9030} with maximum beam elongation) were selected for implementation and comparison against the original lens (L_1) with axisymmetric pressure field used in clinical EM shock wave lithotripters.

Acoustic field characterization in Chapter 3 reveals that the pressure distribution in the focal plane and subsequent bubble activity in the focal zone generated by both masks transformed from a narrow beam width and high pressure axisymmetric field to a non-axisymmetric lower pressure distribution broadened along the axis of mask alignment. Acoustic field characterization helped to identify lithotripter charging voltages for each setup that yield equivalent acoustic energy delivered to the focal region within a 12 mm circular area. At these settings, the broad pressure *y*-axis of L_2+M_{8025} and L_2+M_{9030} enhances the beam width from ~7.5 mm to 11.4 and 14.3 mm, respectively, as compared to the axisymmetric beam width. In addition, the pulse intensity integral (energy flux density) delivered to the focus was reduced from 0.62 mJ/mm^2 (L_1) to 0.57 (L_2+M_{8025}) and 0.53 (L_2+M_{9030}) thus implicating lower risk of tissue injury [57].

An initial stone comminution (*SC*) evaluation included treating hard BegoStone stone phantoms at the lithotripter focus and at several off-axis field positions along the *x*-axis and *y*-axis with each setup (Chapter 4). Compared to L_1, L_2+M_{8025} performed more effectively at positions $0 < y_h < 8$ mm while L_2+M_{8025} demonstrated improvements at $y_h >$ 8 mm thus agreeing with the acoustic fields measured. Importantly, there was no statistical difference between *SC* along the narrow pressure distribution of both masks compared to L_1 at all field positions. The results of acoustic field characterization of each setup were evaluated against stone comminution of stones Correlations of *SC* and average peak pressure delivered to a BegoStone phantom stone inside a tube holder show that an approximately equivalent pressure threshold of ~10 MPa was observed for all setups, agreeing with previously observed convergence pressure thresholds of fragmentation [38]. The effective area of stone comminution (A_{eff}) for each setup was extrapolated from the acoustic field measurements by determining the position along the *x*-axis and *y*-axis yielding the average peak pressure threshold. Both masks enhance A_{eff} by more than 40% compared to L_1 by broadening the pressure distribution along the *y*-axis.

Non-axisymmetric pressure distributions were further evaluated by treating translating stones in the tube holder during simulated respiratory motion, with and without clinically relevant initial stone misalignment (Chapter 4). Stones ideally aligned to the lithotripter focus and translated along the broad pressure distribution of L_2+M_{8025} and L_2+M_{9030} fragment more effectively (*SC* ~ 70%) compared to L_1 (*SC* ~ 60%). Alignment sensitivity results reveal that *SC* is reduced as initial alignment moves further

from the focus, perpendicular to the respiration axis; however, if positioned opposite the direction of the respiration direction, *SC* is enhanced. Overall, L_2+M_{8025} (mask investigated in this set of experiments) demonstrates less sensitivity at alignment positions beyond 2 mm from the focus than L_1. Lastly, L_2+M_{8025} produces higher *SC* at all misalignment positions compared to L_1.

Chapter 5 aimed at bridging *in vitro* experimental analysis to clinical challenges. A ureter model was designed to evaluate steerable non-axisymmetric acoustic fields generated by L_2+M_{8025} and L_2+M_{9030}. The non-axisymmetric acoustic field when aligned to the ureter enhances stone comminution. It was shown that by incorporating a steerable gear system, the non-axisymmetric field is feasibly aligned to stone trajectory during respiratory motion and to the ureter thus creating a controllable system to optimize average peak pressure delivered to stone fragments. Finally, the results in this dissertation motivate future work specifically focusing on continued *in vitro* stone comminution evaluation of the steerable non-axisymmetric acoustic field, further optimization of both mask geometry and steerable acoustic field protocol and translation to a clinical lithotripter setup.

7. Recommendation for future work

The work completed in this dissertation demonstrates an enhancement of *in vitro* stone comminution during simulated respiratory motion and in a ureter model with a non-axisymmetric steerable acoustic field as compared to an axisymmetric lithotripter acoustic field. The first area of proposed future work includes examining the performance of the steerable non-axisymmetric field in other relevant conditions that motivate a controllable elongated pressure distribution. Specific experimental designs may include lower pole stones under significant respiratory motion and stones in locations like the renal pelvis with maximum likelihood of spreading. Alongside designing experimental designs mimicking *in vivo* conditions (anatomy and respiration), it will be beneficial to continue to investigate treatment strategies for effective steering (i.e. Pre-positioning of stone opposing respiration trajectory).

Though two mask designs were characterized and evaluated in this dissertation, the optimization and assessment of mask geometry has yet to be completed. The linear approximations utilized for mask geometry selection should be expanded to a more rigorous numerical simulation incorporating the nonlinearity of the shock wave propagation. A three dimensional numerical model that captures the pressure field distribution in the focal zone would enable a more effective method for investigating mask geometries as compared to the time extensive process of experimental acoustic field characterization. Collaborators at the University of North Carolina, Chapel Hill are currently expanding and validating a previously developed numerical model for

geometric mask optimization. From the results in this dissertation, it is not likely that a specific optimal geometry will suffice as the variations of anatomical structures and stone locations observed in clinic motivate a flexible field design. Therefore, the focus of the optimization process is two-fold: 1) optimize mask geometries specific to several key locations and critical factors influencing stone comminution (respiratory motion excursion distance, misalignment and stone spreading) and subsequently 2) select mask geometries for acoustic field transformations that operate at a minimum charging voltage (< 17 kV). Criteria for optimizing mask geometries dependent on stone location and influencing factors like stone spreading and respiratory motion would include maximizing the average peak pressure and cavitation within the vicinity of the stone trajectory while simultaneously minimizing the risk for tissue injury.

Lastly, translating from the *in vitro* experimental design extensively described in this work to a clinical lithotripter exposes several key challenges. The dry coupling utilized in clinic as compared to the wet coupling (water tank) used in this work would limit the available space about the acoustic lens for incorporating an external mask attachment. Furthermore, the computer-controlled program to rotate the mask has yet to be coupled with the imaging system currently used in modern lithotripters making the alignment of the pressure distribution to anatomical structures and stone trajectory not yet possible. A mask or acoustic barrier above the coil, instead of the acoustic lens, may be more practical for implementation in lithotripters in clinic. Also, an inflatable air pocket design to both steer the acoustic field and adjust beam width elongation depending on the

target stone's location (ureter or calyces) and even modify the field during treatment would be the optimal clinical design. Alongside optimization of mask geometry and translation of the design to clinical lithotripters, *in vivo* animal studies should be designed to evaluate a non-axisymmetric acoustic field in more clinically relevant environments.

Appendix A

To ensure that the acoustic lens L_2 did not enhance the non-axisymmetric acoustic field produced by implemented masks, the pressure field measurements and stone comminution generated by L_1 and L_2 (without masks) were compared. This section details the acoustic field characterization (methods described in 3.2.1.1) results of axisymmetric EM lithotripter setups L_1 and L_2 (without acoustic masks) at matched acoustic energy E_{eff} within a 12 mm circular area. The operating voltage of the EM Lithotripter was 14 kV for L_1 and 14.6 kV for L_2. Figure A.1 shows averaged peak pressure (p_+) as a function of field position (x-axis, open markers and y-axis, filled markers) for L_1 (triangles) and L_2 (diamonds). Both setups produce an axisymmetric p_+ distribution with L_1 delivering a minimally greater p_+ to the focus (44.1 MPa) compared to L_2 (42.2 MPa). The p_+ distributions of L_1 and L_2 are approximately equivalent with BW measurements of 7.5 and 7.7 mm, respectively.

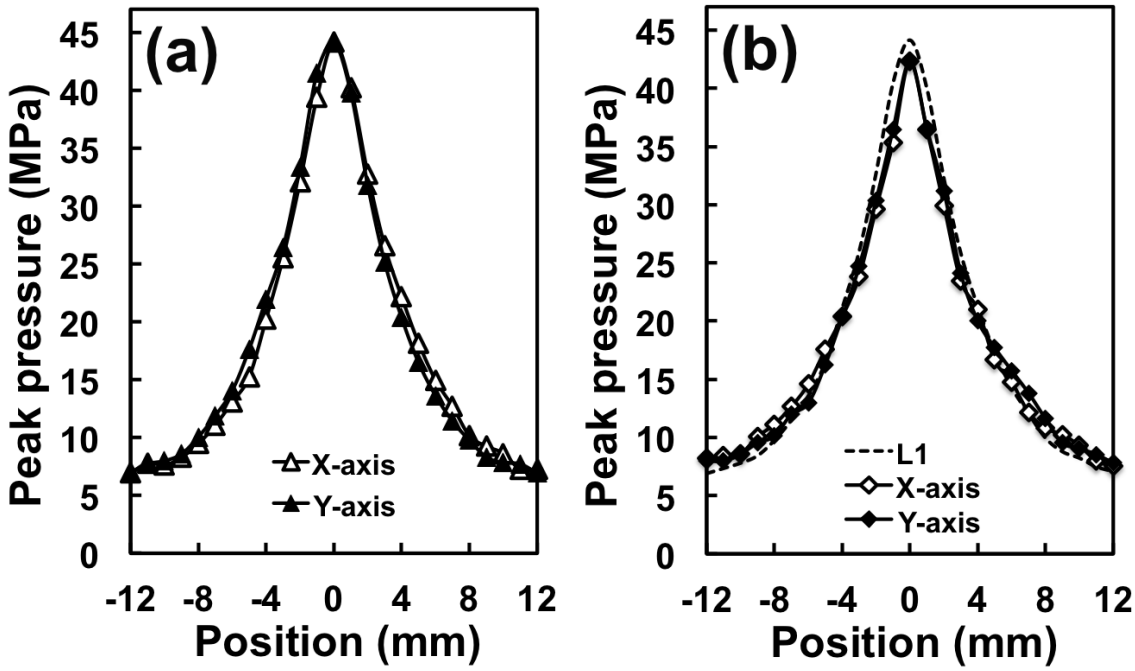

Figure A.1: Acoustic field comparison in the focal plane of (a) L_1 (triangles) and (b) L_2 (diamonds). Averaged peak pressure (p_+) at z = 0 mm measured along the x-axis (filled) and y-axis (open); dashed line in (b) corresponds to the average of p_+ measured along the x-axis and y-axis of L_1.

Figure A.2 shows p_+ along the z-axis for L_1 and L_2. Results demonstrate the post-focal shift of the LSW peak pressure as compared to the lithotripter focus (z = 0 mm) with L_2. By increasing the operating voltage of the lithotripter, there is an observed shift of the LSW peak pressure toward the lithotripter focus. In addition, p_+ reduces to 13.8 and 13.0 MPa at z = -60 mm with L_1 and L_2, respectively.

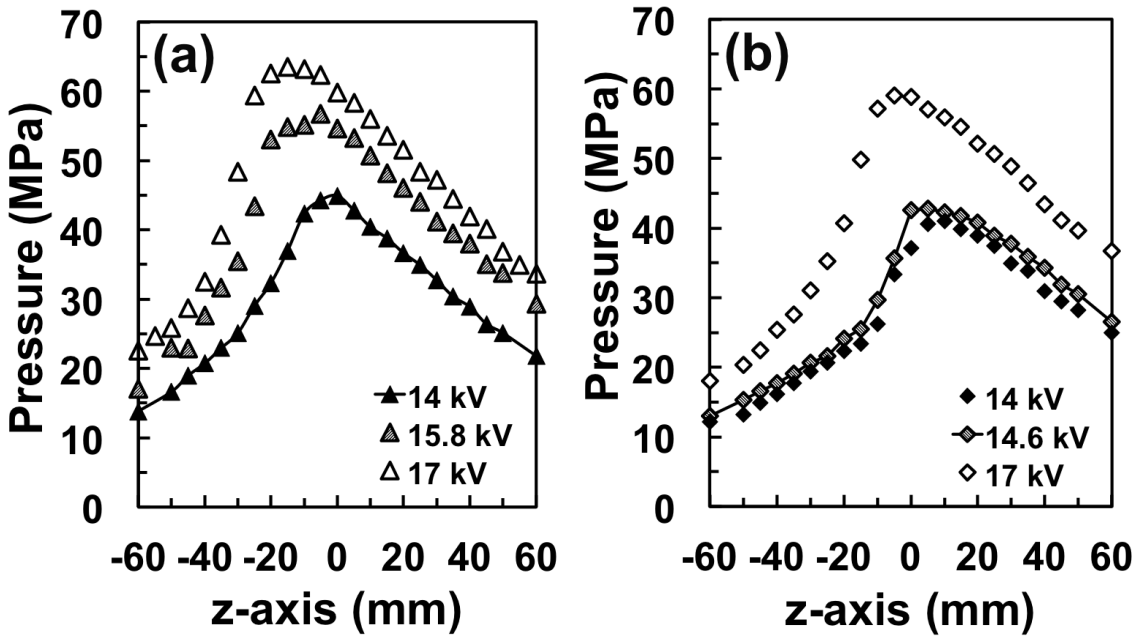

Figure A.2: Averaged p_+ measured along the z-axis of L_1 (a, triangles) and L_2 (b, diamonds) at different source voltages (14 kV – filled, 14.6 – filled, 15.8 – striped and 17 kV – open); solid line corresponds to experimental condition used for stone comminution comparison.

Table A.1 shows the measured acoustic field parameters of L_1 and L_2. Overall, results show that the generated acoustic fields by both setups are approximately equivalent.

Table A.1: Summary of measured acoustic field parameters for L_1 and L_2.

	Source voltage (kV)	p_+ (MPa)	p_- (MPa)	BW_x (mm)	BW_y (mm)	E_{eff} (mJ)
L_1	14	44.1	-10.6	7.5	7.5	44.5
L_2	14.6	42.2	-10.8	7.7	7.7	45.2

Figure A.3 shows static stone comminution (methods described in 4.2.1) produced by L_1 (a, triangles) and L_2 (b, diamonds). At all field positions, there was no statistical difference between stone comminution of the two setups investigated ($p > 0.1$).

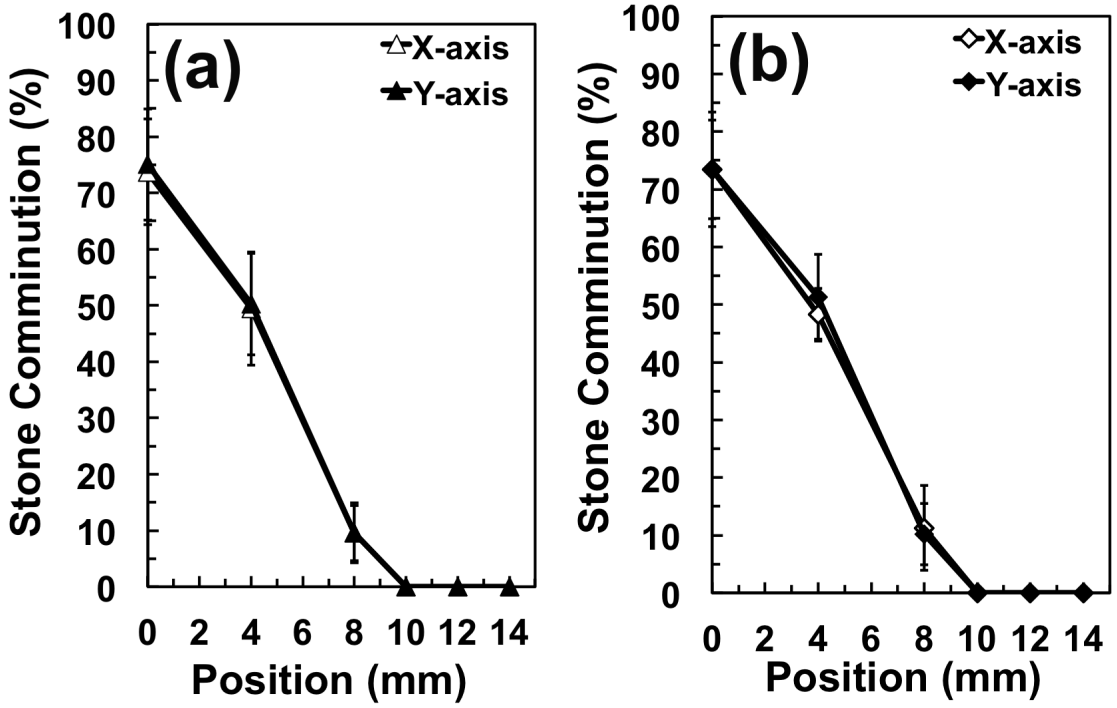

Figure A.3: *In vitro* stone comminution results produced with (a) L_1 and (b) L_2 after 500 shocks treated at the lithotripter focus and at off-axis positions 4, 8, 10, 12, and 14 mm (x-axis, open marker; y-axis, filled marker) with (a); no statistical difference ($p > 0.1$) between L_1 and L_2.

Appendix B

Figure B.1 shows the post-processing of collected pressure waveforms to quantify integral acoustic field parameters $p_{+(avg)}$ and E_{eff}. The peak pressure and the pulse intensity were extrapolated from averaged pressure waveforms. Trinomial fits of acoustic parameters as a function of field position were utilized to integrate over a circular radius of 6 or 7 mm, depending on area of interest. A step size of $\Delta x = \Delta y = 0.1$ mm matched the analytical area of integration with < 2% variation. Because pressure field measurements were collected at 1 mm increments, there is an inherent experimental error associated with the step size utilized collection. Therefore, an error analysis based on the experimental step size is outlined.

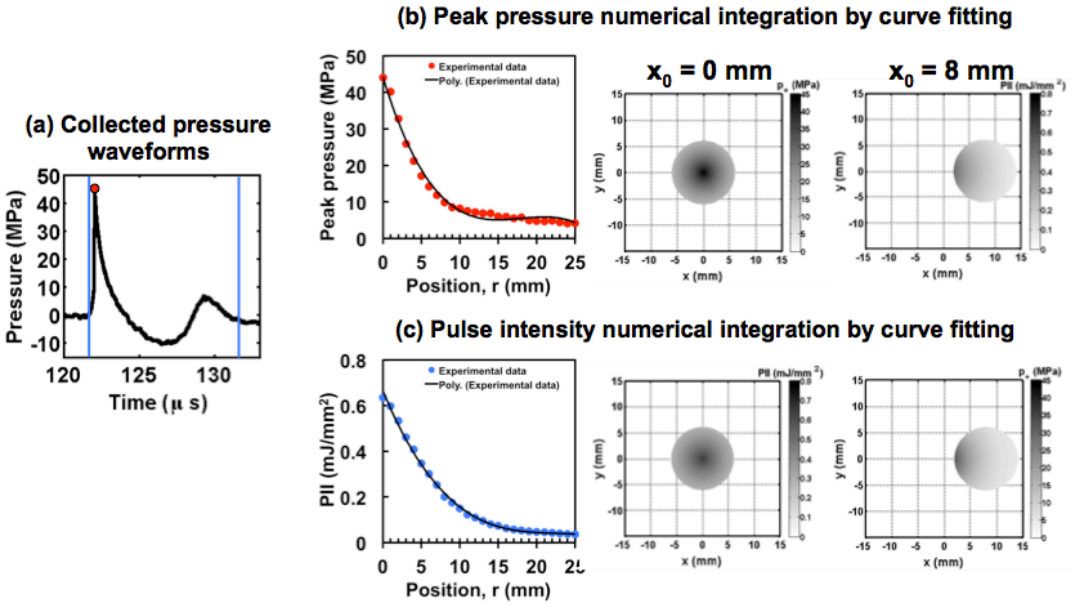

Figure B.1: Post-processing of pressure waveform measurements to calculate integral acoustic field parameters, $p_{+(avg)}$ and E_{eff}, within a circular area (R = 6 or 7 mm). (a) Pressure waveform measurements were averaged and (b) peak pressure and pulse intensity were extrapolated and subsequently fit with trinomial curves for numerical integration as a function of field position.

If the step size between experimental hydrophone measurements approached 0 mm, the numerical integration would approach an exact solution. However, because a step size of 1 mm was used, an experimental error analysis must be examined. By calculating the lower and upper Riemann sum integration, based on a 1 mm step size, the experimental error of $p_{+(avg)}$ and E_{eff} were approximated [Figure B.2].

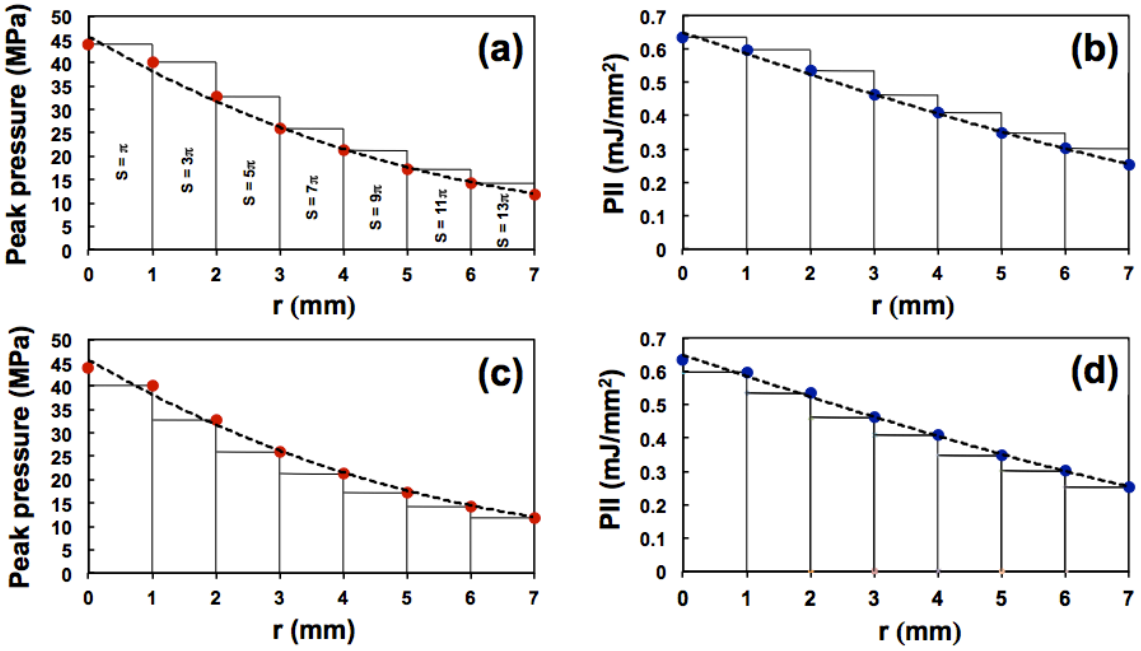

Figure B.2: Experimental error of integrating (a, c) peak pressure and (b, d) pulse intensity within R = 7 mm from pressure waveform measurements collected at 1 mm increments. Error was calculated by calculating (a, b) lower and (c, d) upper Riemann sum integration divided into 1 mm rectangles.

Table B.1 shows results of the lower and upper Riemann sum integration. In addition, the percent difference between the lower and upper bound were calculated. It is assumed that if it were possible, the exact solution would be between the upper and lower limit. Experimental error of $p_{+(avg)}$ and E_{eff} was calculated as ± 9.9% and ± 7.2%,

respectively, compared to a theoretical exact solution. As expected, the trinomial fit results are within the lower and upper Riemann summation suggesting that the method for calculating integral acoustic parameters is reasonable.

Table B.1: Lower and upper Riemann sum integration results of as compared to trinomial fit.

	Lower (MPa)	**Upper (MPa)**	$\frac{Upper-Lower}{Average\ of\ Upper\ and\ Lower} \cdot 100$ **(%)**	**Trinomial (MPa)**
$p_{+(avg)}$	17.8	21.9	19.8	21.0
E_{eff}	53.6	61.9	14.4	55.7

Appendix C

Figure C.1 shows averaged peak pressure (n = 6) measurements along the *z*-axis of L_1 (a, triangles), $L_2 + M_{8025}$ (b, circles) and $L_2 + M_{9030}$ (c, squares) at three operating voltages, 14 kV (filled), 15.8 kV (striped), and 17 kV (open). Continuous lines in each figure correspond to the charging voltages used for acoustic field measurements in the focal plane and stone comminution evaluation. Figure C.1(a) shows the pre-focal shift of the LSW peak pressure with increased charging voltage with L_1. Figure C.1(b) and C.1(c) show an initial post-focal shift of the LSW peak pressure with a charging using L_2 thus demonstrating an effective method to correct for the pre-focal shift of the LSW peak pressure with increased voltage. The operating conditions of $L_2 + M_{8025}$ (15.8 kV) and $L_2 + M_{9030}$ (17 kV) for focal plane measurements (Chapter 3) and stone comminution evaluation (Chapter 4 and 5) still show a minimal LSW post-focal peak pressure shift of 5 mm and 10 mm, respectively.

Peak pressure along the *z*-axis of L_1 shows a sharp decline of pressure from $z = 0$ to -60 mm. At the experimental conditions used for this dissertation, L_1 has minimal pressure of 13.8 MPa at $z = -60$ mm, considered the approximately position along the LSW propagation path of a patient's skin surface. In addition, the -6 dB beam width along the *z*-axis (BW_z) is approximately 90 mm ($-35 \text{ mm} < F < 55 \text{ mm}$). In contrast, $L_2 + M_{8025}$ and $L_2 + M_{9030}$ generate pressure distributions that have peak pressure at $z = -60$ mm of approximately 16.3 and 19.8 MPa, respectively.

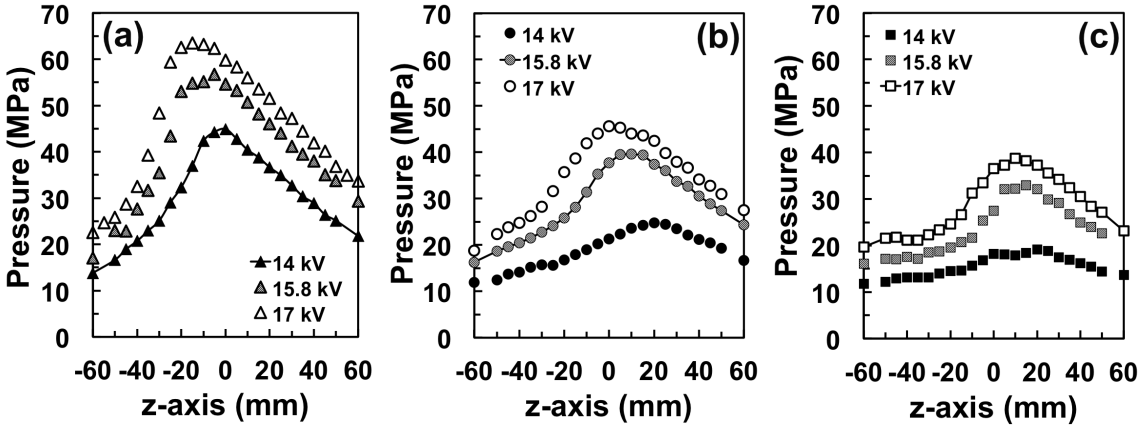

Figure C.1: Averaged peak pressure (p_+) measurements along the z-axis at three different source voltages (14, 15.8 and 17 kV) using (a) L_1, (b) $L_2 + M_{8025}$ and (c) $L_2 + M_{9030}$. Continuous lines represent experimental conditions used for stone comminution with an approximately matched acoustic energy ($E_{eff,\ R=6\ mm} = 45$ mJ) at $z = 0$ mm for the three setups. For all setups, $z = 0$ on the central axis corresponds with the geometric lithotripter focus.

Table C.1: Summary of acoustic field parameters at a variety of source charging voltages.

	Source voltage (kV)	p_+ (MPa)	$\lvert p_- \rvert$ (MPa)	BW_x (mm)	BW_y (mm)	E_{eff} (R=6mm) (mJ)
L_2+L_{5025}	14	26.6	8.6	9.4	11.8	34.9
	15	36.2	8.9	7.9	10.4	43.3
	16	44.8	9.7	7.6	10.1	59.6
L_2+M_{8025}	14	21.3	8.9	8.7	10.3	36.5
	15	35.4	9.2	7.8	10.9	40.6
	15.5	36.2	10.1	7.6	11.3	42.1
	15.8	38.2	10.4	7.6	11.4	44.9
	16	39.9	10.5	7.5	11.3	48.2
	17	45.6	11.0	7.4	11.5	57.5
L_2+M_{9030}	14	18.2	8.4	9.0	13.5	30.2
	15	22.3	8.6	8.9	13.3	32.2
	15.8	27.4	8.8	8.4	13.4	34.5
	16	33.6	8.6	7.7	13.1	35.8
	16.8	35.4	9.5	7.5	13.5	40.3
	17	36.8	10.1	7.5	14.3	44.5

References

1. Scales, C.D., Jr., et al., *Prevalence of kidney stones in the United States.* Eur Urol, 2012. **62**(1): p. 160-5.

2. Coe, F.L., A. Evan, and E. Worcester, *Kidney stone disease.* The Journal of clinical investigation, 2005. **115**(10): p. 2598-608.

3. Romero, V., H. Akpinar, and D.G. Assimos, *Kidney stones: a global picture of prevalence, incidence, and associated risk factors.* Reviews in urology, 2010. **12**(2-3): p. e86-96.

4. Lingeman, J.E., et al., *Shock wave lithotripsy: advances in technology and technique.* Nature reviews. Urology, 2009. **6**(12): p. 660-70.

5. Sakhaee, K., N.M. Maalouf, and B. Sinnott, *Clinical review. Kidney stones 2012: pathogenesis, diagnosis, and management.* J Clin Endocrinol Metab, 2012. **97**(6): p. 1847-60.

6. Chuong, C.J., P. Zhong, and G.M. Preminger, *Acoustic and mechanical properties of renal calculi: implications in shock wave lithotripsy.* Journal of endourology / Endourological Society, 1993. **7**(6): p. 437-44.

7. Parmar, M.S., *Kidney stones.* BMJ, 2004. **328**(7453): p. 1420-4.

8. Johrde, L.G. and F.H. Cocks, *Effect of pH on the microhardness of renal calculi.* Journal of biomedical materials research, 1986. **20**(7): p. 945-50.

9. Rao, P.N., G.M. Preminger, and J.P. Kavanagh, *Urinary tract stone disease*. 2011, Springer,: London. p. 1 online resource (xix, 720 p.) ill.

10. Chaussy, C., et al., *First clinical experience with extracorporeally induced destruction of kidney stones by shock waves.* The Journal of urology, 1982. **127**(3): p. 417-20.

11. Anagnostou, T. and D. Tolley, *Management of ureteric stones.* European urology, 2004. **45**(6): p. 714-21.

12. Skolarikos, A., G. Alivizatos, and J. de la Rosette, *Extracorporeal shock wave lithotripsy 25 years later: complications and their prevention.* European urology, 2006. **50**(5): p. 981-90; discussion 990.

13. Pearle, M.S., E.A. Calhoun, and G.C. Curhan, *Urologic diseases in America project: urolithiasis.* The Journal of urology, 2005. **173**(3): p. 848-57.

14. Skenazy, J., et al., *Nephrolithiasis: "scope," shock or scalpel?* J Endourol, 2005. **19**(1): p. 45-9.

15. Leighton, T.G. and R.O. Cleveland, *Lithotripsy.* Proceedings of the Institution of Mechanical Engineers. Part H, Journal of engineering in medicine, 2010. **224**(2): p. 317-42.

16. Rassweiler, J.J., et al., *Shock wave technology and application: an update.* European urology, 2011. **59**(5): p. 784-96.

17. Weizer, A.Z., P. Zhong, and G.M. Preminger, *New concepts in shock wave lithotripsy.* The Urologic clinics of North America, 2007. **34**(3): p. 375-82.

18. Zhou, Y., et al., *Innovations in shock wave lithotripsy technology: updates in experimental studies.* The Journal of urology, 2004. **172**(5 Pt 1): p. 1892-8.

19. McAteer, J.A., et al., *Strategies for improved shock wave lithotripsy.* Minerva Urol Nefrol, 2005. **57**(4): p. 271-87.

20. Cleveland, R.O. and J.A. McAteer, *The Physics of Shock Wave Lithotripsy*, in *Smith's Textbook on Endourology*, A.D. Smith, et al., Editors. 2009, BC Decker Inc: Hamilton, ON, Canada. p. 317-332.

21. Coleman, A.J. and J.E. Saunders, *A review of the physical properties and biological effects of the high amplitude acoustic field used in extracorporeal lithotripsy.* Ultrasonics, 1993. **31**(2): p. 75-89.

22. Lokhandwalla, M. and B. Sturtevant, *Fracture mechanics model of stone comminution in ESWL and implications for tissue damage.* Phys Med Biol, 2000. **45**(7): p. 1923-40.

23. Ortiz, M., *Microcrack coalescence and macroscopic crack growth initation in brittle solids.* International Journal of Solids and Structures, 1988. **24**(3): p. 18.

24. Crum, L.A., *Tensile-Strength of Water.* Nature, 1979. **278**(5700): p. 148-149.

25. Coleman, A.J., et al., *Acoustic cavitation generated by an extracorporeal shockwave lithotripter.* Ultrasound in medicine & biology, 1987. **13**(2): p. 69-76.

26. Zhong, P., *Shock wave lithotripsy*, in *Bubble dynamics and shock waves*, C. Delale, Editor. 2013, Springer Berlin Heidelberg. p. 291-338.

27. Gracewski, S.M., et al., *Internal stress wave measurements in solids subjected to lithotripter pulses.* J Acoust Soc Am, 1993. **94**(2 Pt 1): p. 652-61.

28. Eisenmenger, W., *The mechanisms of stone fragmentation in ESWL.* Ultrasound in medicine & biology, 2001. **27**(5): p. 683-93.

29. Xi, X. and P. Zhong, *Dynamic photoelastic study of the transient stress field in solids during shock wave lithotripsy.* J Acoust Soc Am, 2001. **109**(3): p. 1226-39.

30. Cleveland, R.O. and O.A. Sapozhnikov, *Modeling elastic wave propagation in kidney stones with application to shock wave lithotripsy.* J Acoust Soc Am, 2005. **118**(4): p. 2667-76.

31. Sapozhnikov, O.A., et al., *A mechanistic analysis of stone fracture in lithotripsy.* J Acoust Soc Am, 2007. **121**(2): p. 1190-202.

32. Church, C.C., *A theoretical study of cavitation generated by an extracorporeal shock wave lithotripter.* J Acoust Soc Am, 1989. **86**(1): p. 215-27.

33. Crum, L.A., *Cavitation Microjets as a Contributory Mechanism for Renal Calculi Disintegration in Eswl.* Journal of Urology, 1988. **140**(6): p. 1587-1590.

34. Sass, W., et al., *The mechanisms of stone disintegration by shock waves.* Ultrasound in medicine & biology, 1991. **17**(3): p. 239-43.

35. Sapozhnikov, O.A., et al., *Effect of overpressure and pulse repetition frequency on cavitation in shock wave lithotripsy.* Journal of the Acoustical Society of America, 2002. **112 %6**(3): p. 1183-1195.

36. Zhu, S.L., et al., *The role of stress waves and cavitation in stone comminution in shock wave lithotripsy.* Ultrasound in Medicine and Biology, 2002. **28**(5): p. 661-671.

37. Lautz, J., G. Sankin, and P. Zhong. *Synergistic interaction between stress waves and cavitation is important for successful comminution of residual stone fragments in shock wave* in *Acoustic Society of America*. 2011. San Diego, CA.

38. Smith, N. and P. Zhong, *Stone comminution correlates with the average peak pressure incident on a stone during shock wave lithotripsy.* Journal of biomechanics, 2012. **45**(15): p. 2520-5.

39. Griffith, A.A., *The phenomena of rupture and flow in solids.* Philosophical Transactions of the Royal Society of London. Series A-Mathematical Physical and Engineering Sciences 1921. **221**: p. 163-198.

40. Granz, B. and G. Kohler, *What makes a shock wave efficient in lithotripsy?* J Stone Dis, 1992. **4**(2): p. 123-8.

41. Moerland, M.A., et al., *The influence of respiration induced motion of the kidneys on the accuracy of radiotherapy treatment planning, a magnetic resonance*

imaging study. Radiotherapy and oncology : journal of the European Society for Therapeutic Radiology and Oncology, 1994. **30**(2): p. 150-4.

42. Schwartz, L.H., et al., *Kidney mobility during respiration.* Radiotherapy and oncology : journal of the European Society for Therapeutic Radiology and Oncology, 1994. **32**(1): p. 84-6.

43. Langen, K.M. and D.T. Jones, *Organ motion and its management.* International journal of radiation oncology, biology, physics, 2001. **50**(1): p. 265-78.

44. Chang, C.C., et al., *In vitro study of ultrasound based real-time tracking of renal stones for shock wave lithotripsy: part 1.* The Journal of urology, 2001. **166**(1): p. 28-32.

45. Chen, C.J., et al., *Clinical experience with ultrasound-based real-time tracking lithotripsy in the single renal stone treatment.* J Endourol, 2009. **23**(11): p. 1811-5.

46. Sorensen, M.D., et al., *Quantitative assessment of shockwave lithotripsy accuracy and the effect of respiratory motion.* Journal of endourology / Endourological Society, 2012. **26**(8): p. 1070-4.

47. Cheng, B.-S., et al., *The use of endotracheal general anesthesia with a one-minute pause in ventilation to increase the effectiveness of extracorporeal shock wave lithotripsy.* Journal of the Taiwan Urological Association, 2006. **16**(2): p. 4.

48. Smith, N.B. and P. Zhong, *A heuristic model of stone comminution in shock wave lithotripsy.* J Acoust Soc Am, 2013. **134**(2): p. 1548-58.

49. Cleveland, R.O., R. Anglade, and R.K. Babayan, *Effect of stone motion on in vitro comminution efficiency of Storz Modulith SLX.* Journal of endourology / Endourological Society, 2004. **18**(7): p. 629-33.

50. Leighton, T.G., et al., *A passive acoustic device for real-time monitoring of the efficacy of shockwave lithotripsy treatment.* Ultrasound Med Biol, 2008. **34**(10): p. 1651-65.

51. Eichel, L., P. Batzold, and E. Erturk, *Operator experience and adequate anesthesia improve treatment outcome with third-generation lithotripters.* J Endourol, 2001. **15**(7): p. 671-3.

52. Sorensen, C., et al., *Comparison of intravenous sedation versus general anesthesia on the efficacy of the Doli 50 lithotriptor.* J Urol, 2002. **168**(1): p. 35-7.

53. London, R.A., T. Kudlak, and R.A. Riehle, *Immersion anesthesia for extracorporeal shock wave lithotripsy. Review of two hundred twenty treatments.* Urology, 1986. **28**(2): p. 86-94.

54. Lee, C., et al., *Impact of type of anesthesia on efficacy of medstone STS lithotripter.* J Endourol, 2007. **21**(9): p. 957-60.

55. Graber, S.F., et al., *A prospective randomized trial comparing 2 lithotriptors for stone disintegration and induced renal trauma.* J Urol, 2003. **169**(1): p. 54-7.

56. Lingeman, J.E., et al., *Shockwave lithotripsy: anecdotes and insights.* J Endourol, 2003. **17**(9): p. 687-93.

57. Bergsdorf, T., S. Thuroff, and C. Chaussy, *The isolated perfused kidney: an in vitro test system for evaluation of renal tissue damage induced by high-energy shockwaves sources.* J Endourol, 2005. **19**(7): p. 883-8.

58. Willis, L.R., et al., *Prevention of lithotripsy-induced renal injury by pretreating kidneys with low-energy shock waves.* J Am Soc Nephrol, 2006. **17**(3): p. 663-73.

59. Evan, A.P., et al., *Independent assessment of a wide-focus, low-pressure electromagnetic lithotripter: absence of renal bioeffects in the pig.* BJU Int, 2008. **101**(3): p. 382-8.

60. Chang, C.C., et al., *In vitro study of ultrasound based real-time tracking of renal stones for shock wave lithotripsy: part 1.* J Urol, 2001. **166**(1): p. 28-32.

61. Bohris, C., T. Bayer, and C. Lechner, *Hit/Miss monitoring of ESWL by spectral Doppler ultrasound.* Ultrasound Med Biol, 2003. **29**(5): p. 705-12.

62. Orkisz, M., et al., *Image based renal stone tracking to improve efficacy in extracorporeal lithotripsy.* J Urol, 1998. **160**(4): p. 1237-40.

63. Chang, C.C., et al., *In vitro study of the revised ultrasound based real-time tracking of renal stones for shock wave lithotripsy: Part 1.* J Urol, 2013. **189**(6): p. 2357-63.

64. Qin, J., et al., *Effect of lithotripter focal width on stone comminution in shock wave lithotripsy.* J Acoust Soc Am, 2010. **127**(4): p. 2635-45.

65. Neisius, A., et al., *Improving the lens design and performance of a contemporary electromagnetic shock wave lithotripter.* Proc Natl Acad Sci U S A, 2014.

66. Lingeman, J.E., et al., *Shock wave lithotripsy: advances in technology and technique.* Nat Rev Urol, 2009. **6**(12): p. 660-70.

67. Qin, J., *Performance Evaluation and Design Improvement of Electromagnetic Shock Wave Lithotripters*, in *Department of Mechanical Engineering and Materials Science*. 2008, Duke University. p. 162.

68. Zhou, Y. and P. Zhong, *The effect of reflector geometry on the acoustic field and bubble dynamics produced by an electrohydraulic shock wave lithotripter.* J Acoust Soc Am, 2006. **119**(6): p. 3625-36.

69. Martini, F., J. Nath, and E. Bartholomew, *The urinary system*, in *Fundamentals of Anatomy and Physiology*. 2007, Benjamin-Cummings Publishing Company.

70. Eisner, B.H., et al., *Differences in stone size and ureteral dilation between obstructing proximal and distal ureteral calculi.* Urology, 2008. **72**(3): p. 517-20.

71. Singal, R.K. and J.D. Denstedt, *Contemporary management of ureteral stones.* The Urologic clinics of North America, 1997. **24**(1): p. 59-70.

72. Dugdale, D., *Nephrolithiasis*, in *American Accreditation HealthCare Commission*, D. Zieve, Editor. 2011: Atlanta, Georgia. p. 1.

73. Fovargue, D.E., et al., *Experimentally validated multiphysics computational model of focusing and shock wave formation in an electromagnetic lithotripter.* J Acoust Soc Am, 2013. **134**(2): p. 1598-609.

74. Pierce, A.D., *Acoustics : an introduction to its physical principles and applications*. McGraw-Hill series in mechanical engineering. 1981, New York: McGraw-Hill Book Co. xxiii, 642 p.

75. Dimarzio, C.A., *Optics for engineers*. 2012, Boca Raton: CRC Press. xxiii, 535 p.

76. Mast, T.D., *Fresnel approximations for acoustic fields of rectangularly symmetric sources.* J Acoust Soc Am, 2007. **121**(6): p. 3311-22.

77. Fresnel, A., Ann. Chem. Phys., 1816. **1**(239).

78. Delius, M., F. Ueberle, and S. Gambihler, *Destruction of gallstones and model stones by extracorporeal shock waves.* Ultrasound Med Biol, 1994. **20**(3): p. 251-8.

79. Zhong, P., Y. Zhou, and S. Zhu, *Dynamics of bubble oscillation in constrained media and mechanisms of vessel rupture in SWL.* Ultrasound in medicine & biology, 2001. **27**(1): p. 119-34.

80. Matlaga, B.R., et al., *Potential for cavitation-mediated tissue damage in shockwave lithotripsy.* Journal of endourology / Endourological Society, 2008. **22**(1): p. 121-6.

81. Chen, H., et al., *Blood vessel deformations on microsecond time scales by ultrasonic cavitation.* Physical review letters, 2011. **106**(3): p. 034301.

82. Zhu, S., et al., *The role of stress waves and cavitation in stone comminution in shock wave lithotripsy.* Ultrasound in medicine & biology, 2002. **28**(5): p. 661-71.

83. Pishchalnikov, Y.A., et al., *Cavitation bubble cluster activity in the breakage of kidney stones by lithotripter shockwaves.* Journal of Endourology, 2003. **17**(7): p. 435-446.

84. Coleman, A.J., et al., *Pressure waveforms generated by a Dornier extracorporeal shock-wave lithotripter.* Ultrasound Med Biol, 1987. **13**(10): p. 651-7.

85. Huber, P., et al., *In vivo detection of ultrasonically induced cavitation by a fibre-optic technique.* Ultrasound in medicine & biology, 1994. **20**(8): p. 811-25.

86. Coleman, A.J., M.J. Choi, and J.E. Saunders, *Detection of acoustic emission from cavitation in tissue during clinical extracorporeal lithotripsy.* Ultrasound in medicine & biology, 1996. **22**(8): p. 1079-87.

87. Zhong, P., et al., *Inertial cavitation and associated acoustic emission produced during electrohydraulic shock wave lithotripsy.* J Acoust Soc Am, 1997. **101**(5 Pt 1): p. 2940-50.

88. Bailey, M.R., et al., *Cavitation detection during shock-wave lithotripsy.* Ultrasound in medicine & biology, 2005. **31**(9): p. 1245-56.

89. Smith, N., et al., *A comparison of light spot hydrophone and fiber optic probe hydrophone for lithotripter field characterization.* Review of Scientific Instruments, 2012. **83 %6**(1): p. %&.

90. Sankin, G.N., D. Piech, and P. Zhong, *Stereoscopic high-speed imaging using additive colors.* Review of Scientific Instruments, 2012. **83 %6**(4): p. %&.

91. Frank, S., et al., *Diffusion-controlled growth or dissolution of cavitation nuclei in shock wave lithotripsy.* Physical Review Applied, 2014 (Submitted).

92. Lautz, J., G. Sankin, and P. Zhong, *Turbulent water coupling in shock wave lithotripsy.* Physics in Medicine and Biology, 2013. **58** (3): p. 735-748

93. Davies, S.C., et al., *Ultrasound quantitation of respiratory organ motion in the upper abdomen.* The British journal of radiology, 1994. **67**(803): p. 1096-102.

94. Brandner, E.D., et al., *Abdominal organ motion measured using 4D CT.* Int J Radiat Oncol Biol Phys, 2006. **65**(2): p. 554-60.

95. Perel, A., et al., *High frequency positive pressure ventilation during general anesthesia for extracorporeal shock wave lithotripsy.* Anesth Analg, 1986. **65**(11): p. 1231-4.

96. Esch, E., et al., *A simple method for fabricating artificial kidney stones of different physical properties.* Urol Res, 2010. **38**(4): p. 315-9.

97. Sorensen, M.D., et al., *Quantitative assessment of shockwave lithotripsy accuracy and the effect of respiratory motion.* J Endourol, 2012. **26**(8): p. 1070-4.

98. Eisenmenger, W., *The mechanisms of stone fragmentation in ESWL.* Ultrasound Med Biol, 2001. **27**(5): p. 683-93.

99. Smith, N. and P. Zhong, *Stone comminution correlates with the average peak pressure incident on a stone during shock wave lithotripsy.* J Biomech, 2012. **45**(15): p. 2520-5.

100. Papadoukakis, S., J.-U. Stolzenburg, and M.C. Truss, *Treatment Strategies of Ureteral Stones.* EAU-EBU Update Series, 2006. **4**(5): p. 184-190.

101. Ibrahim, A.I., et al., *Prognostic factors in the conservative treatment of ureteric stones.* Br J Urol, 1991. **67**(4): p. 358-61.

102. Segura, J.W., et al., *Ureteral Stones Clinical Guidelines Panel summary report on the management of ureteral calculi. The American Urological Association.* J Urol, 1997. **158**(5): p. 1915-21.

103. Coll, D.M., M.J. Varanelli, and R.C. Smith, *Relationship of spontaneous passage of ureteral calculi to stone size and location as revealed by unenhanced helical CT.* AJR Am J Roentgenol, 2002. **178**(1): p. 101-3.

104. Miller, O.F. and C.J. Kane, *Time to stone passage for observed ureteral calculi: a guide for patient education.* J Urol, 1999. **162**(3 Pt 1): p. 688-90; discussion 690-1.

105. Tiselius, H.G., et al., *Guidelines on urolithiasis.* Eur Urol, 2001. **40**(4): p. 362-71.

106. Preminger, G.M., et al., *2007 guideline for the management of ureteral calculi.* J Urol, 2007. **178**(6): p. 2418-34.

107. Peschel, R., G. Janetschek, and G. Bartsch, *Extracorporeal shock wave lithotripsy versus ureteroscopy for distal ureteral calculi: a prospective randomized study.* J Urol, 1999. **162**(6): p. 1909-12.

108. Turk, T.M. and A.D. Jenkins, *A comparison of ureteroscopy to in situ extracorporeal shock wave lithotripsy for the treatment of distal ureteral calculi.* J Urol, 1999. **161**(1): p. 45-6; discussion 46-7.

109. Argyropoulos, A.N. and D.A. Tolley, *SWL is more cost-effective than ureteroscopy and Holmium:YAG laser lithotripsy for ureteric stones: A comparative analysis for a tertiary referral centre.* British Journal of Medical and Surgical Urology, 2010. **3**(2): p. 65-71.

110. Phipps, S., et al., *The management of ureteric stones.* Ann R Coll Surg Engl, 2010. **92**(5): p. 368-72.

111. Elbahnasy, A.M., et al., *Lower caliceal stone clearance after shock wave lithotripsy or ureteroscopy: the impact of lower pole radiographic anatomy.* J Urol, 1998. **159**(3): p. 676-82.

112. Gupta, N.P., et al., *Infundibulopelvic anatomy and clearance of inferior caliceal calculi with shock wave lithotripsy.* J Urol, 2000. **163**(1): p. 24-7.

113. Sampaio, F.J., A.L. D'Anunciacao, and E.C. Silva, *Comparative follow-up of patients with acute and obtuse infundibulum-pelvic angle submitted to extracorporeal shockwave lithotripsy for lower caliceal stones: preliminary report and proposed study design.* J Endourol, 1997. **11**(3): p. 157-61.

114. Bagley, D.H. and M.H. Rittenberg, *Intrarenal dimensions. Guidelines for flexible ureteropyeloscopes.* Surg Endosc, 1987. **1**(2): p. 119-21.

115. Vienna, T.G.H., *Radiograph of the kidneys*. 2005.

116. Smith, A.D., *Smith's textbook of endourology*. 2nd ed. 2007, Hamilton Ont. London: BC Decker. xiv, 972, 31 p.

117. Cury, F., et al., *Respiratory-induced organ motion during free breathing: A source of errors during radiosurgery for the upper urinary tract*, in *Proceedings of the 53rd Annual ASTRO Meeting*. 2011: Miami, Florida.

118. Anglada-Curado, F.J., et al., *Extracorporeal shock wave lithotripsy for distal ureteral calculi: improved efficacy using low frequency.* Int J Urol, 2013. **20**(2): p. 214-9.

Biography

Jaclyn was born in Winchester, Massachusetts in 1987. Soon after, her family moved to Jay, Maine where she spent her entire childhood. After graduating from Jay High School, she attended Boston University, where she received a Bachelor of Science degree in Biomedical Engineering in 2009. Inspired by her coursework and renowned biomedical engineering faculty, she developed an interest in research and development specifically in medical device design and innovation. Under the mentorship of Dr. Joyce Wong, she decided to pursue graduate research at the intersection of fundamental mechanical engineering design and clinical medical devices. Jaclyn pursued graduate study in Duke University's Mechanical Engineering and Materials Science department for its diverse, interdisciplinary and innovative research areas. There, Jaclyn sought a research lab that specialized in medical device innovation. She met Dr. Pei Zhong and immediately joined his laboratory, focusing on therapeutic ultrasound and in particular shock wave lithotripsy. Jaclyn benefited from the intelligent and passionate lab mentors and colleagues in a highly collaborative research environment. Below are her publications, conference presentations and awards since obtaining her bachelor's degree:

Refereed Journal Publications

"Diffusion-controlled growth or dissolution of cavitation nuclei in shock wave lithotripsy," *Physical Review Applied,* Spencer Frank, Jaclyn Lautz, Georgy Sankin, Andrew Szeri, and Pei Zhong (in review)

"Turbulent water coupling in shock wave lithotripsy," *Physics in Medicine and Biology,* Jaclyn Lautz, Georgy Sankin, and Pei Zhong (January 2013)

"Displacement of particles in microfluidics by laser-generated tandem bubble," *Applied Physics Letters,* Jaclyn Lautz, Georgy Sankin, Fang Yuan, and Pei Zhong (November 2010)

Conference Presentations

"A non-axisymmetric, elongated pressure distribution in the lithotripter focal plane enhances stone comminution in vitro during simulated respiratory motion" *Acoustical Society of America,* San Francisco, California 2013

"Mechanistic assessment of the role of stress waves and cavitation in stone comminution during shock wave lithotripsy" *International Society of Therapeutic Ultrasound,* Heidelberg, Germany 2012

"Effects of turbulent water coupling on cavitation activity in shock wave lithotripsy" *NSF Future Engineering Innovation Symposium*, Arlington, VA 2012

"Synergistic interaction between stress waves and cavitation is important for successful stone comminution of residual stone fragments in shock wave lithotripsy" *Acoustical Society of America Conference,* San Diego, CA 2011

"Displacement of cells in microfluidics: Application to cell sorting," *Annual Biomedical Engineering Conference,* Austin, TX 2010

"Synergistic interaction between stress waves and cavitation in Shock Wave Lithotripsy," *Annual Biomedical Engineering Conference,* Austin, TX 2010

Awards

National Science Foundation Graduate Research Fellowship	2011 – 2014
Acoustical Society of America Student Travel Award	2013
National Science Foundation Engineering Innovation Fellowship	2012
International Society of Therapeutic Ultrasound Student Travel Award	2012
Most Innovative Project, MEMS Retreat, Duke University	2012
Best Presentation Award, MEMS Retreat, Duke University,	2010